uOttawa

L'Université canadienne
Canada's university

FACULTÉ DES ÉTUDES SUPÉRIEURES ET POSTOCTORALES

uOttawa

L'Université canadienne
Canada's university

FACULTY OF GRADUATE AND POSDOCTORAL STUDIES

Choonghee Jo

AUTEUR DE LA THÈSE / AUTHOR OF THESIS

Ph.D. (Mechanical Engineering)

GRADE / DEGREE

Department of Mechanical Engineering

FACULTÉ, ÉCOLE, DÉPARTEMENT / FACULTY, SCHOOL, DEPARTMENT

Constitutive Modeling for Mechanical Behavior of Polymer-Clay Nanocomposite Foams

TITRE DE LA THÈSE / TITLE OF THESIS

Hani Naguib

DIRECTEUR (DIRECTRICE) DE LA THÈSE / THESIS SUPERVISOR

CO-DIRECTEUR (CO-DIRECTRICE) DE LA THÈSE / THESIS CO-SUPERVISOR

EXAMINATEURS (EXAMINATRICES) DE LA THÈSE / THESIS EXAMINERS

Glen Hibbard

David Redekop

Michel Nganbe

François Robitaille

Gary W. Slater

Le Doyen de la Faculté des études supérieures et postdoctorales / Dean of the Faculty of Graduate and Postdoctoral Studies

CONSTITUTIVE MODELING FOR MECHANICAL BEHAVIOR OF POLYMER-CLAY NANOCOMPOSITE FOAMS

by

Choonghee Jo

A thesis submitted to the Faculty of Graduate and Postdoctoral Studies
in partial fulfillment of the requirements for the degree of

DOCTOR OF PHILOSOPHY

in Mechanical Engineering

Ottawa-Carleton Institute for Mechanical and Aerospace Engineering
University of Ottawa
Ottawa, Canada

April 2008

Your file Votre référence
ISBN: 978-0-494-50737-7
Our file Notre référence
ISBN: 978-0-494-50737-7

Abstract

Constitutive equations for characterizing the nonlinear mechanical behavior of polymer/clay nanocomposite foams were studied. To consider the influence of the crystallinity on the mechanical properties of the foams, both amorphous and semi-crystalline polymers were used. Several viscoelastic models were accounted for the modeling of tensile behavior. The constitutive equation for nonlinear tensile behavior of microcellular Poly(methyl-methacrylate) (PMMA) foams was expressed in terms of material properties and physical characteristics of foams such as strain, strain rate, elastic modulus, relative density of foam, and relaxation time constant. In the constitutive model for tensile behavior of PMMA/clay nanocomposite foams, the reinforcing effect by intercalation of the clays and the detrimental effect by clay agglomeration were considered. The constitutive equation was expressed in terms of clay morphology and material properties. The aspect ratio of clays and the expansion of clay layer spacing in the intercalated clay clusters were proved to play a vital role in the reinforcing mechanism. For the modeling of semi-crystalline polymer/clay nanocomposite foams, the effects of nanoclay loadings, crystallinity, strain rate, and foaming conditions on the foam morphology and mechanical properties of microcellular high density polyethylene (HDPE)/clay nanocomposites were studied. Intercalated clay structures were investigated in the nanocomposites, and microcellular foams were manufactured by a batch foaming process. Tensile mechanical tests indicated that Young's modulus and the tensile strength were reinforced on the whole with crystallinity and nanoclay contents. Also, a constitutive model for tensile behavior of HDPE/clay nanocomposite foams was proposed. The elastic modulus of the foams was developed using micromechanics theory and representative volume element (RVE) concept. The constitutive model for HDPE/clay nanocomposite foams was expressed in terms of microstructural properties of polymer, and physical properties of the foams. Employing the proper constitutive laws, the macroscopic material behaviors of polymer/clay nanocomposite foams could be represented. The developed constitutive models were demonstrated by experiment.

Acknowledgements

I would like to express my gratitude to my supervisor, Dr. Hani E. Naguib, whose support, guidance, and encouragements helped me to complete this work. Also, I am grateful to Jin Fu, Steven Wong, and Yoon Hwan Lee for the help of experiments. Finally I would like to thank my family.

Table of Contents

List of Figures

List of Tables

List of Symbols

A_c	Area of the clay particle
a_1	Dimension of clay particle or intercalated clay stacks
a_3	Thickness of clay particle or intercalated clay stacks
a_α	Radius of crack α
C_1	Effect of the coupling agent on the crystallinity
C_2	Effect of coupling agent on the Young's modulus
c	Half crack length
D	Elastic compliance tensor
D_c	Cell diameter (μm)
$\bar{D}$	Overall compliance
d	Diameter of sphere cavity
d_1	Dimension of cube
d_c	Clay layer thickness
d_m	Clay layer spacing
E	Elastic modulus
E_c	Elastic modulus of composites
E_m	Elastic modulus of polymer matrix
E_m'	Elastic modulus of HDPE containing PE-g-MAn
E_p	Elastic modulus of clay particulates
E_R	Elastic modulus by the Reuss model
E_s	Young's modulus of the unfoamed solid
E_{eq}	Equivalent elastic modulus
E^*	Elastic modulus of foams
$\bar{E}$	Overall elastic modulus

$\bar{E}_c$	Overall elastic modulus of nanocomposites
$\bar{E}^*$	Overall elastic modulus of foams
$\bar{E}_c^*$	Overall elastic modulus of nanocomposite foams
f	Volume fraction of the cavities in RVE
f_i	Intercalated fractions of clays
f_a	Agglomerated fractions of clays
K_I	Mode I fracture toughness
N	Total number of cracks per unit volume
N_i	Number of intercalated clay clusters in the matrix
N_α	Number of cracks of radius a_α per unit volume of RVE
n_c	Number of clay layers in each intercalated clay stack
p_0	Applied stress
R	Radius of cavity
r	Radial distance from the center of cavity
S	Eshelby's tensor
t	Time
u	Crack opening displacement in mode I crack
u^o	Boundary displacements
u_p	Displacement of clay stack in load direction
u_R	Radial displacement at the surface of the spherical cavity
V	Total volume of composites
V_c	Volume fraction of crystals
V_R	Volume expansion ratio of foams
v	Outer unit normal vector of bounded surface ∂V
v_m	Volume fraction of polymer matrix
v_m'	Volume fraction of the matrix after intercalation process
v_p	Volume fraction of clay particles

v_{pa}	Volume fraction of agglomerated clay particles
v_{pi}	Volume fraction of the clay particles which will be intercalated
v_{pi}'	Volume fraction of the intercalated regions
w_p	Weight fraction of clay particles
$Z(z)$	Complex function
α, β	Material constants
δ, ψ	Parameters in polar co-ordinates
ε	Total strain
$\dot{\varepsilon}$	Strain rate
ε_d	Strain at dashpot component
ε_s	Strain at spring component
$\overline{\varepsilon}$	Volume average of strain (effective strain)
$\overline{\varepsilon}^o$	Average strain of RVE without cavities
$\overline{\varepsilon}^c$	Additional strain due to the presence of cavities
$\overline{\varepsilon}^p$	Overall strain decreased by all intercalated clay stacks
$\overline{\varepsilon}^R$	Overall volumetric strain by a cavity
$\overline{\varepsilon}^\alpha$	Overall strain due to a crack a_α
ϕ	Fraction of solid in the cell struts
η	Viscosity modulus (Pa·s)
λ	Ramé constant
μ	Shear modulus
θ	Angle between the clay plane and the plane perpendicular to the load
ρ_c	Density of crystal structure
ρ_a	Density of amorphous structure
ρ_m	Specific gravity of polymer matrix
ρ_p	Specific gravity of clay particles
ρ_r	Relative density of foams (g/cm^3)

σ	Stress or overall tensile stress
σ_{TS}	Tensile strengths of unfoamed solid
σ_{TS}^{*}	Tensile strengths of foam
σ^{o}	Average macro stress
σ_{θ}	Tangential component of the stress at cavity
σ_{ij}	Crack tip stress component of mode I crack
τ	Relaxation time constant
ν	Poisson's ratio
χ_c	Crystallinity

Abbreviations

ASTM	American Society for Testing and Materials
C20A	Cloisite 20A
CO_2	Carbon dioxide
CRR	Cooperatively rearranging regions
DSC	Differential Scanning Calorimeter
HDPE	High density polyethylene
LDPE	Low density polyethylene
Org-MMT	Organic-Montmorillonite
PC	Polycarbonate
PE-*g*-MAn	Maleic Anhydride grafted Polyethylene
PMMA	Poly(methyl-methacrylate)
RVE	Representative Volume Element
SEM	Scanning Electron Microscope
TEM	Transmission Electron Microscope

Chapter 1

Introduction

1.1 Preamble

A great deal of interest has been focused on polymer/clay nanocomposite foams because of their superior physical, mechanical, thermal, and electrical properties compared to the unfoamed polymer or conventional foams. In the polymer/clay nanocomposite, the nanometer scaled silicate pellets produce a good reinforcement on the mechanical properties of the polymer whilst acting as a nucleation agent in the foaming process. Due to these unique properties, microcellular nanocomposite plastics can be used in a large number of innovative industrial and biomedical applications.

For actual product design using polymer/clay nanocomposite foams, numerical methods are indispensable, where the constitutive equations are used in the numerical methods as governing equations. The constitutive equations should be able to represent the mechanical characteristics of the materials used. Accordingly, there is an emerging need for the study of the constitutive models as well as the characterizing study of the foams. Many studies have focused on the processing and physical characterization of polymer/clay nanocomposite foams, and some studies of the mechanical properties of the foams have been performed. However, only few studies were performed on the modeling of the mechanical properties of the foams and particularly, little work has been reported for the constitutive equation of the foams.

On this account, constitutive models for characterizing the mechanical behavior of polymer/clay nanocomposite foams were developed in this study and the theoretical models were evaluated by experiments. The constitutive equations were expressed in terms of clay morphology, foam morphology, and material properties. Also, the influence of crystallinity and strain rate were incorporated in the models. The developed constitutive models could effectively predict the tensile behavior of amorphous polymer (PMMA)/clay nanocomposite foams and semi-crystalline polymer (HDPE)/clay nanocomposite foams.

1.2 Microcellular Foams

Foam materials have found more and more applications in industry because of their energy absorbing and recovery behavior during impact as well as lightweight and moldable characteristics. Microcellular plastics are polymeric foams with cell diameter sizes from 0.1 to 10 μm and cell densities in the range of 10^9 to 10^{15} cells/cm^3, and specific density reductions relative to the unfoamed plastic foams in the range of 5 to 98% [Kumar et al. 1994]. Compared to the unfoamed polymer, microcellular plastics generally possess superior physical, thermal, and electrical properties, i.e., higher strength-to-weight ratio [Klempner and Frisch 2004], higher impact strength [Matuana et al. 1998, Collias et al. 1994], increased toughness [Baldwin and Suh 1992], prolonged fatigue life [Seeler and Kumar 1993] and an increased thermal stability, increased thermal and electrical insulation properties [Taylor and Fernandez 2005, Xiang et al. 2006]. Therefore, microcellular foams have a great potential for applications such as packaging, insulation, automotive and aircraft industries, and structural components. Due to these unique properties, microcellular plastics can be used in a large number of innovative industrial applications. These include lightweight and high-strength parts for automotive and aerospace industries [Lee LJ et al. 2005]. Applications are also available for furniture, sporting goods, and packaging as well as thermal and electrical insulators. In addition, microcellular plastics are produced using environmentally safe gases such as nitrogen and carbon dioxide.

1.3 Polymer/Clay Nanocomposites

Organically modified layered silicates have been widely used as property enhancers for polymeric materials (Min et al. 2006, Alexandre et al. 2002, Tzavalas et al. 2006, Zhong and Kee 2005, Osman et al. 2005). Polymer nanocomposites are composed of an organic polymer matrix and inorganic nanoparticles. Nanofillers have at least one dimension on the order of 1 nm and the platelet-shaped nanofillers have high aspect ratios from 10 to 1000 [Giannelis 1996]. Since the dispersed phase dimensions of clays are in the nanometer range, nanoparticles can impact the macroscopic properties of the polymer with only a few weight percent of loadings in the polymer. These nanometer scaled pellets with such high aspect

ratios and their nanometer scale dispersibility tend to produce a good reinforcement and improve the mechanical properties of the polymer over those of the pure polymer or conventional composites [Giannelis et al. 1999, LeBaron et al. 1999, Vaia et al. 1999, Biswas and Ray 1999, McNally et al. 2003, Tseng et al. 2002, Wan et al. 2003, Wang H et al. 2001, Giannelis 1996, Alexandre and Dubois 2000]. At low clay content, polymer layered silicate nanocomposites exhibited enhanced mechanical, thermal and barrier properties [Pinnavaia and Beall 1989, Liao et al. 2001]. Also, various improved properties such as higher heat distortion temperatures, enhanced flame resistance, increased modulus, lower permeability, improved thermal resistivity, and altered electronic and optical properties have been discovered [Bharadwaj 2001, Kumar et al. 2003, Du et al. 2002, Giannelis 1996, Wang and Pinnavaia 1998, Kojima et al. 1993].

The effects of the filler on the composite materials depend on its size, aspect ratio, hybrid morphology, and dispersion quality [Ray et al. 2005, Fertig III et al. 2004, Unal et al, 2004, Wang et al, 2005]. The difference of the nanocomposite structure is usually dependent upon the method of fabrication and the degree of compatibility between the polymer matrix and the clays [Lopez-Manchado et al. 2004, Wang et al. 2004]. Intercalated polymer/clay nanocomposites are formed when the polymer is inserted between the clay layers. If clays are dispersed in a polymer matrix and the orientated distribution of the clay layers are destroyed, exfoliated nanocomposites are formed. To achieve the property enhancement in the nanocomposites, the clay layers should disperse as single platelets throughout the polymer matrix (delamination), where the structure is microscopically isotropic. To attain such dispersion of clay platelets, the polymer should first penetrate between the clay platelets, in which an intercalated morphology is formed and the silicate registry is retained. This intercalation is possible if both the polymer and the clay layers have polar groups that have favorable interaction. The compatibility of the clay modifier with the polymer matrix plays an important role in exfoliation. When Cloisite 15A was used as clay the intercalated structures could be seen in polyethylene matrix. On the other hand, when Cloisite 30B was used, only large and small tactoids with no evidence of intercalation were shown [Mehrabzadeh and Kamal 2004]. It is because Cloisite 30B is not compatible with polyethylene. One of the factors influence on the intercalation or exfoliation can be the extruder configuration when the nanocomposites are produced by melt intercalation

[Mehrabzadeh and Kamal 2004]. Using higher shear mixing and residence time (low feed rates) in the extruder, better mixed polymer/clay samples can be obtained and therefore, more intercalated or exfoliated structures are expected. The effect of compatibilizer (Maleic anhydride grafted high-density polyethylene) on intercalation and exfoliation was not significant [Mehrabzadeh and Kamal 2004].

Polymer nanocomposites can be synthesized by three primary production strategies. The first is the melt intercalation of a polymer into an organically modified silicate [Zhong and Kee 2005, Lee et al. JH 2005, Zhang and Wilkie 2003, Wang et al. 2001, Liang et al. 2004, Wang et al. 2003]. This method works well with polar polymers. Since polyethylene (PE) is a nonpolar polymer, homogeneous dispersion of the clay mineral in polyethylene is difficult. Thus ammonium-modified silicates are used with high density polyethylene (HDPE) [Jeon et al. 1998]. Wang et al. [Wang et al. 2002] reported that clays could be exfoliated in maleated PE/clay nanocomposites produced by melt intercalation. The second method is in situ polymerization in an aqueous polymer solution [Bergman et al. 1999, Wei et al. 2004]. Exfoliation could be achieved only by in situ polymerization of HDPE, in the presence of clay [Bergman et al. 1999, Alexandre et al. 2002]. However, it is limited to polymers that are soluble. As a third method, a silicate that is intercalated by an initiator or catalyst is used with monomer to form an intercalated or exfoliated polymer nanocomposite [Weimer et al. 1999]. Jeon et al. [Jeon et al. 1998] obtained intercalated HDPE nanocomposites using solution blending method with HDPE and modified sodium montmorillonite silicates. Also, It is realized that polyethylene nanocomposite with good exfoliation or intercalation can be obtained by proper modification of HDPE [Xu et al. 2005].

Generally, the strength and modulus of polymer/clay composites increase with increasing clay loading, and nanocomposites containing more intercalated or exfoliated structures show higher tensile modulus [Osman et al. 2005, Lee JH et al. 2005]. Also, the mechanical properties of polymer/clay nanocomposites depend on many factors, including the aspect ratio of the filler, the degree of dispersion of the filler in the matrix resin and the adhesion at the filler-matrix interface. Generally, clay does not influence the crystal form, melting temperature or crystallinity of HDPE. However, it acts as a nucleation agent, increases marginally the crystallization temperatures, and reduces the crystallite size [Lee JH et al. 2005]. Compression molding and higher residence time raise the modulus, while causing

reduction in the elongation at break. This can be due to enhanced intercalation or exfoliation [Zhong and Kee 2005]. Organoclay has barrier effect improving the thermal stability, and the other is the catalysis effect which degrades the polymer matrix, and consequently decreases the thermal stability. When small fractions of clay are added, the clay layers are well dispersed and the barrier effect is predominant. However, with increasing clay loading, the catalyzing effect rises and becomes dominant, so the thermal stability of the nanocomposites decreases [Zhao et al. 2005, Qin et al. 2004]. The clay itself can also catalyze the degradation of polymer matrixes, which reduces the thermal stability of polymer/clay nanocomposites [Qin et al. 2004]. By adding clays, the flammability resistance of polyethylene was greatly improved due to the formation of the clay-enriched protective char during the combustion [Wang et al. 2003, Zhao et al. 2005]. This is caused by a physical barrier action of char to mass and heat transfer [Gilman et al. 2000].

1.4 Nanocomposite Foams

Recently, a great deal of interest has been focused on the polymer/clay nanocomposite foams because well-dispersed nanometer scaled fillers in the polymer matrix can be used as nucleation sites in the foaming process. The interfaces between the fillers and the polymer can be potential nucleation sites where heterogeneous nucleation can be induced. Also, since the size of the filler is on the order of nanometers, the nanoparticles can be used in microcellular polymeric foam processing as a nucleation agent [Manninen et al. 2005]. As a result, the nano-scaled particles can contribute to the enhancement of the mechanical properties of the foams by micro-scaled reinforcement. As such, microcellular foams are produced easily with a small amount of nanoparticles, and many synthesis and processing techniques for nanocomposite foams have been studied.

The microcellular plastics can be produced by extrusion method, batch processing, and semi-continuous processing. In this study, batch process method is used for foam samples. The batch processing method is explained with three mechanisms: creating a gas/polymer solution, inducing a thermodynamic instability to nucleate billions of micro voids, and controlling the growth of stable nuclei by diffusion. On the first step of the process, plastic samples are placed into a pressure vessel of CO_2. After several days, the samples are

removed from the pressure vessel and heated to near their glass transition temperature. After some time, the plastic becomes soft enough so that the gas trapped inside the plastic can push the plastic outward, then plastic foams are made. Microcellular Plastics can be made of nearly all polymers and fiber reinforced polymers including thermosetting, amorphous, semi-crystalline, elastomeric, and liquid crystalling polymers. In this study, amorphous polymer and semi-crystalline polymer are used.

1.5 Motivation and Objectives

As the use of polymer/clay nanocomposite foams is increasing the characterization study for the nanocomposites and their foams have been conducted. In accompany with this, a need for constitutive models representing the foams is increasing because the constitutive equations form a basis of computational design. Therefore, the need for predicting and simulating the mechanical behavior of polymer/clay nanocomposite foams is motivated by the increasing use of new foam materials in many applications. When new foam materials are used for manufacturing, the role of constitutive equations on the process up to final product is in Fig. 1.1. For practical design and analysis on using microcellular nanocomposite plastics, numerical tools which can predict and estimate the characterization of the mechanical properties of the foam materials are necessary, which is in need of the corresponding constitutive equations. This demand causes the development of models of the underlying mechanics that are responsible for the observed properties. Accordingly, the desire to have a constitutive model for microcellular nanocomposite materials is increasing. On this account, constitutive models for characterizing the mechanical properties of polymer/clay nanocomposite foams are developed in this study. The models are especially designed for the nanocomposite foams produced by using both amorphous polymer and semi-crystalline polymer. Also, the models are verified by experiments, where PMMA and HDPE are used for amorphous and semi-crystalline polymers, respectively. PMMA is highly transparent and its products show strong, light, and tough characteristics. HDPE foams are widely used in ridge packaging, recreational equipment, and as structural foams because of higher stiffness compared to LDPE foams. Also, their microcellular foams have been of great interest in recent years.

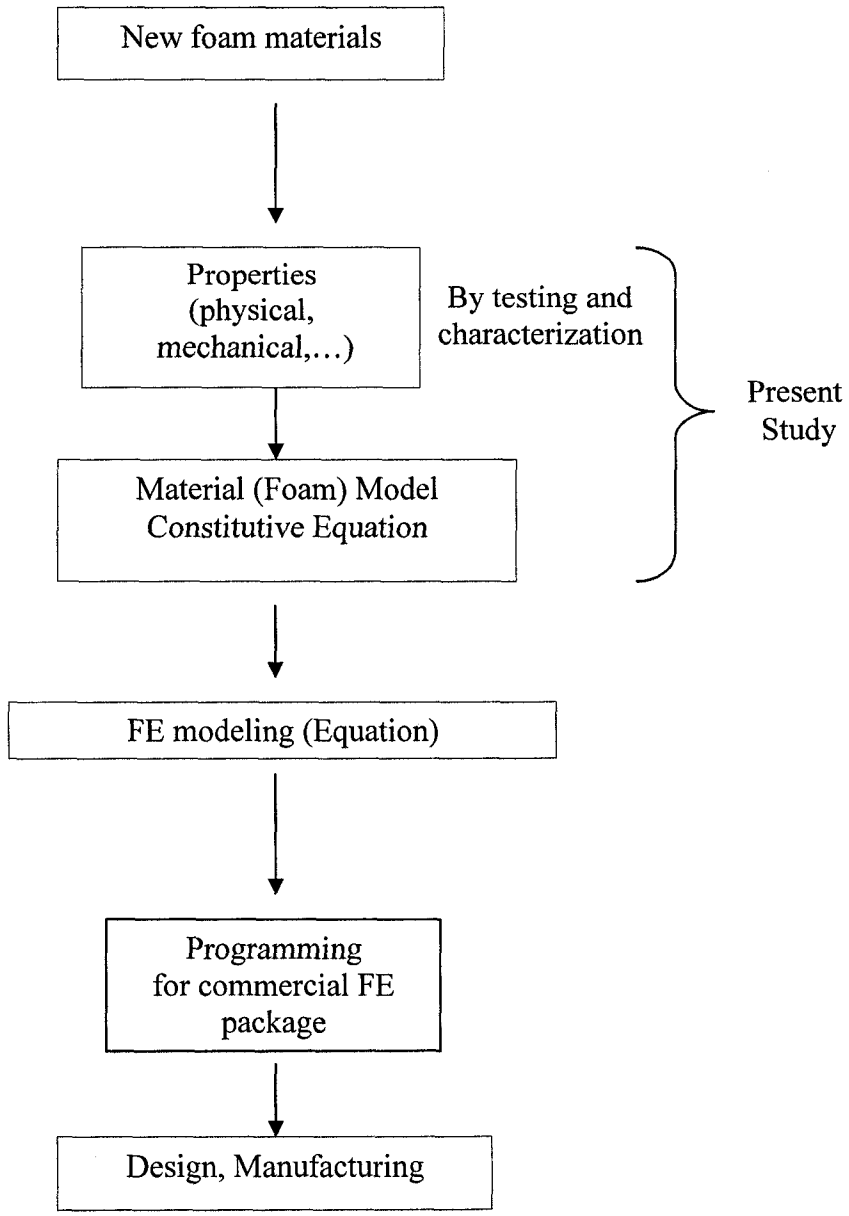

Figure 1.1 Role of constitutive equations on the manufacturing process using new materials.

The following are considered to be principal contributions of this research:

1) The constitutive models developed in this study can be used to predict the nonlinear tensile stress-strain relationship as well as the tensile modulus of polymer/clay nanocomposite foams. The models are used for both nanocomposites and their foams using amorphous or semi-crystalline polymers.

2) General parameters can be used in the constitutive model. In the modulus models, basic material data and some physical properties of foams that can be determined easily by experiment are used. These characteristics enable to set up numerical analysis method for computer simulation.

3) Also, it was found that the constitutive equation obtained from the Maxwell model can be a representative of those by other well known viscoelastic models. The stress-strain behaviors generated from Generalized Maxwell model, Three Element model, and Burgers model can be represented by the constitutive equation using the Maxwell model. In this case, it is required to control only one material parameter (relaxation time constant).

1.6 Organization

On the development of constitutive models, two types of polymer (amorphous polymer and semi-crystalline polymer) are considered. In chapter 3, constitutive models for nonlinear viscoelastic behavior of microcellular foams are studied from various viscoelastic models. Based on these studies a constitutive model for characterizing the tensile behavior of PMMA/clay nanocomposite foams is developed in chapter 4. In the model, the effects of intercalated and agglomerated clays on the tensile properties are considered. Each constitutive model is verified by experiments. PMMA/clay nanocomposite foams are manufactured by batch process method and their uniaxial tensile test results are compared with those by the constitutive model.

As a second part, constitutive models using semi-crystalline polymer are studied. In chapter 5, constitutive models for tensile mechanical behavior of HDPE/clay nanocomposite and its foams are proposed by using micromechanics and intercalated clay model. In order to describe the stress-strain relationship of foams, a viscoelastic model is used. The constitutive model is expressed in terms of microstructural properties of polymer and physical properties of the foams. Also, the influence of nanoclay, foaming conditions on the mechanical properties of the foams is investigated by experiement and the developed constitutive model is verified by experimental data. In chapter 6, the effect of crystallinity and strain rate on the foam morphologies and mechanical properties of HDPE/clay nanocomposite foams are studied by experiment, and these effects are incorporated in the constitutive model. The models are evaluated by experiments using HDPE/clay nanocomposite foams.

Chapter 2

Background

2.1 Constitutive Modeling for Amorphous Polymer

Most polymers or polymeric foams show viscoelastic or viscoplastic behaviors [Bekkour et al. 1998, Ferry 1980, Iannace 2001, Kanny 2002, Riande 2000, Rodriguez-Perez 2000, Sahraoui 2001, and Singh 2003]. To describe the specific mechanical behavior of polymeric foams, the corresponding constitutive law is required for the specific deformation phenomena of the material. In other words, to describe the macroscopic nature of the materials in question, proper constitutive laws are used to govern the distinct types of macroscopic material behaviors.

The modeling for the mechanical behaviour of amorphous polymer has been studied [Hasan and Boyce 1995, Drozdov 1998, Drozdov 2000, Drozdov 2001, Lai et al. 2005, Cho and Kim 2000, Duan 2001]. Constitutive equations for the nonlinear viscoelastic response of amorphous polymers were derived by Drozdov [Drozdov 2000]. The model treats a glassy polymer as an ensemble of independent relaxing regions that randomly hop in their cages being thermally activated. Two features of an amorphous polymer at glassy state are the distributed nature of the microstructural state and the thermally activated evolution of this state. They play a key role in determining its mechanical properties. Based on these natures, a constitutive model was developed by Hasan [Hasan and Boyce 1995]. The model was found to be predictive of the nonlinear viscoelastic-viscoplastic behavior under nonmonotonic loading conditions over a range of strain rates and temperature as well as predictive of the creep behavior over a wide range in stress level at different temperatures. Also, Drozdov [Drozdov 1998, Drozdov 2001] derived a model for the viscoelastic and viscoplastic behaviour of amorphous galssy polymers at isothermal loading with small strains. In this model, amorphous polymer is assumed as heterogeneous at the microscale. It is treated as an ensemble of cooperatively rearranging regions (CRR) which are bridged by links and relax at random times as they are thermally agitated. At the micro-level, the

viscoelastic response of a polymer is reflected by rearrangement of CRRs, whereas the viscoplastic behaviour is associated with coalescence of quasi-point defects and creation of isolated islands of CRRs.

A plastic flow mechanism of glassy polymers was explained in terms of solitons which is expected to unify the existing concepts for viscoelasticity and yield of glassy polymers, such as dislocation, disclination and free volume [Cho and Kim 2000]. Another phenomenological model was proposed by Duan [Duan 2001]. Duan's model has a concise expression of stress dependence on strain, strain rate and temperature. It is capable of uniformly describing the entire range of deformation behavior of glassy and semicrystalline polymers, especially the intrinsic strain softening and subsequent orientation hardening of glassy polymers. This model predicted the compressive behaviour of PMMA and polycarbonate (PC) under various deformation conditions.

2.2 Constitutive Modeling for Semicrystalline Polymers

The viscoelastic response of semicrystalline polymers is conventionally associated with the rearrangement of chains in the amorphous regions. A non-linear viscoelastic model based on rheological and molecular approaches was derived for the time-and rate-dependent responses of a semi-crystalline polymer at isothermal deformation at small strains [Lai et al. 2005]. In the model, the crystalline phase was considered as perfectly elastic. On the other hand, the amorphous phase was treated as an equivalent heterogeneous network of chains which is non-linearly viscoelastic. This model was applied for isotactic polypropylene (iPP).

The modeling of semi-crystalline polymer based on microstructure is faced by representing the properties of crystalline and amorphous materials efficiently. A micromechanically-based constitutive model for HDPE in small deformations is presented by Nikolov and Doghri [Nikolov and Doghri 2000]. Here, a semi-crystalline polymer is modeled as an aggregate of randomly oriented composite inclusions, each consisting of a stack of parallel lamellae with their adjacent amorphous layers. For the amorphous phase, the viscoelastic constitutive behavior is modeled. For the crystalline portion a nonlinear viscoplasticity, single crystal model was chosen. The viscoplastic behavior at yield is incorporated through the constitutive modeling of the crystalline lamellae. The shortcoming

of the phenomenological models is some micromechanical parameters in the model cannot be directly measured despite their physical meaning.

Many micromechanically-based constitutive models for semicrystalline polymers have been studied [van Dommelen et al. 2003, van Dommelen et al. 2004, Drozdov and Christiansen 2003]. A micromechanically-based numerical model for the elasto-plastic deformation and texture evolution of semicrystalline polymers has been developed and used to simulate the mechanical behavior of particle-modified polyethylene [Nikolov and Doghri 2000, Drozdov and Gupta 2003]. To investigate the effect of a specific microstructural morphology on the mechanical behavior of voided systems, a multiscale numerical model is used [van Dommelen et al. 2004]. In this method, polycrystalline model is used for HDPE matrix material. The basic structural element in this model is a layered two-phase composite inclusion, comprising both a crystalline and an amorphous domain. The averaged fields of an aggregate of composite inclusions, having either a random or a preferential orientation, form the constitutive behavior of the polymeric matrix material. A deformation mechanism of oriented polyethylene was investigated by using a multiscale numerical model by van Dommelen et al. [van Dommelen et al. 2003]. The model established a link between the microscopic, the mesoscopic, and the macroscopic levels. In the model, the effect of the macroscopic behaviour of a stacked lamellar microstructure on the tensile behaviour is simulated. Also, the anisotropic mechanical behavior by a stacked lamellar morphology was investigated.

Lee and Paul [Lee and Paul, 2005] developed a model for the mechanical properties of a nanocomposite containing complex inclusions by using the Eshelby's equivalent tensor with a Mori–Tanaka type model. This model permits predictions for sphere, disc, and fiber shaped inclusions, and the influences of the primary and secondary aspect ratios on the effective elastic moduli were examined. However, it is limited to unidirectionally aligned inclusions. The effect of the nanoparticles on the elastic modulus of polymer/clay nanocomposites has been studied experimentally [Luo and Daniel 2003, Cho and Paul 2001, Lee and Goettler 2004, Vu et. al 2004, Kuo 2005, Murphy et. al 2003]. Some micromechanically-based constitutive models for semicrystalline polymers have been studied [Dommelen et. al 2003, Dommelen et. al 2004, Drozdov and Christiansen 2003].

Microstructural concept and RVE (representative volume element) can be used for modeling of polymer composites. Lee et al. [Lee and Ghosh 1999] proposed a continuum level elastic–plastic constitutive modeling method for composite and porous materials. It is based on two-scale analysis using the asymptotic homogenization method and the Voronoi cell finite element model for detailed microstructural analysis. The linear elastic behavior of the heterogeneous materials is represented by an orthotropic elasticity tensor. For the isotropic hardening plasticity with associate flow rule representation, a pressure-dependent yield function with strain and plastic work dependent parameters is postulated. This constitutive model is ideal for applications in hierarchical multiple-scale analysis of heterogeneous materials.

In addition to the viscoelastic behavior, semicrystalline polymers can be subject to large plastic deformation process accompanying high anisotropy due to preferential orientation of macromolecules. Many experimental investigation and modeling of plastic deformation of semi-crystalline polymers have been studied [Nikolov and Doghri 2000, van Dommelen et al. 2003, Lee et al. 1993, Nitta and Yamaguchi 1998, Spathis and Kontou 1998]. A micromechanically based composite model was also proposed for large plastic deformation and texture evolution of semi-crystalline polymers [Lee and Ghosh 1999], where an aggregate of two-phase composite inclusions is used in modeling and the molecular chain inextensibility within the crystalline phase is considered. Interface compatibility and traction equilibrium are enforced within each composite inclusion. In the constitutive equations, the lack of live independent slip systems in the crystalline phase is accounted. Also, the effect of molecular alignment is included in the constitutive law for the amorphous phase. These composite models are used to predict stress strain behavior and texture evolution in isotropic HDPE under different modes of straining.

Several constitutive models for HDPE have been developed. The viscoplasticity theory based on overstress for polymers is applied for the simulation of the relaxation and creep behaviors of solid HDPE [Khan and Krempl 2006]. Of considerable significance is the model's ability to represent amorphous and semicrystalline polymers. Also, the time-dependent behavior of HDPE was modeled by using a one-dimensional integral representation [Lai and Bakker 1995]. Owing to the plasto-viscoelastic behavior of the material, the total strain is assumed to be decomposed into a recoverable viscoelastic strain

and an irrecoverable plastic strain. The viscoelastic deformation is represented by the Schapery thermodynamic theory. The plastic deformation is assumed to be accumulated during the loading history. An effective time concept is introduced for the plastic deformation, so that the response due to complex loading can be accounted for. This model represents a prediction of the responses of creep and recovery, two-step creep, and constant stress rate loading and unloading. Based on the experimental data, two uniaxial constitutive models were constructed by Zhang [Zhang and Moore 1997] for HDPE. The first, a nonlinear viscoelastic model, is formulated using the mechanical analogy consisting of one independent spring and six Kelvin elements in series. Creep data are used to determine the model parameters. The second model, a viscoplastic formulation, is developed using the viscoplastic theory proposed by Bodner to characterize the uniaxial viscoplastic behaviour of metals. Inelastic strain rate is introduced into the state variable in addition to inelastic work to depict the strong rate dependent behavior of HDPE. A multiscale numerical model is used to investigate the mechanics of intraspherulitic deformation of polyethylene [van Dommelen et al. 2003]. Constitutive properties of the material are identified for the crystallographic and amorphous domains. The averaged fields of an aggregate of individual phases, having preferential orientations, form the constitutive behavior of intraspherulitic material. This model includes the geometrical effect of the anisotropic structure within a spherulite, causing strain concentrations in the centers, which spread out in the equatorial region for uniaxial loading conditions and in inclined directions for plane strain loading. The deformations are linked to microstructural processes as interlamellar deformation and intralamellar crystallographic slip.

For the time-dependent behavior of semicrystalline polymers at isothermal loading with small strains, Drozdov [van Dommelen et al. 2003] modeled a semicrystalline polymer as a network of macromolecules bridged by junctions (physical crosslinks, entanglements, and crystalline lamellae) that can slide with respect to their reference positions in the bulk material under straining. The network is assumed to be highly inhomogeneous, and it is modeled as an ensemble of mesoregions (MRs) with various strengths of interchain interaction. The viscoelastic response of a semicrystalline polymer reflects reformation of strands in active MRs, whereas its viscoplastic behavior is associated with sliding of junctions. For small stress–strain relations for uniaxial deformation, the law of

thermodynamics using the Clausius–Duhem inequality was adopted. Also, Drozdov [Drozdov and Christiansen, 2003] derived a constitutive equation for the viscoplastic behavior of semicrystalline polymers at finite strains. The rate of sliding in viscoplastic behavior is assumed to be proportional to the average stress in strands linked to non-affine junctions. The constitutive equations are applied to the analysis of uniaxial tension, uniaxial compression and simple shear of an incompressible medium.

Nitta [Nitta and Yamaguchi 1998] proposed a method for the analysis of stress-strain curves for crystalline polymers such as polypropylene and polyethylene, in which the plastic deformation and the anharmonicity of the spring constant are taken into account. This method makes possible the evaluation of the plastic deformation as well as the nonlinear viscoelasticity. Drozdov [Drozdov and Christiansen 2003] derived a constitutive model for the viscoplastic behavior of a semicrystalline polymer at small strains.

2.3 Polymer/Clay Nanocomposites

The constitutive models mentioned so far are for semi-crystalline polymers without nano fillers. The influence of the nanoparticles on the constitutive modeling is also required. Studies on the influence of the nanoparticles on the constitutive modeling of semicrystalline polymer nanocomposites are increasing. However, only few models for HDPE/clay nanocomposites have been reported [Osman et. al 2005, Zhong and Kee 2005, Luo and Daniel 2003, Sheng et. al 2004, Drozdov and Christiansen 2007]. Moreover, little study has been performed for the constitutive modeling of the polymer/clay nanocomposite foams.

In the case of using HDPE, Nikolov et al. [Nikolov et. al 2002] proposed a multi-scale constitutive model for small deformations of semicrystalline polymers, where viscoelastic and viscoplastic models were used for crystalline lamellae and amorphous phase behavior, respectively. A constitutive model is derived for the viscoplastic response of polyethylene/montmorillonite clay nanocomposite at three-dimensional cyclic deformations with small strains [Drozdov and Christiansen 2007]. The study focuses on low-cycle deformation. Luo [Luo and Daniel 2003] developed a three-phase model including the epoxy matrix, the exfoliated clay nanolayers and the nanolayer clusters. In the model, the region consisting of matrix with exfoliated clay nanolayers or platelets is analyzed by assuming

near uniform dispersion and random orientation. The properties of intercalated clusters of clay platelets are calculated by a rule of mixtures based on a parallel platelet system. The Mori–Tanaka method is applied to calculate the modulus of the nanocomposite as a function of various parameters, including the exfoliation ratio, clay layer and cluster aspect ratios, d-spacing, intragallery modulus, matrix modulus and matrix Poisson's ratio. When HDPE is melt compounded with an organically modified montmorillonite, the composite film involves intercalated clay particles, where the clay enhancing effects apply mainly to the modulus, instead of to the strength [Zhong and Kee 2005]. Also, the influence of the organic monolayer structure on the exfoliation of montmorillonite and the tensile properties of the HDPE/organo-montmorillonites nanocomposites was studied [Osman et al. 2005]. The tensile properties were correlated to the volume fraction of the inorganic part of the nanocomposites. A multiscale modeling strategy was employed to account for the hierarchical morphology of the nanocomposite [Sheng et al. 2004]. These geometric features of clays together with estimates of silica lamina stiffness provide a basis for modeling effective mechanical properties of the clay particle. In the case of the semi-crystalline matrices, the transcrystallization behavior induced by the nanoclay is taken into account by modeling a layer of matrix surrounding the particle to be highly textured and therefore mechanically anisotropic. Micromechanical models based on the 'effective clay particle' were employed to calculate the overall elastic modulus of the amorphous and semi-crystalline polymer/clay nanocomposites and to compute their dependence on the matrix and clay properties as well as internal clay structural parameters.

Chapter 3

Tensile Behavior of Microcellular Polymer Foams[1]

3.1 Introduction

In order to describe the macroscopic nature of the materials in question, proper constitutive laws governing the distinct types of macroscopic material behaviors are necessary. Fractional constitutive equations on the basis of viscoelastic models such as the Maxwell model and Kelvin-Voigt model were derived [Schiessel et al. 1995], where each model was changed to generalized form using fractional elements. If a finite number of basic viscoelastic elements is used with a finite distribution of delay or relaxation times, the relationship between stress and strain can be obtained by a fractional model; Hernandez-Jimenez et al. [Hernandez-Jimenez et al. 2002] studied this method using the Maxwell model. A fractional viscoelastic constitutive equation using the three parameter model was studied [Schmidt and Gaul 2002] and the adaptive capability of the equation to viscoelastic moduli by experiment was demonstrated. In search for a different method to express the nonlinear viscoelastic behavior of thermorheologically complex materials, Klompen and Govaert [Klompen and Govaert 1999] considered stress-dependent viscosity in Generalized Maxwell model and applied it to PMMA. Also, nonlinear viscoelastic models based on free volume considerations were used as constitutive models [Arzoumanidis and Liechti 2003], in which the effect of stress and strain on the free volume was considered and compared to tensile experimental data at various rates.

Convolution integral forms are sometimes used to describe the dynamic behavior of viscoelastic properties of foams [Singh et al. 2003, White et al. 2000]. Notably, the time-dependent response of a viscoelastic material has been expressed by convolution integral called Boltzmann superposition integral [Christensen 1982]. Lu and Zhang [Lu and Zhang

[1]Reproduced from: C. Jo, J. Fu and H.E. Naguib, Constitutive modeling for mechanical behavior of PMMA microcellular foams, Polymer 2005, 46(25): 11896-11903.

2004] showed a constitutive relation expressed in terms of relative density and strain, using the Boltzmann integral, and applied it for the tensile behavior of microcellular polycarbonate.

In this chapter, constitutive equations for nonlinear tensile behavior of amorphous foams are studied. The modeling is presented in terms of foam parameters such as foam density and volume fraction of solid contained in the cell edges. The application of the constitutive model is confined to only tensile behavior of foams which show viscoelastic property. Also, experimental work to verify the constitutive model is performed. PMMA microcellular foams are manufactured using batch process method and tensile tests results of the foams are compared with the constitutive model.

3.2 Constitutive Models for Nonlinear Elastic Behavior of Foams

Several constitutive equations were derived from viscoelastic models to describe the tensile stress-strain behavior of PMMA foams.

3.2.1 Constitutive equation using Maxwell model

In the Maxwell model (Fig. 3.1(a)), the spring and dashpot represent the elastic response and the time-dependent response, respectively, where E is elastic modulus and η is defined as viscosity modulus. The governing equation of the model is expressed as:

$$\dot{\sigma} + \frac{E}{\eta}\sigma = E\dot{\varepsilon} \tag{3.1}$$

where σ is the stress on both spring and dashpot, and ε is the total strain of the model. From Eq. (3.1), a constitutive equation is derived, providing strain rate is constant, as:

$$\sigma(t) = \eta\dot{\varepsilon}\left[1 - \exp\left(-\frac{E}{\eta}t\right)\right]. \tag{3.2}$$

The relationship between E and η is obtained from Fig. 3.1(a):

$$\eta = \frac{\varepsilon_s}{\dot{\varepsilon}_d}E \tag{3.3}$$

where ε_s and ε_d are the strains shown by the spring component and the dashpot component, respectively. In nonlinear behavior, the modulus of viscosity η is dependent on the stress during the deformation [Klompen and Govaert 1999].

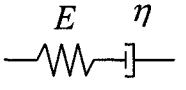

(a) Maxwell model

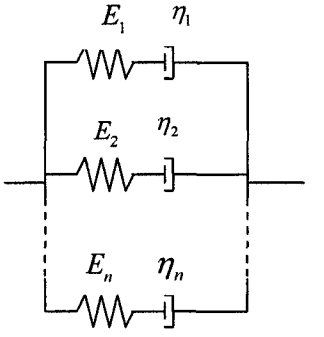

(b) Generalized Maxwell model

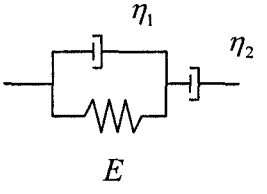

(c) Three Element model

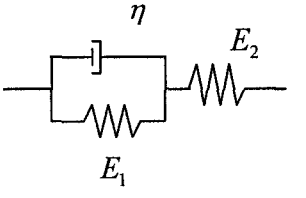

(d) Three Element Standard Solid

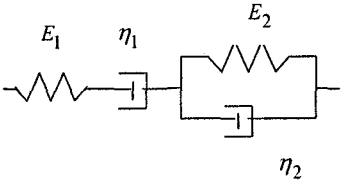

(e) Burgers model

Figure 3.1 Viscoelastic models

However, in this model, a constant value of modulus of viscosity is assumed during the small elastic deformation. In other words, η is accounted as a material parameter not processing parameter. Thus, the ratio of ε_s and $\dot{\varepsilon}_d$ could be considered as a constant and is represented using the relaxation time constant expressed as $\tau = \eta / E$, where τ is a material property determined experimentally. If the time variable is replaced by strain using the relationship $\varepsilon = \dot{\varepsilon} t$, the stress is expressed as a function of strain and strain rate:

$$\sigma = \eta \dot{\varepsilon} \left[1 - \exp\left(-\frac{\varepsilon}{\tau \dot{\varepsilon}} \right) \right] . \tag{3.4}$$

The equivalent elastic modulus E_{eq} is obtained from Eq. (3.4) and it can be counted as the elastic modulus of foams, E^*:

$$E_{eq}(= E^*) = \left. \frac{d\sigma}{d\varepsilon} \right|_{\varepsilon \to 0} = E . \tag{3.5}$$

Eventually, the constitutive equation is expressed as a function of strain, elastic modulus of foams, time constant τ, and strain rate:

$$\sigma = E^* \tau \dot{\varepsilon} \left[1 - \exp\left(-\frac{\varepsilon}{\tau \dot{\varepsilon}} \right) \right] . \tag{3.6}$$

By expressing E^* and τ as function of foam properties, the constitutive equation can be represented in terms of foam properties such as the relative density of foams.

3.2.2 Constitutive equation using Generalized Maxwell model

Using the Riesz representation theorem [Riesz and Sz.-Nagy 1955], the stress tensor expressed by strain history can be changed to the Stieltjes integral form, and from the integral the stress constitutive equation is obtained with variable changes [Christensen 1982]:

$$\sigma(t) = \int_0^t E(t - t') \dot{\varepsilon}(t') dt' . \tag{3.7}$$

E is defined as a relaxation function which represents modulus. Since the force on each pair of Generalized Maxwell model (Fig. 3.1(b)) relaxes exponentially, the modulus is expressed as [Riande 2000]:

$$E(t - t') = \sum_{i=1}^{n} E_i \exp\left(-\frac{(t - t')}{\tau_i} \right) \tag{3.8}$$

in which the relaxation time constant τ_i is defined as $\tau_i = \eta_i / E_i$. Accordingly, the constitutive equation is obtained providing $\dot{\varepsilon}$ = constant and $t = \varepsilon/\dot{\varepsilon}$ as:

$$\sigma = \sum_{i=1}^{n} E_i \tau_i \dot{\varepsilon} \left[1 - \exp\left(-\frac{\varepsilon}{\tau_i \dot{\varepsilon}} \right) \right] . \tag{3.9}$$

Eq. (3.9) contains the concepts of convolution integral and fractional model. Since the stress in Generalized Maxwell model is the sum of the stresses of each Maxwell model component, the stress in Eq. (3.9) can also be obtained from Eq. (3.4) by summation of each stress component:

$$\sigma = \sum_{i=1}^{n} \sigma_i = \sum_{i=1}^{n} \eta_i \dot{\varepsilon} \left[1 - \exp\left(-\frac{\varepsilon}{\tau_i \dot{\varepsilon}} \right) \right] . \tag{3.10}$$

The equivalent elastic modulus of the Generalized Maxwell model is obtained from Eq. (3.9);

$$E_{eq} (= E^*) = \left. \frac{d\sigma}{d\varepsilon} \right|_{\varepsilon \to 0} = \sum_{i=1}^{n} E_i \tag{3.11}$$

If $\eta_i = \eta$ and $E_i = E$, as a special case of the Generalized Maxwell model, $E^* = nE$ and $\tau_i = \frac{\eta}{E} (= \tau)$. Then, Eq. (3.9) becomes

$$\sigma = nE\tau\dot{\varepsilon} \left[1 - \exp\left(-\frac{\varepsilon}{\tau\dot{\varepsilon}} \right) \right] = E^* \tau \dot{\varepsilon} \left[1 - \exp\left(-\frac{\varepsilon}{\tau\dot{\varepsilon}} \right) \right] . \tag{3.12}$$

This corresponds to the constitutive equation by the Maxwell model (Eq. (3.6)). As another case, when $n = 2$, Eq. (3.9) is expanded to:

$$\sigma = E_1 \tau_1 \dot{\varepsilon} \left[1 - \exp\left(-\frac{\varepsilon}{\tau_1 \dot{\varepsilon}} \right) \right] + E_2 \tau_2 \dot{\varepsilon} \left[1 - \exp\left(-\frac{\varepsilon}{\tau_2 \dot{\varepsilon}} \right) \right] \tag{3.13}$$

where $E^* = E_1 + E_2$, $\tau_1 = \frac{\eta_1}{E_1}$ and $\tau_2 = \frac{\eta_2}{E_2}$. For more simplicity, if E_1 is assumed equal to E_2, then Eq. (3.13) is:

$$\sigma = \frac{E^*}{2} \tau_1 \dot{\varepsilon} \left[1 - \exp\left(-\frac{\varepsilon}{\tau_1 \dot{\varepsilon}} \right) \right] + \frac{E^*}{2} \tau_2 \dot{\varepsilon} \left[1 - \exp\left(-\frac{\varepsilon}{\tau_2 \dot{\varepsilon}} \right) \right] \tag{3.14}$$

in which $E^* = E_1 + E_1 = 2E_1$. Eq. (3.14) becomes the constitutive equation obtained from the Maxwell model when $\tau_1 = \tau_2$. Despite $\tau_1 \neq \tau_2$, it was proved that by choosing proper values of τ_1 and τ_2 in Eq. (3.14), the same stress-strains curves as those by the Maxwell model (Eq.

(3.6)) are made; where $\tau_1 + \tau_2 \geq \tau$ is always maintained. This rule is applied to all n in the Generalized Maxwell model. For the cases of $n = 2$ and $n = 3$, the stress-strain curves of Eq. (3.9) are plotted and compared with the one by the Maxwell model (Eq. (3.6)) in Fig. 3.2, where E^* are the same in all three curves. For the plot of Eq. (3.6) in Fig. 3.2, the τ was determined so that the theoretical curve can fit roughly to the experimental data. Also, the values of E^* and $\dot{\varepsilon}$ were obtained from experimental data and Eq. (3.30). In order to match to the stress-strain curve by Maxwell model, the Generalized Maxwell model (n=2) can have many pairs of τ_1 and τ_2, however only one pair ($\tau_1 = 47$ and $\tau_2 = 100$) was specified in Fig. 3.2. The Generalized Maxwell model with n=3 was also used by the same method as n=2. From Fig. 3.2, it is clear that the constitutive equation by the Generalized Maxwell model created the same stress-strain behavior as the Maxwell model with only different time constants. Fig. 3.3 shows the stress-strain curves by the Generalized Maxwell model with each different E_i and τ_i. Similarly in Fig. 3.2, the same value of E^* were used for all three curves in Fig. 3.3. It was also proved in the figure that if the same equivalent elastic modulus is used in both models, any form of the constitutive equation by the Generalized Maxwell model can describe the stress-strain behavior made by the Maxwell model. In other words, the behavior of Eq. (3.9) almost coincides with that of Eq. (3.6) if proper combinations of E_i and τ_i are used in Eq. (3.9).

3.2.3 Constitutive equation using Three Element model

The equation of motion of the Three Element model (Fig. 3.1(c)) is:

$$\dot{\sigma} + \frac{E}{\eta_1 + \eta_2}\sigma = \frac{E\eta_2}{\eta_1 + \eta_2}\dot{\varepsilon} + \frac{\eta_1\eta_2}{\eta_1 + \eta_2}\ddot{\varepsilon} \quad . \tag{3.15}$$

Assuming that $\dot{\varepsilon} =$ constant and $\ddot{\varepsilon} = 0$, a constitutive equation is derived using the similar procedures as in section 3.2.1:

$$\sigma = \eta_2\dot{\varepsilon}\left[1 - \exp\left(-\frac{E}{\eta_1 + \eta_2}\frac{\varepsilon}{\dot{\varepsilon}}\right)\right] . \tag{3.16}$$

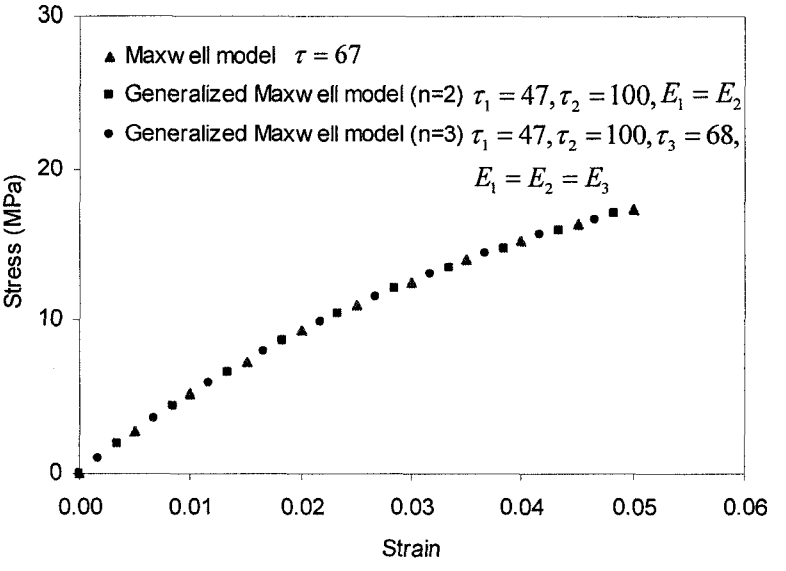

Figure 3.2 Comparison of the constitutive equations by Generalized Maxwell model with that by Maxwell model.

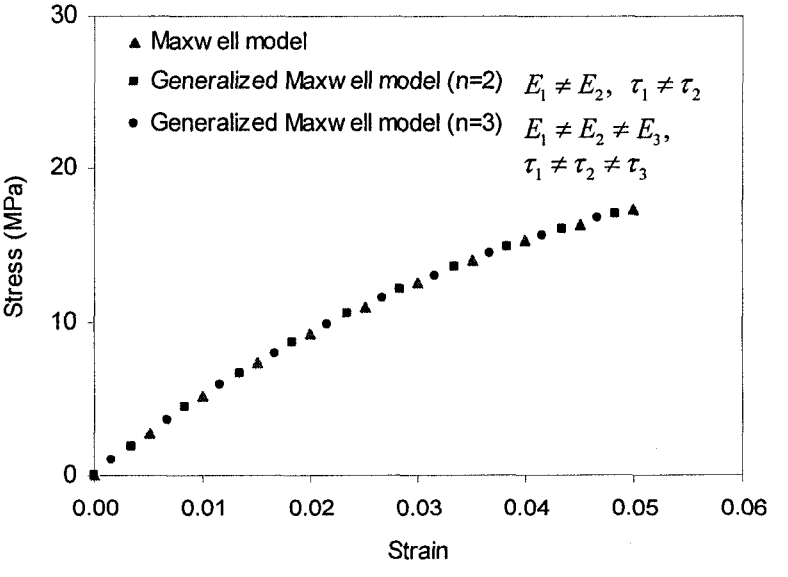

Figure 3.3 Comparison of the constitutive equations by Generalized Maxwell model (each different E_i and τ_i) with that by Maxwell model.

If the relaxation time constant is set as $\tau = \frac{\eta_1 + \eta_2}{E}$,

$$\sigma = \eta_2 \dot{\varepsilon}\left[1 - \exp\left(-\frac{\varepsilon}{\tau\dot{\varepsilon}}\right)\right] . \tag{3.17}$$

The equivalent elastic modulus is calculated in the same method:

$$E_{eq}(= E^*) = \left.\frac{d\sigma}{d\varepsilon}\right|_{\varepsilon \to 0} = \frac{\eta_2}{\eta_1 + \eta_2} E \tag{3.18}$$

From Eqs. (3.17) and (3.18), the constitutive equation by the Three Element model is:

$$\sigma = E^* \tau\dot{\varepsilon}\left[1 - \exp\left(-\frac{\varepsilon}{\tau\dot{\varepsilon}}\right)\right] \tag{3.19}$$

which is identical to the constitutive equation by the Maxwell model. This means that even if the values of the components E and η are different between the Maxwell model and the Three Element model, the stress-strain behaviors by both models are coincident with each other if and only if E^* and τ are the same in both models. The expressions of E and η are also summarized in Table 3.1.

3.2.4 Constitutive equation using Three Element Standard solid

The equation of motion of the Three Element Standard Solid (Fig. 3.1(d)) is:

$$\dot{\sigma} + \frac{E_1 + E_2}{\eta}\sigma = \frac{E_1 E_2}{\eta}\varepsilon + E_2\dot{\varepsilon} . \tag{3.20}$$

The corresponding constitutive relation is obtained from Eq. (3.20) as:

$$\sigma = \frac{E_1 E_2}{E_1 + E_2}\varepsilon - \frac{E_2}{E_1 + E_2}\eta\dot{\varepsilon}\left(\frac{E_1}{E_1 + E_2} - 1\right)\left[1 - \exp\left(-\frac{E_1 + E_2}{\eta}\frac{\varepsilon}{\dot{\varepsilon}}\right)\right] . \tag{3.21}$$

The equivalent elastic modulus is:

$$E_{eq}(= E^*) = \left.\frac{d\sigma}{d\varepsilon}\right|_{\varepsilon \to 0} = E_2 . \tag{3.22}$$

If the relaxation time constant is set as $\tau = \frac{\eta}{E_1 + E_2}$, then

$$\sigma = \frac{E_1 E_2}{\eta}\tau\varepsilon - E_2\tau\dot{\varepsilon}\left(\frac{E_1}{\eta}\tau - 1\right)\left[1 - \exp\left(-\frac{\varepsilon}{\tau\dot{\varepsilon}}\right)\right] . \tag{3.23}$$

Table 3.1 Summary of constitutive equations and equivalent elastic modulus for foams.

Type of model	Equivalent elastic modulus of foams	Relaxation time constant	Constitutive equations
Maxwell	$E^* = E$	$\tau = \frac{\eta}{E}$	$\sigma = E^*\tau\dot{\varepsilon}\left[1-\exp\left(-\frac{\varepsilon}{\tau\dot{\varepsilon}}\right)\right]$
Generalized Maxwell ($E_i = E$, $\eta_i = \eta$)	$E^* = nE$	$\tau = \frac{\eta}{E}$	
Three Element (E, η_1, η_2)	$E^* = \frac{\eta_2}{\eta_1+\eta_2}E$	$\tau = \frac{\eta_1+\eta_2}{E}$	
Generalized Maxwell	$E^* = \sum_{i=1}^{n} E_i$	$\tau_i = \frac{\eta_i}{E_i}$	$\sigma = \sum_{i=1}^{n} E_i\tau_i\dot{\varepsilon}\left[1-\exp\left(-\frac{\varepsilon}{\tau_i\dot{\varepsilon}}\right)\right]$
Burgers	$E^* = -\frac{\eta_1^2}{\eta_1+\eta_2}\lambda_1 - \frac{\eta_1\eta_2}{\eta_1+\eta_2}\lambda_2$ where $\lambda_{1,2} = \frac{1}{2\eta_1\eta_2}\times\left(-B\pm\sqrt{B^2-4AC}\right)$		$\sigma = \eta_1\dot{\varepsilon} + \left[-\eta_1\dot{\varepsilon} + \frac{1}{\lambda_1-\lambda_2}\left(E^* + \frac{E_1E_2}{\lambda_2\eta_2\dot{\varepsilon}}\right)\right]e^{\lambda_1\varepsilon} - \frac{1}{\lambda_1-\lambda_2}\left(E^* + \frac{E_1E_2}{\lambda_2\eta_2\dot{\varepsilon}}\right)e^{\lambda_2\varepsilon}$ where $\lambda_{1,2} = \frac{1}{2\eta_1\eta_2\dot{\varepsilon}}\left(-B\pm\sqrt{B^2-4AC}\right)$, $A = \eta_1\eta_2$, $B = E_2\eta_1 + E_1(\eta_1+\eta_2)$, $C = E_1E_2$ or $\sigma = \eta_1\dot{\varepsilon}\left[1-\frac{\eta_1}{\eta_1+\eta_2}\exp\left(\lambda_1\frac{\varepsilon}{\dot{\varepsilon}}\right) - \frac{\eta_2}{\eta_1+\eta_2}\exp\left(\lambda_2\frac{\varepsilon}{\dot{\varepsilon}}\right)\right]$ where $\lambda_{1,2} = \frac{1}{2\eta_1\eta_2}\left(-B\pm\sqrt{B^2-4AC}\right)$
Three Element Standard Solid (E_1, E_2, η)	$E^* = E_2$	$\tau = \frac{\eta}{E_1+E_2}$	$\sigma = E^*\varepsilon - \frac{E^{*2}\tau}{\eta}\varepsilon + \frac{E^{*2}\tau^2\dot{\varepsilon}}{\eta}\left[1-\exp\left(-\frac{\varepsilon}{\tau\dot{\varepsilon}}\right)\right]$

Using the relationship, $E_1 = \frac{\eta}{\tau} - E_2$ and $E^* = E_2$, the constitutive equation is expressed as:

$$\sigma = E^*\varepsilon - \frac{E^{*2}\tau}{\eta}\varepsilon + \frac{E^{*2}\tau^2\dot{\varepsilon}}{\eta}\left[1 - \exp\left(-\frac{\varepsilon}{\tau\dot{\varepsilon}}\right)\right]. \tag{3.24}$$

As shown in Fig. 3.4, the stress-strain curves by Eq. (3.24) are getting closer to that made by the Maxwell model as E_1 becomes small. The three curves (τ = 45, τ = 25, and τ = 10) in Fig. 3.4 were made so that their tensile strengths at strain rate 0.05 are the same to that by the Maxwell model. Under this condition τ is always smaller than that of Maxwell model provided E_1 is positive. To the given τ, numerous pairs of η and E_1 exist. In Fig. 3.4, one of those was chosen and specified for each τ. If one of η or E_1 is determined, the other is calculated by $E_1 = \frac{\eta}{\tau} - E_2$ or $\tau = \frac{\eta}{E_1 + E_2}$. If the same τ (=67) is used, the stresses by the Three Element Standard Solid model are always greater than that by the Maxwell model unless E_1 is negative. In other words, the stress-strain behavior by the Three Element Standard Solid has more strain hardening phenomenon than the Maxwell model.

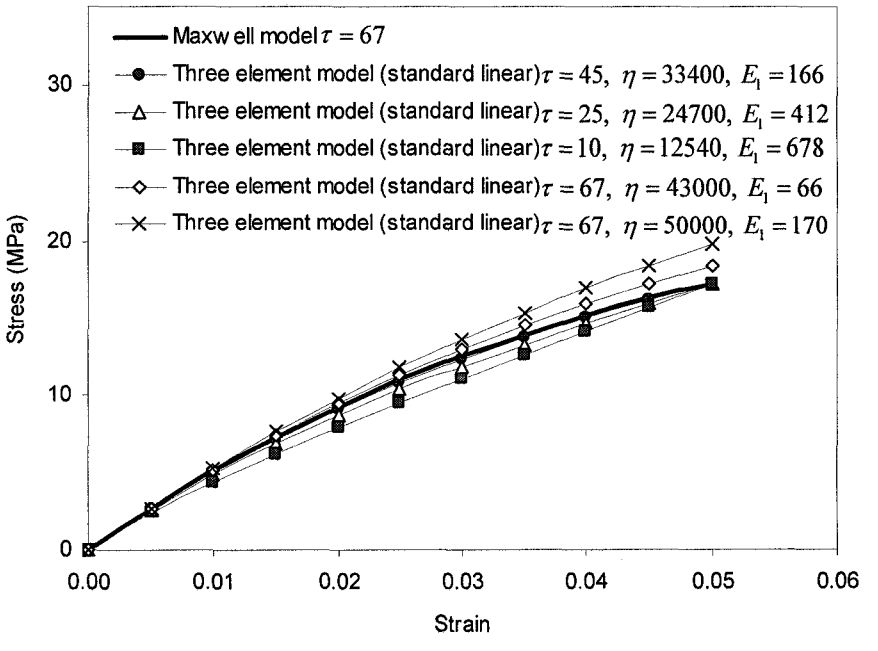

Figure 3.4 Comparison of the constitutive equations of foams by Three Element Standard Solid ($E^* = E_2$ = 576 MPa) with that by Maxwell model (E^* = 576 MPa).

3.2.5 Constitutive equation using Burgers model

The equation of motion of the Burgers model (Fig. 3.1(e)) is:

$$\eta_1\eta_2\ddot{\sigma}+\left[E_2\eta_1+E_1(\eta_1+\eta_2)\right]\dot{\sigma}+E_1E_2\sigma=E_1E_2\eta_1\dot{\varepsilon}+E_1\eta_1\eta_2\ddot{\varepsilon}\ . \tag{3.25}$$

If the strain rate is considered as a constant during the tensile deformation, the constitutive equation is expressed as:

$$\sigma=-\frac{\eta_1^{\,2}}{\eta_1+\eta_2}\dot{\varepsilon}e^{\lambda_1\frac{\varepsilon}{\dot{\varepsilon}}}-\frac{\eta_1\eta_2}{\eta_1+\eta_2}\dot{\varepsilon}e^{\lambda_2\frac{\varepsilon}{\dot{\varepsilon}}}+\eta_1\dot{\varepsilon} \tag{3.26}$$

where, $\lambda_{1,2}=\frac{1}{2\eta_1\eta_1}\left(-B\pm\sqrt{B^2-4AC}\right)$, $A=\eta_1\eta_2$, $B=E_2\eta_1+E_1(\eta_1+\eta_2)$, $C=E_1E_2$ and $D=E_1E_2\eta_1$.

The equivalent elastic modulus is

$$E_{eq}(=E^*)=\left.\frac{d\sigma}{d\varepsilon}\right|_{\varepsilon\to 0}=-\frac{\eta_1^{\,2}}{\eta_1+\eta_2}\lambda_1-\frac{\eta_1\eta_2}{\eta_1+\eta_2}\lambda_2\ . \tag{3.27}$$

In order to E^* be shown in the constitutive equation, Eq. (3.25) can be solved by the Laplace transformation method with initial conditions $\sigma(0)=0$ and $\dot{\sigma}(0)=E_{eq}$.

$$\sigma=\eta_1\dot{\varepsilon}+\left[-\eta_1\dot{\varepsilon}+\frac{1}{\lambda_1-\lambda_2}\left(E^*+\frac{E_1E_2}{\lambda_2\eta_2\dot{\varepsilon}}\right)\right]e^{\lambda_1\varepsilon}-\frac{1}{\lambda_1-\lambda_2}\left(E^*+\frac{E_1E_2}{\lambda_2\eta_2\dot{\varepsilon}}\right)e^{\lambda_2\varepsilon} \tag{3.28}$$

where $\lambda_{1,2}=\frac{1}{2\eta_1\eta_2\dot{\varepsilon}}\left(-B\pm\sqrt{B^2-4AC}\right)$.

If the value of η_1 is chosen equal to η_2 in the model, the magnitude of the equivalent elastic modulus is determined only by E_1 and E_2:

$$E_{eq}(=E^*)=\left.\frac{d\sigma}{d\varepsilon}\right|_{\varepsilon\to 0}=\frac{E_2}{2}+E_1 \qquad (\text{when } \eta_1=\eta_2)\ . \tag{3.29}$$

The shape of the stress-strain curves are dependent on $\eta_1\ (=\eta_2)$ provided the equivalent elastic modulus is not changed. The stress-strain curves in this case are plotted in Fig. 3.5 and compared with those of the Maxwell model, where the equivalent elastic modulus in both models is the same. As shown in Fig. 3.5, the stress-strain curves by Burgers model are almost identical to the Maxwell model's even though there are slight differences at low time constant τ.

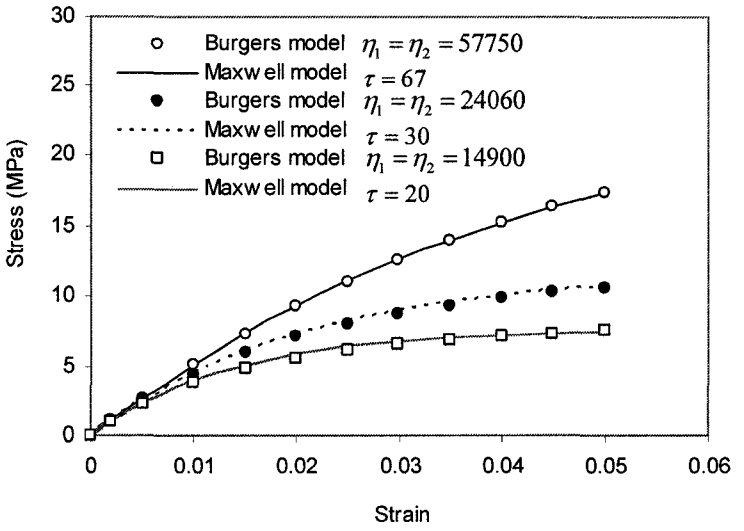

Figure 3.5 Comparison of the constitutive equations of foams by Burgers model with that by Maxwell model.

Summary of the constitutive equations studied in this chapter and their equivalent elastic moduli for foams are listed in Table 3.1. The characteristics of those equations are that the relaxation time constant and the equivalent elastic modulus play important roles in every constitutive equation. By comparing the constitutive equations studied in this chapter, it is proved that the constitutive equation by the Maxwell model could be a representative one. To verify the relevance of the constitutive equation, experimental work has been performed to compare with the theoretical results.

3.3 Experimental

In order to obtain the stress-strain curves by experiment, PMMA closed cell microcellular foams were manufactured in a batch process method [Fu et al. 2005] and then uniaxial tensile tests were performed.

3.3.1 Materials

PMMA with a M_w = 108,500 and a M_n = 56,700 was supplied by Canus Plastics. Before use the samples were dried at a temperature of 90°C for at least 24 hours. With the use of a hydraulic, heated, press (Carver, Inc) machine, PMMA resins were molded into 1.5 mm thick panels by hot compression molding, where five tons of pressure was applied for four minutes. The temperature of the hot pressing plates was 180°C. Rectangular strips were obtained from the mold with dimensions of 6 mm × 50 mm. The blowing agent used in this study was carbon dioxide obtained from Praxair-Inc.

3.3.2 Foaming experiment

The foaming experiments were performed by a batch process. The schematic diagram is shown in Fig. 3.6. First, the polymer samples were saturated in a high pressure CO_2 chamber at a pressure of 3.8 – 5.8 MPa and at room temperature (21°C – 23°C). The saturation time, which varies from one day to two weeks, was calculated according to the diffusion coefficient of the carbon dioxide in PMMA [Handa et al. 2001]. In the next stage, the saturated samples were put in a water bath with selected temperature for 5 – 20 seconds. The rapid change in temperature and pressure induced cell nucleation and cell growth [Baldwin 1996, Park 1995]. Afterwards, the samples were put in cold water to fix the foam morphology.

3.3.3 Sample characterization

The samples were air dried for 7 days before testing. The foam density was measured by a buoyancy method using a density determination kit supplied by Denver Instrument. The gravity of unfoamed samples was measured in distilled water and in the air. The Archimedean principle was applied for determining the specific gravity of the foams. The relative foam density is defined as the ratio of the foam density and the unfoamed polymer density. The expansion ratio is defined as the ratio of the unfoamed polymer density to the foam density.

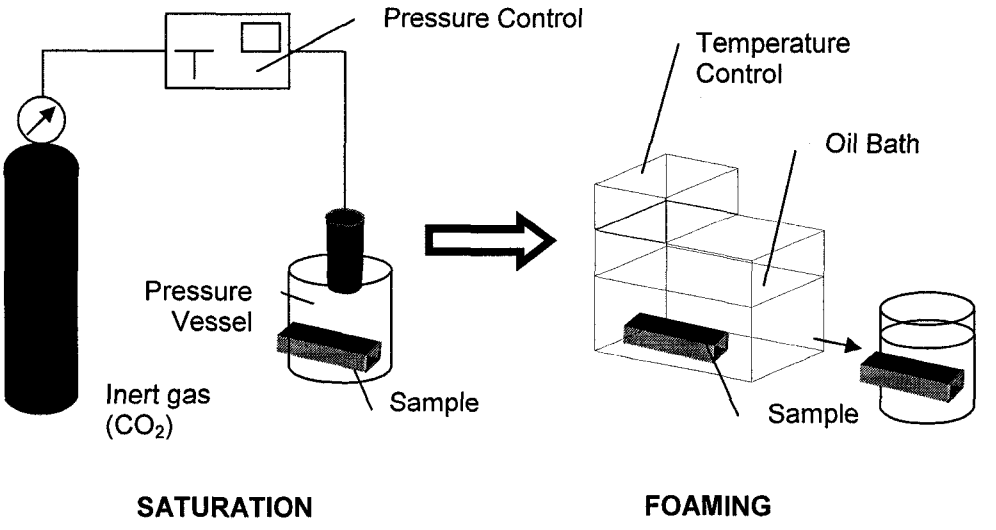

Figure 3.6 Batch processing method.

3.3.4 Mechanical testing

The tensile mechanical properties were tested with an Instron 4202 machine with a 10 kN load cell at room temperature. Rectangular strip samples with thicknesses from 1.5 mm to 3 mm, depending on their expansion ratios, were used for tensile testing. A crosshead speed of 1.0 mm/min was used and the strain was calculated from the displacement of the crosshead of the machine. The elastic moduli were obtained by calculating the slope of the stress-strain curves at the initial linear portions. The experimental results of tensile strength and elongation at break were also reported. A minimum of five specimens were tested for each sample and the average data were used in this study.

3.4 Results and Discussion

3.4.1 Mechanical properties of PMMA microcellular foams

Mechanical behavior of PMMA microcellular foams were determined by tensile experiments. Different densities of the PMMA foams were obtained by changing the processing parameters such as foaming time, foaming temperature and saturation pressure. The engineering stress-strain curves of the PMMA microcellular foams are presented in Fig. 3.7 at different relative densities (ρ_r). As shown in the figure, the tensile mechanical properties of the PMMA microcellular foams were closely related to the foam density, which is controlled by the foaming conditions. The elastic modulus, tensile strength and the elongation at break were studied as functions of foam relative density. The experimental correlation between the modulus and the relative density matched Gibson's equation on the whole. The tensile strength and elongation at break both decreased when decreasing foam density. For some of the foaming conditions which resulted in higher foam density, higher elongation at break of the microcellular PMMA foam was observed compared with the unfoamed PMMA [Fu et al. 2005].

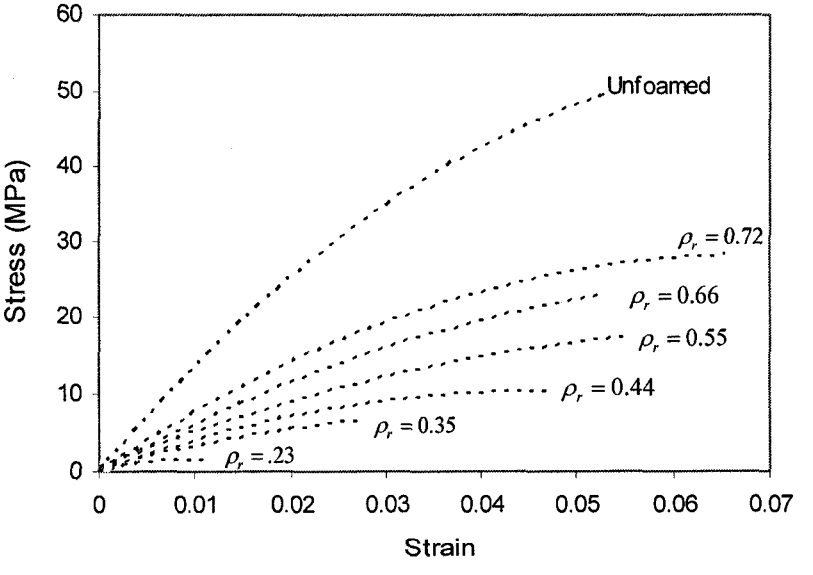

Figure 3.7 Experimental tensile behavior of PMMA microcellular foams.

3.4.2 Parametric verification of the constitutive equation

The constitutive equation obtained from the Maxwell model was used for validation with experimental results. The elastic modulus of foams E^* under the tensile loading can be represented in terms of the relative density of foams using Gibson and Ashby's prediction [Gibson and Ashby 1999] for closed cell foams;

$$\frac{E^*}{E_s} \approx \phi^2 \rho_r^{\,2} + (1-\phi)\rho_r \tag{3.30}$$

where E_s is Young's modulus of the unfoamed solid and ρ_r is the relative density of foams and ϕ is the fraction of solid in the cell struts. Using Eq. (3.30), Eq. (3.6) is expressed as a function of the relative density of foams;

$$\sigma = \tau\dot{\varepsilon}E_s\left[\phi^2\rho_r^{\,2} + (1-\phi)\rho_r\right]\left[1-\exp\left(-\frac{\varepsilon}{\tau\dot{\varepsilon}}\right)\right] \tag{3.31}$$

This constitutive equation can be applied for nonlinear elastic tensile behavior of foams. The parametric studies to Eq. (3.31) are shown in Fig. 3.8. As expected, the stresses increased with increasing strain rate, elastic modulus, time constant, and relative density, though this stress decreases as ϕ increases, which implies that the cells are approached to open-celled form.

3.4.3 Validation of the constitutive equation for PMMA microcellular foams

In Fig. 3.8, the stress-strain curves plotted by Eq. (3.31) were compared with uniaxial tensile test data. It was demonstrated that theoretical curves closely represent the experimental data. Chen's experiments [Chen et al. 2002] have yielded behavior on quasi-static tensile tests of PMMA, however there was little yield phenomenon observed in the current experiment as shown in Fig. 3.9. The macroscopic responses of the PMMA foams appeared quite brittle. The tensile strengths of the analytical curves in Fig. 3.9(a) were calculated by the formula proposed for PMMA microcellular foams [Fu et al. 2005]:

$$\frac{\sigma_{TS}^*}{\sigma_{TS}} \approx \rho_r^{\,2} \tag{3.32}$$

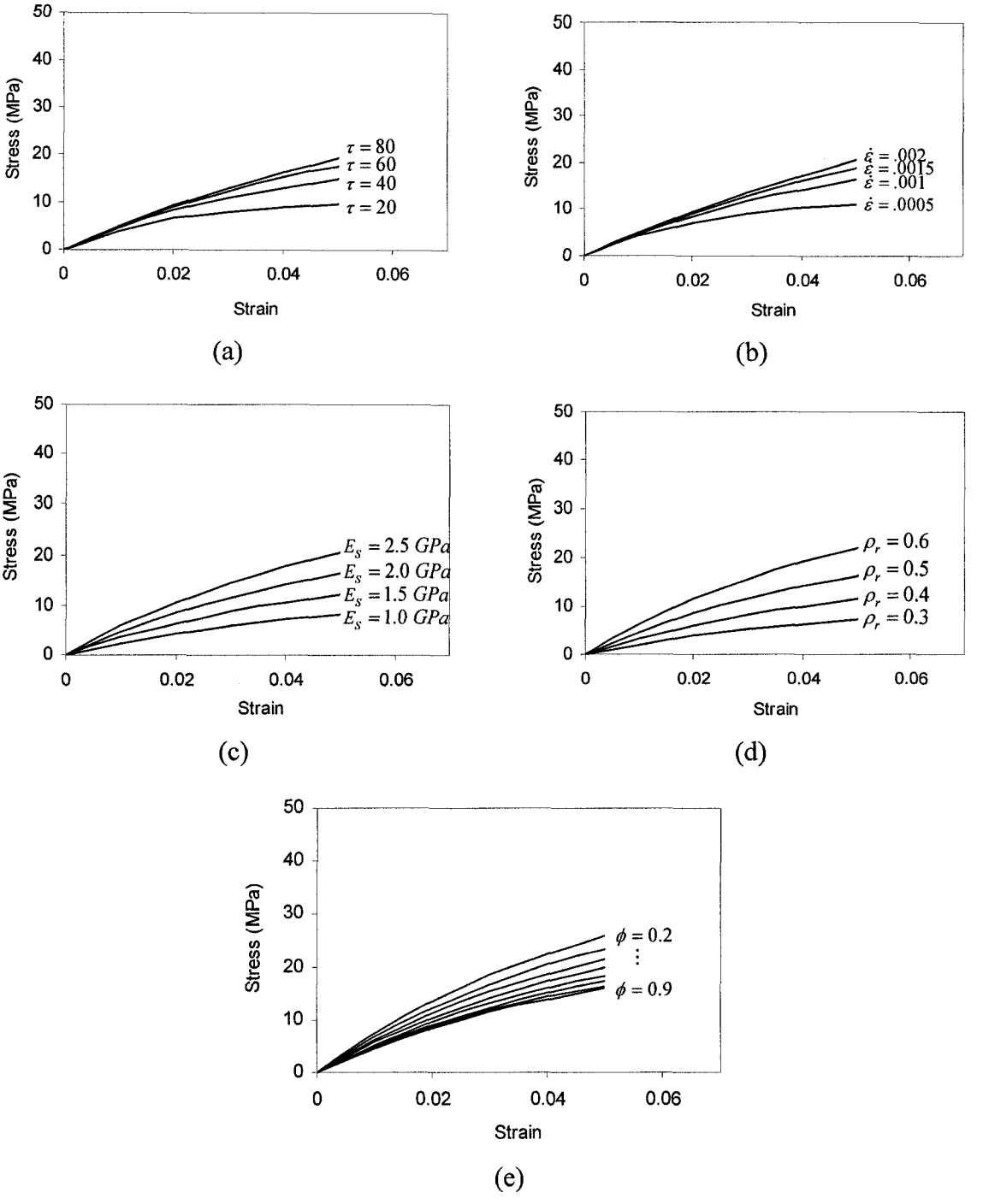

Figure 3.8 Parametric verification of the constitutive equation (a) relaxation time constant, (b) strain rate, (c) elastic modulus, (d) relative density of foams, and (e) fraction of solid in the cell struts.

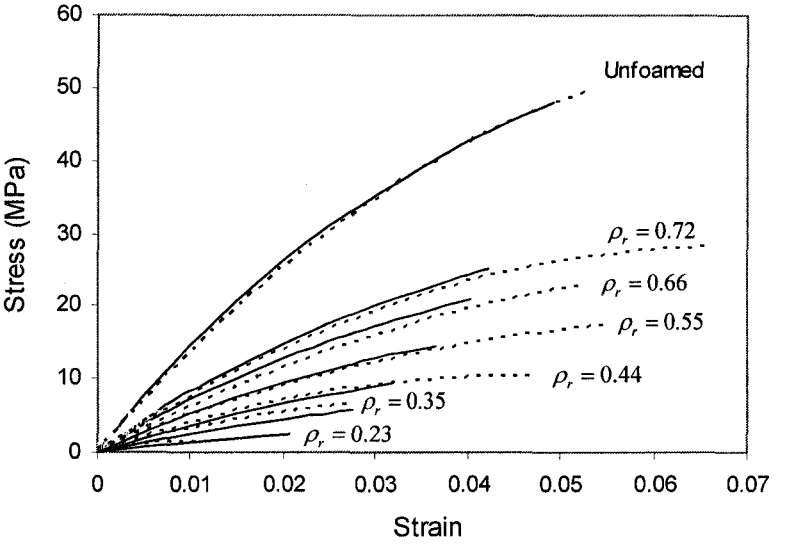

(a)

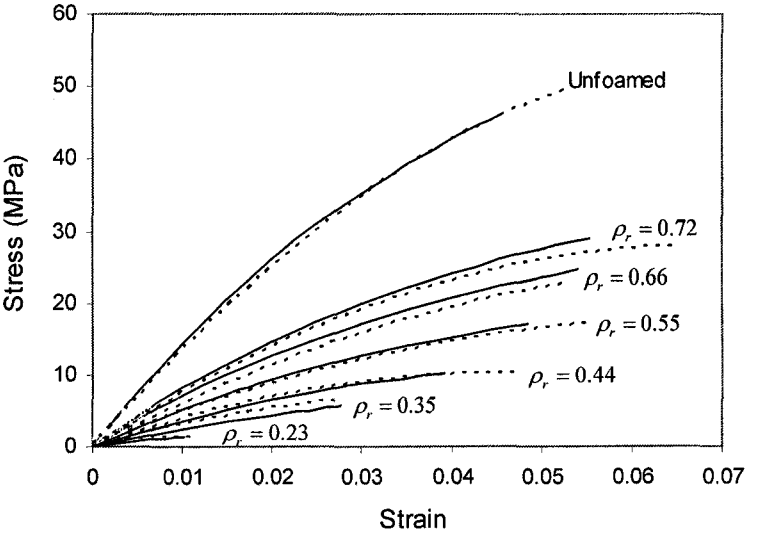

(b)

Figure 3.9 Comparison of the engineering tensile stress-strain curves of PMMA foams (solid lines: Eq. (3.31), dotted lines: experimental results): (a) Tensile strength was used for break point in Eq. (3.31); (b) Failure strain was used for break point in Eq. (3.31).

where σ_{TS}^{*} and σ_{TS} are the tensile strengths of the foam and unfoamed solid, respectively. For the value of ϕ, 0.8 was chosen in Eq. (3.31) because the magnitude of the elastic modulus of foams, E^{*}, (Eq. (3.30)) was close to the experimental data when $\phi = 0.8$. If the percent elongation is used for the determination of the failure strain, the stress-strain curves from Eq. (3.31) fit the experimental data more closely as shown in Fig. 3.9(b).

The same strain rate (= 0.000667 s^{-1}) was applied to both Eq. (3.31) and experimental results, and the relaxation time constant $\tau = 65$ was used for plotting of Eq. (3.31) in Fig. 3.9. Also the Young's modulus of unfoamed PMMA E_s =1940 was used in Eq. (3.31). The time constant $\tau = 65$ is valid only at the strain rate used in this experiments. Therefore, if the test condition is changed, τ would be changed too.

In this study, only one relaxation time constant was used for comparison with experimental results, however, the rate of the change of the time constant τ to the change of the strain rate or time should be defined with more experimental data. Therefore, for generalized expression of the constitutive equation, the time constant τ should be represented in terms of test conditions or foam properties, such as strain rate, and requires the effect of varying strain rate during loading to be taken into account. Also, the effects of cell morphology such as cell size, cell distribution, cell type and cell wall thickness are recommended to be considered in formulating the constitutive equations.

3.5 Conclusion

Constitutive equations for PMMA foams subjected to tensile loading were studied, where viscoelastic components were used to model the nonlinear tensile behavior of foams. Results indicated that the constitutive equation obtained from the Maxwell model could be representative of all the constitutive equations based on different types of viscoelastic models such as: the Generalized Maxwell model, the Three Element model and the Burgers model. In other words, any stress-strain curve made by the Generalized Maxwell model, Three Element model and Burgers model could also be generated by the constitutive equation using the Maxwell model provided the relaxation time constant is chosen properly.

The proposed constitutive equations are expressed as functions of strain, strain rate, relaxation time constant and elastic modulus, where foam properties such as equivalent elastic modulus, fraction of solid in the cell struts, and relative density of foams are used. With these parameters, the constitutive model could describe the nonlinear elastic tensile behavior of foams. Without considering the temperature effect, this constitutive model has an advantage in that it can be applied to practice with only a few foam properties. For verification of the constitutive model, microcellular foams were prepared from PMMA using the batch method and tensile test results of the foams were compared with the model. The theoretical model demonstrates a fit quite similar to test data.

Chapter 4

Tensile Behavior of Intercalated Polymer/Clay Nanocomposite Foams[1]

4.1 Introduction

The effect of nanoparticles on the elastic modulus of the polymer/clay nanocomposites has been studied experimentally [Luo and Daniel 2003, Cho and Paul 2001, Lee and Goettler 2004, Vu el al. 2004, Murphy et al. 2003, Kuo et al. 2005]. It has been generally seen that the Young's modulus of the nanocomposites increases with increasing nanoparticle contents; however, the decreasing elastic modulus under tensile behavior is sometimes seen when high loadings of nanoparticles are used [Xie et al. 2004, Pappas et al. 2005].

At high clay loadings, the intercalated clays have a role to improve the mechanical properties of the materials and at the same time, some of the intercalated clays may have aggregate-like form. Therefore, a further increase of clay particles may be detrimental to the mechanical properties. For phenolic resin/montmorillonite (MMT) clay nanocomposites, the tensile modulus was observed to be decreased after optimal concentration of clays [Pappas et al. 2005]. Miyagawa [Miyagawa et al. 2005] showed there was an upper limit on the improvement of the modulus by clay loading and it was possible that the existence of the intercalated clay nanoplatelets may result in the lower tensile strength. Using the intercalated nanocomposites, Zerda [Zerda and Lesser 2001] showed that as the clay concentration increases the size of clay particles increases and interparticle distances decreases.

For evaluation of the reinforcing effect of clay nanoplatelets on the modulus of clay nanocomposites, Tandon–Weng and Halpin–Tsai equations may be used [Tandon and Weng 1986, Halpin and Kardos 1976]; however, they are well applied for completely exfoliated

[1]Reproduced from: C. Jo, J. Fu and H.E. Naguib, Constitutive modeling for intercalated PMMA/clay nanocomposite foams, Polym. Eng. Sci., 2006, 46(12): 1787-1796.

structure. For the existence of the intercalated clay nanoplatelets, Brune [Brune 2002] applied a pseudo-inclusion concept with the Halpin–Tsai equation for the evaluation of the effect of stacked clay particles on the elastic modulus, where clay stacks were proved to have a detrimental effect on the reinforcement efficiency. A study for the case of an infinitely extended homogeneous elastic solid containing an ellipsoidal inclusion was performed by Eshelby [Eshelby 1957]. At higher clay loading, a substantial amount of the clay remains in aggregate or intercalated form. The clay in intercalated form improves mechanical properties, but intercalated clay retains some of its aggregate-like properties, so a further increase in the mass fraction of clay could be detrimental. Tsukrov [Tsukrov 2000] derived the effective elastic moduli of 2-D solids with randomly located perfectly rigid elliptical inclusions.

In this chapter, an elastic modulus of polymer/clay nanocomposite foams that can accommodate the reinforcing effect by intercalated clays and the detrimental effect by agglomerated clays is studied. Then, the modulus is applied for the constitutive equation for tensile behavior of polymer/clay nanocomposite foams. PMMA/clay nanocomposite foams are manufactured by batch process method and their uniaxial tensile test results are compared with those by the constitutive model. The PMMA/MMT nanocomposites may possess exfoliated and intercalated structures [Li et al. 2003, Okamoto et al. 2001, Huang and Brittain 2001]; however, exfoliation was not considered in this study since fully exfoliated structure is not manufactured easily.

4.2 Constitutive Modeling

4.2.1 Elastic modulus of nanocomposites containing intercalated clays

The elastic modulus of the nanocomposites can be expressed by using the Mori Tanaka method [Mori and Tanaka 1973] and Benveniste's expression [Benveniste 1987] as

$$E_c = E_m + v_p\left\{\left(E_p - E_m\right)T\right\}\left[v_m + v_p\{T\}\right]^{-1} \quad , \tag{4.1}$$

where E_m and E_p are elastic moduli of polymer matrix and clay particulates, respectively, and v_p and v_m are volume fractions of clay particles and polymer matrix, respectively. The

bracket { } in Eq. (4.1) denotes average over all possible orientations. The component $T\left[v_m + v_p\{T\}\right]^{-1}$, called concentration factor, represents the ratio of the average strain in a typical individual inclusion and the homogeneous constant strain. By using Eshelby's [Eshelby 1957] result, Benveniste [Benveniste 1987] derived an expression for T as

$$T = \left[1 + SE_m^{-1}(E_p - E_m)\right]^{-1} . \tag{4.2}$$

where S denotes Eshelby's tensor. When the intercalated clay regions are assumed as penny-shape the Eshelby's tensors are expressed as [Nemat-Nasser and Hori 1993]

$$S_{1111} = S_{2222} = \frac{\pi(13-8\nu)}{32(1-\nu)}\frac{a_3}{a_1} \text{ and } S_{3333} = 1 - \frac{\pi(1-2\nu)}{4(1-\nu)}\frac{a_3}{a_1} \qquad (a_1 = a_2 \gg a_3), \tag{4.3}$$

in which ν is the Poisson's ratio of the polymer matrix and a_3/a_1 is the aspect ratio of the penny-shape. If an average value of the three orthogonal components can be used for randomly oriented case, S is expressed by

$$S = \frac{1}{3}S_{iiii} = \left(\frac{1}{3} + \frac{3\pi}{16(1-\nu)}\right)\frac{a_3}{a_1} , \tag{4.4}$$

S is a function of the aspect ratio of clay cluster and Poisson's ratio. When clay particles are assumed randomly oriented in the polymer matrix, the orientation effect of the inclusions is neglected during the deformation, thus, Eq. (4.1) becomes

$$E_c = E_m + v_p\left(E_p - E_m\right)T\left(v_m + v_p T\right)^{-1} . \tag{4.5}$$

In this study, the clays in polymer matrix are assumed to be embedded as intercalated and agglomerated states in nanocomposites. Then, the volume fraction of clay particles used in Eq. (4.5) is divided by intercalated and agglomerated components,

$$v_p = f_i v_p + f_a v_p = v_{pi} + v_{pa} , \tag{4.6}$$

where f_i and f_a are the intercalated and agglomerated fractions of clays, respectively. v_{pi} is the volume fraction of the clay particles which will be intercalated and v_{pa} is the volume fraction of agglomerated clay particles. The interactions among the clay clusters can be neglected since the volume fraction of the clay particles was assumed to be small. When intercalation process has finished, the volume fraction of the intercalated region becomes greater than v_{pi} because matrix material has been inserted between the clay layers. Hence,

modified intercalated volume fraction was used for the calculation of the modulus of the nanocomposites. If the clays are disk shaped and have uniform size in the whole intercalated regions, the modified volume fraction of the intercalated regions is calculated as

$$\begin{aligned} v_{pi}' &= N_i\left[n_c d_c + (n_c - 1)d_m\right]A_c\frac{1}{V} \\ &= N_i n_c d_c\left(1 + \frac{n_c - 1}{n_c}\frac{d_m}{d_c}\right)A_c\frac{1}{V} \\ &= v_{pi}\left(1 + \frac{n_c - 1}{n_c}\frac{d_m}{d_c}\right) \\ &= f_i v_p\left(1 + \frac{n_c - 1}{n_c}\frac{d_m}{d_c}\right), \end{aligned} \tag{4.7}$$

in which, N_i is the number of intercalated clay clusters in the matrix and n_c is the number of clay layers in each intercalated clay cluster. d_c and d_m denote the clay layer thickness and the layer spacing between clay particles, respectively. Also, A_c is the area of the clay particle and V is the total volume of composites. Then, the new volume fractions are defined as

$$1 = v_m' + v_{pi}' + v_{pa}\ , \tag{4.8}$$

where $v_m' = (1 - v_p) - f_i v_p \frac{n_c - 1}{n_c}\frac{d_m}{d_c}$ is the volume fraction of the matrix after intercalation process has finished. Therefore, the modulus of the composites in Eq. (4.5) is modified to the following form

$$E_c = E_m + v_{pi}'T\left(v_m' + v_{pi}'T\right)^{-1}\left(E_p - E_m\right)\ . \tag{4.9}$$

In Eq. (4.9), the modulus of the intercalated region was regarded to have the same modulus as the clay clusters. The macromolecular chains intercalated in clay layers are confined in a very small space and their behavior is quite different from those in bulk matrix, which results in the macromolecules becoming rigid. Also, the increasing effect of the tensile modulus by considering the interfacial region between the polymer matrix and clay particles was proved by Ji [Ji et al. 2002]. Thus, the elastic modulus in the intercalated region is usually assumed as the same to that of the clay particles. The orientation effect of the clay

particles was assumed small and neglected in Eq. (4.9) because the clay particles were assumed randomly oriented.

4.2.2 Elastic modulus of nanocomposites containing agglomerated clays

During tensile mode, some intercalated nanocomposites show decreasing elastic modulus with increasing clay contents [Xie et al. 2004, Pappas et al. 2005]. The decreasing phenomenon of the elastic modulus of the nanocomposites containing agglomerated clays can be explained by increased overall elastic strain due to matrix failure at agglomerated clay regions. This implies that the bonding forces between the matrix and the agglomerated clays become weak and consequently, the agglomerated clays play as a cavity or crack in the matrix. Thus, the overall elastic modulus of the nanocomposites with inclusions was calculated with the assumption that the agglomerated clays can be considered as cracks which exist in the matrix. Also, many cracks in the matrix are accounted for the dilute distribution, in which cracks are so far apart that their interactions may be neglected. The validity of this method is limited to the case of the composites that have relatively small volume fraction of inclusions. In this section, the elastic modulus of an isotropic material that contains aligned penny-shaped cracks was estimated.

The notion of a representative volume element (RVE) is used to estimate the continuum properties of the heterogeneous medium in terms of the properties and structures of the microconstituents [Nemat-Nasser and Hori 1993, Drugan and Willis 1996, Wang and Huang 1995]. Using the concept of RVE the overall strain increment of the nanocomposites containing cracks can be estimated as a function of the prescribed local incremental values. Within the volume V of RVE, strain-displacement relation is expressed at a typical point x by

$$\varepsilon = \frac{1}{2}\left\{\nabla \otimes \mathbf{u} + (\nabla \otimes \mathbf{u})^{T}\right\} \quad \text{in V}, \qquad \mathbf{u} = \mathbf{u}(\mathbf{x}). \tag{4.10}$$

The volume average of $\boldsymbol{\varepsilon}$ is

$$\overline{\varepsilon} \equiv \frac{1}{V}\int_{V} \varepsilon \, dV \, . \tag{4.11}$$

If the displacements are assumed prescribed on the boundary of the RVE, the average strain $\bar{\varepsilon}^{o}$ is given in terms of the boundary displacements u^{o} by

$$\bar{\varepsilon}^{o} = \frac{1}{V}\int_{\partial V}\frac{1}{2}\left(v \otimes u^{o} + u^{o} \otimes v\right) dS \,, \tag{4.12}$$

where v is the outer unit normal vector of the bounded surface ∂V. With the RVE concept, the overall elastic parameters of solids containing cracks can be established. If inclusions are considered as cavities, the average strain is expressed by two components

$$\bar{\varepsilon} = \bar{\varepsilon}^{o} + \bar{\varepsilon}^{c} \,, \tag{4.13}$$

where $\bar{\varepsilon}^{o}$ is the average strain of the RVE having no cavities and $\bar{\varepsilon}^{c}$ is the additional strain due to the presence of the cavities.

The magnitude of $\bar{\varepsilon}^{c}$ can be obtained by introducing the virtual stress and strain on the cavity surfaces and by using reciprocal theorem between virtual loading and actual loading [Nemat-Nasser and Hori 1993]

$$\bar{\varepsilon}^{c} = \frac{1}{V}\int_{\partial\Omega}\frac{1}{2}\left(n \otimes u + u \otimes n\right) dS \,, \tag{4.14}$$

where $\partial\Omega$ denotes cavity surface and n is the exterior unit normal vector on the cavity surface and u is the displacement vector resulting from actual loading. For the calculation of $\bar{\varepsilon}^{c}$, the direction of the penny-shaped cracks that can contribute to the change of the elastic modulus was assumed normal to the tensile load. Let RVE have various crack sizes and total N cracks per unit volume,

$$N = \sum_{\alpha=1}^{n} N_{\alpha} \,, \tag{4.15}$$

where N_{α} is the number of cracks of radius a_{α} per unit volume of RVE. Since cracks in the RVE are considered as dilute distribution,

$$\begin{aligned} \bar{\varepsilon}^{c} &= \sum_{\alpha=1}^{n} N_{\alpha}\frac{1}{V}\int_{\partial\Omega_{\alpha}}\frac{1}{2}\left(n \otimes u + u \otimes n\right) dS \\ &= \sum_{\alpha=1}^{n} N_{\alpha}\bar{\varepsilon}^{\alpha} \,, \end{aligned} \tag{4.16}$$

where $\bar{\varepsilon}^{\alpha}$ denotes the overall strain due to a crack a_{α} and defined as

$$\bar{\varepsilon}^{\alpha} \equiv \frac{1}{V}\int_{\partial\Omega_{\alpha}}\frac{1}{2}\left(n \otimes u + u \otimes n\right) dS \,. \tag{4.17}$$

The magnitude of u in Eq. (4.17) can be considered as crack opening displacement in mode I crack. The displacement of the penny-shaped crack edge can be obtained from elastic crack-tip field theory. For plane strain case, the displacement in the direction of tensile loading is calculated by using Airy stress function and Westergaard function [Broek 1986] as

$$u = \frac{1+\nu}{E}\left[2(1-\nu)\,\mathrm{Im}\,\bar{Z} - n\,\mathrm{Re}\,Z\right] . \tag{4.18}$$

In Eq. 18, the complex function $Z(z)$ is defined as

$$Z(z) = \mathrm{Re}\,Z + i\,\mathrm{Im}\,Z \text{ and } \frac{d\bar{Z}}{dz} = Z \quad (z = x + iy) . \tag{4.19}$$

When the origin of the coordinate system is located at the crack tip, the analytic function Z which satisfies the boundary conditions at crack tip is given by

$$Z_{|z|\to 0} = \frac{K_I}{\sqrt{2\pi z}} \qquad \text{with } z = re^{i\theta} . \tag{4.20}$$

Then, using the expression for Z in Eq. (4.20), the displacement u at crack surface ($\theta = \pi$) is obtained as

$$u = 4(1-\nu^2)\frac{K_I}{E}\sqrt{\frac{r}{2\pi}} . \tag{4.21}$$

When a penny-shaped crack embedded in an infinite elastic medium is subjected to uniform tension, one of the stress components at a general point in the interior of the elastic solid has the following form [Sneddon 1946],

$$\sigma_z = \frac{2p_0}{\pi}\sqrt{\frac{c}{2\delta}}\left\{\frac{5}{4}\cos\frac{1}{2}\psi - \frac{1}{4}\cos\frac{5}{2}\psi\right\} , \tag{4.22}$$

where δ and ψ are parameters in polar co-ordinates, c is the half crack length, and p_0 is the applied stress. When Eq. (4.22) is compared with the crack tip stress component of mode I crack

$$\sigma_{ij} = \frac{K_I}{\sqrt{2\pi r}} f_{ij}(\theta) , \tag{4.23}$$

K_I in Eq. 23 has the form

$$K_I \approx \frac{2\sigma_0}{\pi}\sqrt{a\pi} . \tag{4.24}$$

If the origin of the coordinate for the displacement v is moved to the center of the crack, the parameter r in Eq. (4.21) is changed to $a-r$. Then, Eq. (4.21) yields the displacement of the penny-shaped crack edge under crack opening mode after substitution of K_I in Eq. (4.24),

$$u = \frac{\sigma_0}{E}\frac{8(1-\nu^2)}{\sqrt{2\pi}}\sqrt{a^2 - ar} \ . \tag{4.25}$$

The direction of the displacement u is parallel to the load direction and normal to the crack surface. For a crack Ω_α of radius a_α, the overall strain increment parallel to σ_0 is calculated from Eqs. (4.17) and (4.25) as

$$\bar{\varepsilon}^{\alpha} = \frac{1}{V}a^3\frac{32\sqrt{2}(1-\nu^2)}{15E}\sigma_0 \ . \tag{4.26}$$

For simplicity, if all crack sizes in RVE are uniform as a_α and all N_α are the same, Eq. (4.16) becomes, by dilute distribution,

$$\bar{\varepsilon}^{c} = nN_\alpha\bar{\varepsilon}^{\alpha} = N\bar{\varepsilon}^{\alpha} \ . \tag{4.27}$$

Substitute Eq. (4.26) into Eq. (4.27), to arrive at

$$\bar{\varepsilon}^{c} = \frac{Na^3}{V}\frac{32\sqrt{2}(1-\nu^2)}{15E}\sigma_0 \ . \tag{4.28}$$

Since the compliance part of Eq. (4.28) contains elastic modulus E, the average strains in Eq. (4.13) can be expressed by using compliance tensors and from which the expression for the overall elastic modulus of RVE is obtained. Representing $\bar{\varepsilon}$ and $\bar{\varepsilon}^{o}$ in terms of compliances,

$$\bar{\varepsilon} = \bar{D}:\sigma^{o} \text{ and } \bar{\varepsilon}^{o} = D:\sigma^{o} \ , \tag{4.29}$$

where $\bar{D}$ is overall compliance and σ^{o} is average macro stress and D is the elastic compliance tensor for the matrix. Then, the average strain in Eq. (4.13) can be modified as a compliance form,

$$\bar{D} = D + \frac{Na^3}{V}\frac{32\sqrt{2}(1-\nu^2)}{15E} \ . \tag{4.30}$$

Since $\bar{D} = 1/\bar{E}$ and $D = 1/E$, the expression for the overall elastic modulus of RVE is obtained as

$$\bar{E} = E\left[1+\frac{Na^3}{V}\frac{32\sqrt{2}\left(1-\nu^2\right)}{15}\right]^{-1} . \tag{4.31}$$

The modulus $\bar{E}$ decreases as crack radius and number of cracks increase. The aspect ratio of agglomerated clay clusters is relatively low compared to intercalated clays [Li et al. 2003, Priya and Jog 2003]. Thus, if the penny-shaped crack is regarded as a disk shape with radius a and when the aspect ratio of the disk is lower than ten, the volume of the disk becomes close to a^3. Then, Na^3/V in Eq. (4.31) can be considered as a volume fraction of the agglomerated clay particles. Therefore, by using the relationship

$$\frac{Na^3}{V} \equiv f_a v_p , \tag{4.32}$$

the modulus $\bar{E}$ in Eq. (4.31) can also be expressed as

$$\bar{E} = E\left[1+f_a v_p \frac{32\sqrt{2}\left(1-\nu^2\right)}{15}\right]^{-1} . \tag{4.33}$$

In this constitutive model, the effect of the agglomerated clay size was not considered for simplicity. Thus, for overall modulus of nanocomposites, Eq. (4.33) was used in this study. In case of PMMA/clay composites, average crystallite thickness and average number of clay layers per aggregate may increase with clay contents [Tabtiang 2000]; however, in this study, the initially determined volume fraction of the aggregated clay particles were used in the constitutive model.

4.2.3 Constitutive equation for polymer/clay nanocomposite foams

When the modulus of the nanocomposites containing agglomerated clays (Eq. (4.33)) is applied to the polymer matrix containing intercalated clay particles, the overall modulus ($\bar{E}_c$) for nanocomposites containing both intercalated and agglomerated clay particles is yielded from Eqs. (4.9) and (4.33) as

$$\bar{E}_c = \left[E_m + v_{pi}'T\left(v_m' + v_{pi}'T\right)^{-1}\left(E_p - E_m\right)\right]\left[1+f_a v_p \frac{32\sqrt{2}\left(1-\nu^2\right)}{15}\right]^{-1} . \tag{4.34}$$

In the previous work [Jo et al. 2005], a constitutive model using an equivalent elastic modulus was proposed for nonlinear elastic behavior of polymeric materials. If the equivalent elastic modulus of the nanocomposite containing the effect of the nanoparticles is determined, it can be applied for the constitutive equation of the nanocomposite materials. For tensile behavior of PMMA/clay nanocomposites, the constitutive equation based on the viscoelastic behavior was adapted since the constitutive model has well described the elastic behavior of PMMA [Jo et al. 2005]. Therefore, the constitutive equation for PMMA/clay nanocomposites can be expressed using the overall modulus $\bar{E}_c$ obtained in the previous section,

$$\sigma = \bar{E}_c \tau \dot{\varepsilon} \left[1 - \exp\left(-\frac{\varepsilon}{\tau \dot{\varepsilon}} \right) \right], \tag{4.35}$$

where τ is a time constant determined by experiments. In order to apply the constitutive equation (Eq. (4.35)) for foams, the effect of foam density on the modulus should be specified. In case of the closed cell foams, the elastic modulus of the nanocomposite foams ($\bar{E}_c^*$) can be represented as a function of the relative density of foams by using the Gibson's prediction [Gibson and Ashby 1999] as

$$\bar{E}_c^* = \bar{E}_c \left[\phi^2 \rho_r^2 + (1-\phi) \rho_r \right], \tag{4.36}$$

where ρ_r is the relative density of foams and ϕ is the volume fraction of solid contained in the cell edges. The value of ϕ is determined by experiments. Therefore, by using $\bar{E}_c^*$ in place of $\bar{E}_c$ in Eq. (4.35), the constitutive equation for tensile behavior of PMMA/clay nanocomposite foams has been yielded as Eq. (4.37):

$$\sigma = \bar{E}_c^* \tau \dot{\varepsilon} \left[1 - \exp\left(-\frac{\varepsilon}{\tau \dot{\varepsilon}} \right) \right]. \tag{4.37}$$

4.3 Experimental

4.3.1 Materials

Cloisite 20A (C20A), the organically modified montmorillonite clay supplied by Southern Clay Products Inc, was used for the synthesis of polymer/clay nanocomposites. This clay was prepared by an ion exchange reaction involving the inorganic sodium cations of natural montmorillonite and an organic modifier dimethyl dehydrogenated tallow quaternary ammonium. The modifier concentration in the organoclay was reported by the manufacturer to be 95 meq/100 g of clay and has a layer spacing of 24.2 Å. PMMA resin with a M_w=108,500 and a M_n=56,700 was supplied by Canus Plastics. Before use, the PMMA was dried at 90°C for more than 24 h in a vacuum oven., Carbon dioxide (obtained from Praxair) was used as a blowing agent. Methanol and toluene, supplied by Fisher Scientific, were used as reagents.

4.3.2 PMMA/clay nanocomposites

PMMA/clay nanocomposites containing 0.5, 1.0, and 2.0 wt% nanoclay (C20A) loadings were prepared using a solvent co-precipitation method. In this method, dispersions of 0.4 wt% Cloisite 20A in toluene and solutions of 10 wt% PMMA in toluene were prepared. After being stored at room temperature for three days, the organoclay dispersions were sonicated in an ultrasonic bath, model FS140 supplied by Fisher Scientific, for 1 h. The sonicated material was added to the PMMA toluene solution while stirring with a magnetic stirrer for 10 min. The mixtures were then precipitated in methanol/toluene (20:1 volume ratio) with vigorous stirring. The resultant PMMA/clay precipitates were washed two times with methanol/toluene (10:1 volume ratio), and then dried at room temperature for two days and finally kept under vacuum at 90°C for three days [Manninen et al. 2005].

4.3.3 Foaming of PMMA/clay nanocomposites

The foaming experiments were performed in a two stage batch process. In the first stage, the polymer samples were saturated in a subcritical CO_2 bath at a pressure of 5.8 MPa and at room temperature (21-23°C). The saturation time was calculated based on the diffusion coefficient of the carbon dioxide in PMMA nanocomposites [Manninen et al. 2005]. In the second stage, the saturated samples were put in a water bath with a temperature of 60°C. To

control the expansion ratio, different foaming times, varying from 5 to 20 s, were selected. The rapid change in temperature and pressure induced cell nucleation and cell growth. Afterwards, the samples were put in cold water to control the foam morphology.

4.3.4 Mechanical testing

The foamed samples were air dried for 7 days before testing. The foam density was measured by a buoyancy method using a density determination kit supplied by Denver Instrument. The weight of the samples was measured in distilled water and in the air. The Archimedean principle was applied for determining the specific gravity of the foams. The relative foam density is defined as the ratio of foamed to unfoamed sample density and the expansion ratio is obtained as the inverse of the foam density. The tensile mechanical properties were tested with an Instron 4202 machine with a 10 kN load cell at room temperature. Rectangular strip samples with thicknesses from 1.5 mm to 3 mm, depending on their expansion ratios, were used for tensile testing. A crosshead speed of 1.0 mm/min was used and the strain was calculated from the change of the displacement of the crosshead. The Young's moduli were obtained by calculating the slope of the stress-strain curves at the initial linear portions. The experimental results of tensile strength and elongation at break were also obtained, in which at least five specimens were tested for each data point and the averages were used.

4.4 Results and Discussion

It was observed from the experimental results (see Fig. 4.1) that the tensile elastic modulus (Young's modulus) of the PMMA/clay nanocomposites has been increased at 0.5 wt% clay loadings and after 0.5 wt%, the modulus began to decrease with increasing clay loadings. It can be inferred from this trend that up to 0.5 wt% clay loadings, almost all clay particles were used for intercalation in the polymer matrix and as a result, the Young's modulus of the material increased. But when more than 0.5 wt% clay loadings are used, some clay particles are agglomerated leading to decrease of the modulus. PMMA/clay nanocomposites manufactured using organically modified smectite clay showed intercalated

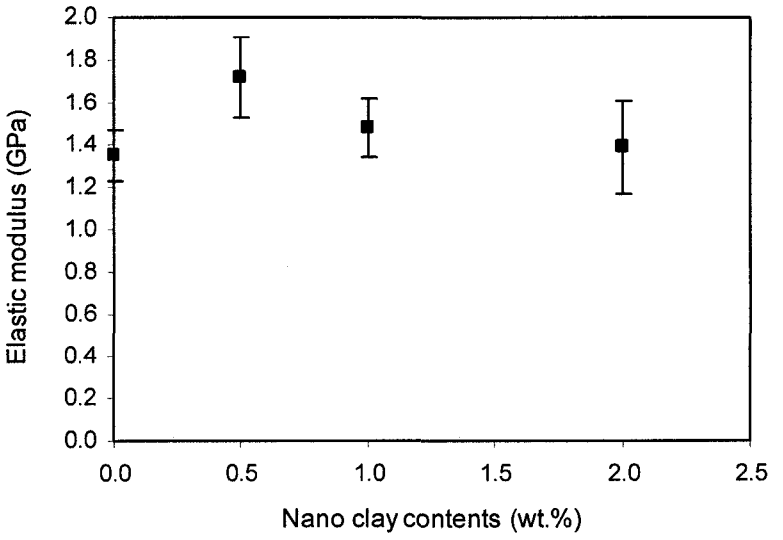

Figure 4.1 Tensile elastic modulus of PMMA/clay nanocomposites containing 0 wt%, 0.5 wt%, 1.0 wt%, and 2.0 wt% nanoclay loadings.

structures at 2 wt% clay contents [Manninen et al. 2005]; however, in this experiment, agglomeration has appeared to start right after 0.5 wt% clay loadings.

The developed theoretical model for elastic modulus of PMMA/clay nanocomposites was plotted in Fig. 4.2 for parametric study, where $d_m/d_c = 2$ and $a_1/a_3 = 20$ were maintained in Fig. 4.2(a) and 4.2(b), respectively. The fully intercalated model (Eq. (4.9)) shows monotonic increase with clay loadings. Compared with the experimental results, this model shows much higher tensile stresses at high clay loadings because the agglomeration effect was not considered in the model. On the contrary, the model including the intercalation and agglomeration (Eq. (4.34)) shows decreasing phenomenon after maximum value. The starting point of the decrease of the modulus was adapted from the experimental result (see Fig. 4.1). As shown in Fig. 4.2, the increase of the aspect ratio of the intercalated clay clusters gives reinforcing effect on the elastic modulus. Also, the larger expansion of the clay spacing improves the modulus. The increase of the aspect ratio of the clay clusters means that the shape of clays become close to the exfoliated form, accordingly, the modulus

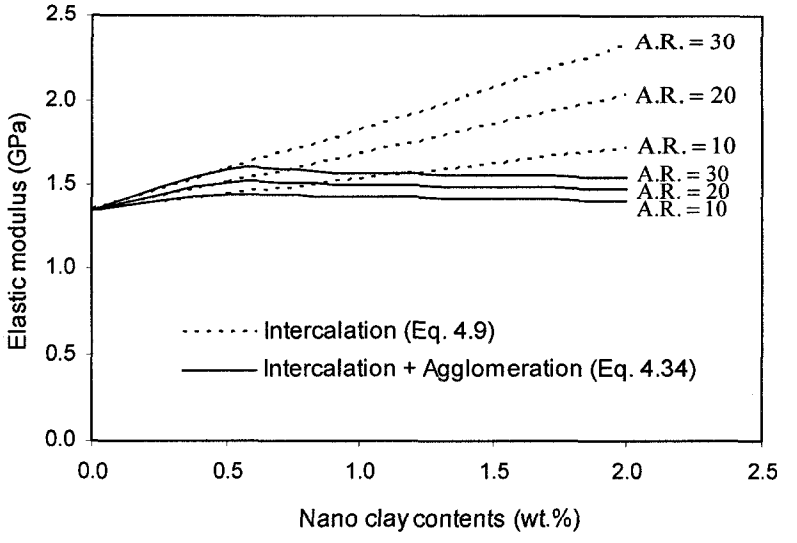

(a)

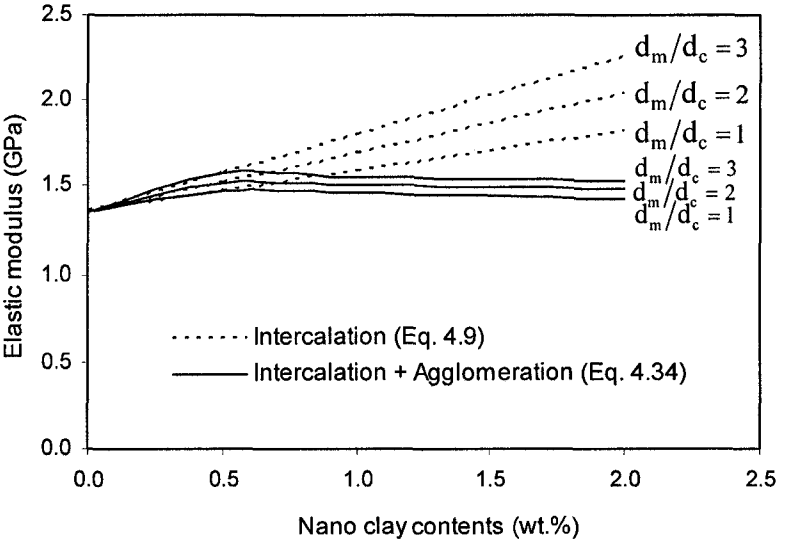

(b)

Figure 4.2 Variation of the elastic modulus by (a) aspect ratio of intercalated clay clusters and (b) expansion of clay layer spacing in the intercalated clay clusters.

Table 4.1 Material parameters used in constitutive model.

ν	a_1/a_3	E_m (GPa)	E_p (GPa)	n_c	d_m/d_c
0.35	20	1.35	170	5	2

will be higher. Also, the increase of the clay layer spacing produces the same effect by increasing the volume fraction of clay. The values of the material parameters used in the theoretical model are listed in Table 4.1. The Young's modulus of PMMA (E_m) was determined by experiment and the Young's modulus of the clay particles (E_p) was obtained from literature [Luo and Daniel 2003, Shia et al. 1998]. The aspect ratio of the clay particles decrease with increasing clay contents [Priya and Jog 2003]; however, the aspect ratio of the intercalated clay clusters (a_1/a_3) was assumed as 20 in the theoretical model. The number of clay layers (n_c) per intercalated clay cluster and the expansion of the clay layer spacing (d_m/d_c) were determined based on the PMMA/MMT composites [Li et al. 2003, Priya and Jog 2003, Winberg et al. 2005].

In Fig. 4.3, the experimental values of the tensile elastic modulus of PMMA/clay nanocomposites were compared with the theoretical predictions (Eq. (4.34)). In the model, $a_1/a_3 = 20$ and $d_m/d_c = 2$ were used. The fraction of the clay particles used for agglomeration was not measured in this experiment, so in the use of the theoretical model, all of the clay particles over 0.5 wt% were assumed to be used for agglomeration. The elastic moduli plotted based on the theoretical model in Fig. 4.3 show similar trend to the experimental results. At 1.0 and 2.0 wt% clay loadings, the moduli by theoretical model represent higher values than experimental results. This difference can be reduced if the volume fraction of the agglomerated clay particles is modified. As the clay loading increases, the intergallery spacing of the clays in polymer nanocomposites is decreased gradually after

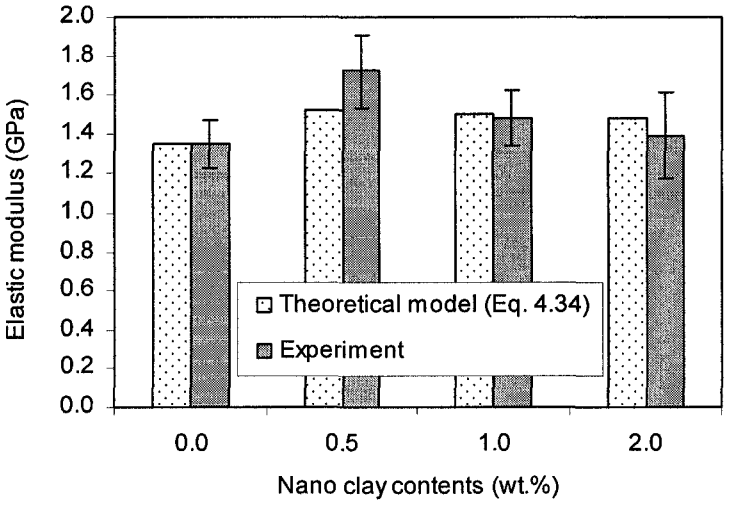

Figure 4.3 Comparison of the tensile elastic modulus of PMMA/clay nanocomposites containing 0, 0.5, 1.0, and 2.0 wt% nanoclay loadings.

having maximum spacing [Priya and Jog 2003, Winberg et al. 2005]. Thus, the volume fraction of the clay particles which contributes to the agglomeration can be larger than just the volume of agglomerated clay particles themselves. After all, the detrimental effect by the agglomerated clay particles could be increased by using the increased volume fraction of the agglomerated clay particles. But, in this study, the initial volume fraction of the agglomerated clay particles v_{pa} was assumed not to be changed during the process for simplicity. Therefore, if modified volume fraction of the agglomerated clays greater than v_{pa} is used in the theoretical model, the predicted moduli would go down at 1.0 and 2.0 wt% of clay loadings in Figure 4.3.

The measured elastic moduli of the PMMA/clay nanocomposite foams are shown in Fig. 4.4 as a function of the relative density of foams and they are compared with the elastic moduli by prediction (Eq. (4.36)). In Eq. (4.36), the parameter ϕ to each clay loading was determined to be able to fit to experimental data. It was observed in Fig. 4.4 that the magnitude of ϕ was increased at higher (2.0 wt%) clay loading. The increase of the parameter ϕ means that the cell walls became weak and consequently, the modulus went

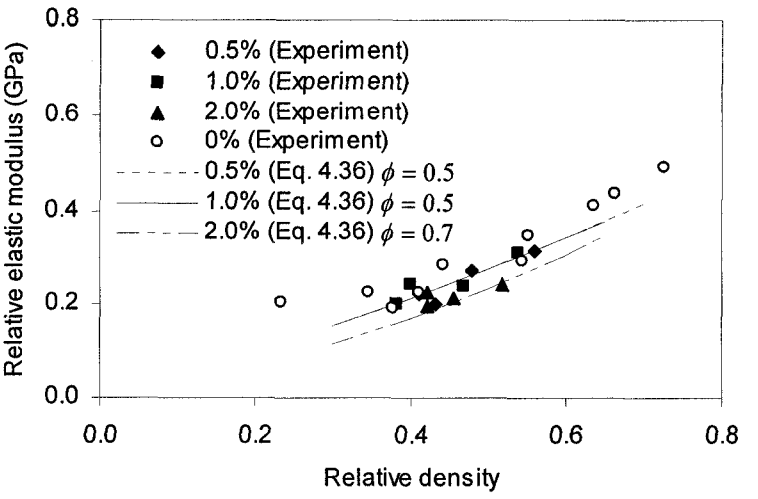

Figure 4.4 Tensile elastic modulus of PMMA/clay nanocomposites foams containing 0.5, 1.0, and 2.0 wt% nanoclay loadings.

down with increasing the clay particles. In other words, agglomeration and the increases of ϕ bring about the similar effect. It was proved from the figure that Eq. (4.36) can be used to predict the elastic modulus of PMMA/clay nanocomposite foams if the foam parameter ϕ is properly determined.

The engineering stress-strain curves of the PMMA/clay nanocomposites are presented in Fig. 4.5(a). At clay loading of 0.5 wt%, the mechanical properties of the PMMA/clay nanocomposites were enhanced in both tensile strength and elongation at break. With increasing the clay loadings, the detrimental effects were clear, especially, the reduction of the elongation at break was remarkable. Some experimental work also show that the tensile modulus of PMMA/clay nanocomposites increases with clay loading, on the other hand, the tensile strength and tensile strain at break may decrease or increase [Park and Jana 2003, Yang and Nelson 2004]. The constitutive equation for PMMA/clay nanocomposites (Eq. (4.35)) was applied and plotted in Fig. 4.5(b) for comparison. In the use of Eq. (4.28), the weight fraction of the clay particles w_p was converted to the volume fraction of the clay particles v_p by

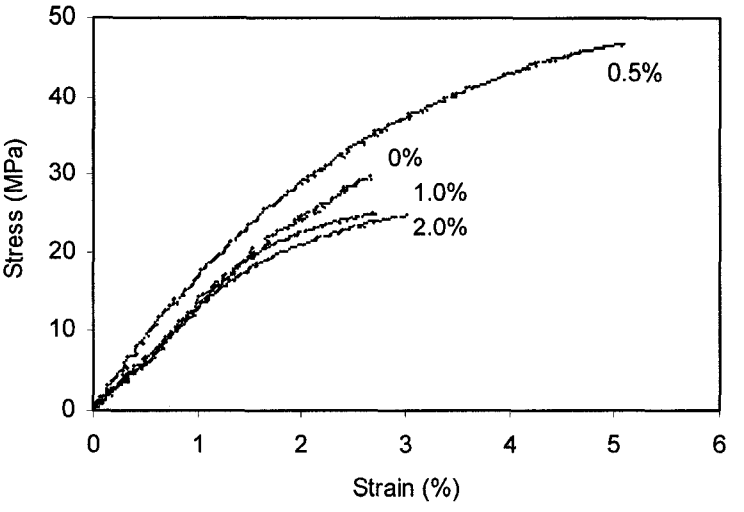

(a)

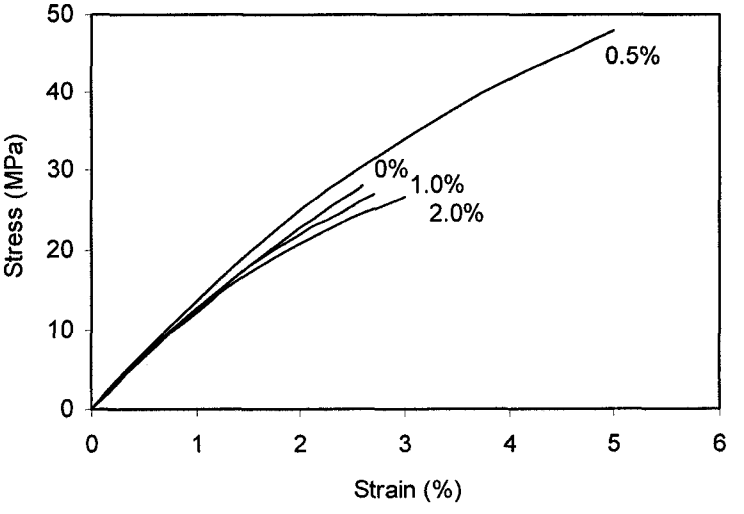

(b)

Figure 4.5 Tensile stress-strain behavior of PMMA/clay nanocomposites containing 0, 0.5, 1.0, and 2.0 wt% nanoclay loadings: (a) experiment; (b) Eq. (4.35).

$$v_p = 1 \Big/ \left[1 + \frac{\rho_p}{\rho_m} \left(\frac{1}{w_p} - 1 \right) \right] . \tag{4.38}$$

Then, the 0.5, 1.0 and 2.0 wt% are converted to 0.331, 0.663 and 1.331 vol%, respectively, where the specific gravities 1.77 for C20A and 1.17 for PMMA were used. The time constant τ is a material property which is determined by experiments [Jo et al. 2005]. For plotting Figure 4.5b, τ = 85, 75, 45 and 40 were used for 0, 0.5, 1.0 and 2.0 wt% of clay composites, respectively. On determination of the failure points in Figure 4.5b, the same percent elongations obtained from test results were used. Since the material parameter τ is changed by materials used, the magnitude of τ for nanocomposites should be changed by different clay compositions. In this experiment, it was proved that the value of τ decreases with increasing the clay loadings.

The constitutive equation for tensile behavior of PMMA/clay nanocomposite foams (Eq. 37) was compared with experimental results in Fig. 4.6. The percent elongations obtained from test results were used for determination of the failure points in Fig. 4.6(b). Also, the same values of τ used for unfoamed case (Fig. 4.5(b)) were used in the constitutive model for foams. Strictly speaking, the τ may be changed at high percentage of clay loadings or in the case of very low density foams. But, in Fig. 4.6(b), τ was considered not to be changed since clay loadings were relatively low and relative foam densities were greater than 0.5. To compare the effect of clay contents on the stress-strain behavior of foams, the foam samples which have the same relative density should be used. In Fig. 4.6(b), the relative densities of foams for the three curves are not exactly same; however, the three curves can be used for comparison of the effect of clay contents because the differences of the relative densities are not big. Compared with the experimental results, the tensile stress-strain curves generated by the proposed constitutive model showed similar stress-strain behaviors.

4.5 Conclusion

A constitutive model for tensile behavior of PMMA/clay nanocomposite foams was developed, elucidating the effect of intercalated and agglomerated nanoclays. In determining the elastic modulus of the nanocomposite foams, the reinforcing effect by intercalated clays

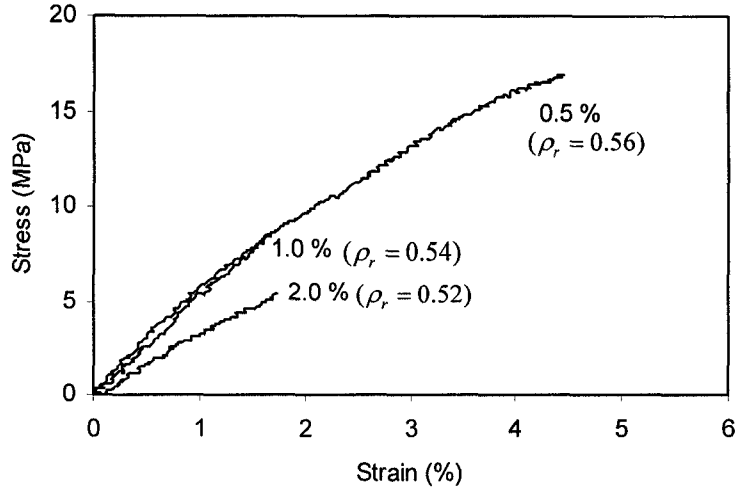

(a)

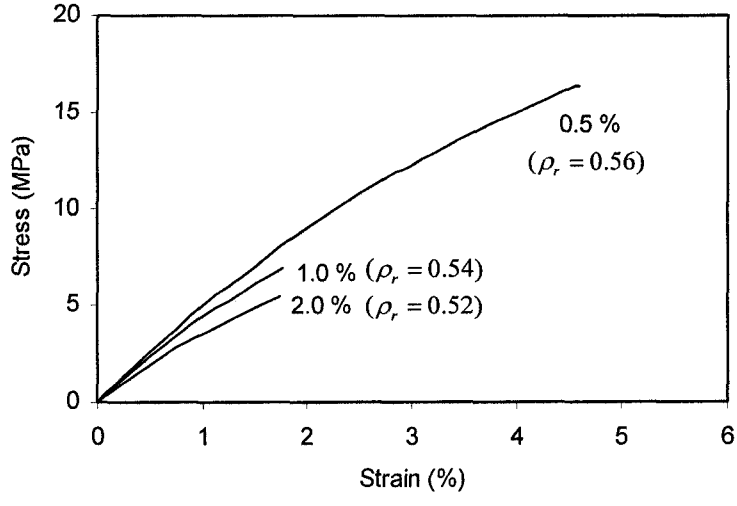

(b)

Figure 4.6 Tensile stress-strain behavior of PMMA/clay nanocomposite foams containing 0.5, 1.0, and 2.0 wt% nanoclay loadings: (a) experiment; (b) Eq. (4.37).

and the detrimental effect by agglomerated clay particles were taken into account. The proposed elastic modulus was expressed in terms of clay morphologies (such as aspect ratio and clay layer spacing) and material properties of the material. PMMA/clay nanocomposite foams containing 0.5, 1.0 and 2.0 wt% nanoclays have been prepared and tensile tests were performed. The mechanical properties such as elastic modulus, tensile strength, and elongation at break were improved at 0.5 wt% clay loading; however, a further increase in the mass fraction of clay was detrimental to the mechanical properties because of the agglomeration of the clays. The tensile stress-strain curves predicted by the constitutive model were in agreement with experimental results. By determining the material parameter τ properly, the proposed constitutive model can predict the tensile behavior of the intercalated and agglomerated PMMA/clay nanocomposite foams.

Chapter 5

Tensile Mechanical Behavior of HDPE/clay Nanocomposite Foams[1]

5.1 Introduction

Generally, the elastic modulus of polymer/clay composites increases with augmenting the clay volume fractions, while the yield stress and strain decrease with increasing clay volume fraction [Osman et. al 2005, Lee J-H et. al 2005]. The enhancing effect of clay in HDPE applies mainly to the modulus rather than the strength [Zhong and Kee 2005]. This enhancing phenomenon is due to the exfoliation of the clays in the matrix, and high aspect ratio of clay particles. The mechanical properties of the nanocomposites are closely related to clay loading and the polymer matrix, as well as to the molecular weight of compatibilizers [Zhong and Kee 2005]. In general, compared to the amorphous polymer, foaming of the semicrystalline polymer is difficult because of the crystalline structures in the semicrystalline polymer, which was demonstrated in references [Doroudiani et al. 1996, Rachtanapun et al. 2003, Lee YH et al. 2005, Doroudiani et al. 1998], where the expansion ratio of foams is decreased with increasing crystallinity. The foaming grade of HDPE is usually decreased with increasing molecular weight or with decreasing melt flow index [Zhang et al. 2003]. Increasing both the molecular weight and amount of blowing agent decreased the cell size. Cell density also increased with increasing HDPE molecular weight [Zhang et al. 2003].

In this chapter, a constitutive model for estimating the tensile behavior of HDPE/clay

[1]Reproduced from:
C. Jo and H.E. Naguib, Constitutive modeling of HDPE polymer/clay nanocomposite foams, Polymer, Polymer, 48(11):3349-3360, 2007.
C. Jo and H.E. Naguib, Effect of nanoclay and foaming conditions on the mechanical properties of HDPE-clay nanocomposite foams, J. Cell. Plast., 43(2):111-121, 2007.

nanocomposite foams was proposed. A model for elastic modulus of HDPE/clay nanocomposite foams was developed by using micromechanics (representative volume element (RVE)) concept. The difference in the modeling of elastic modulus between the current work using HDPE/clay nanocomposite and the previous work [Jo et al. 2006] using PMMA/clay nanocomposite foams is on the type of clay dispersion in the polymer matrix. In the case of PMMA/clay nanocomposite foams, both deteriorating effect by agglomerated clays and enhancing effect by intercalated clays on the elastic modulus were considered. However, in the present work, only intercalated clay model was used because, within the used wt% clay concentration, the overall elastic modulus is not decreased but increases very slowly as clay content increases. Thus, the intercalated clay stacks in HDPE/clay nanocomposites are modeled so that the rate of enhancing effect on the modulus is diminished gradually. In order to describe the tensile elastic behavior of the foams, a viscoelastic model was used. The constitutive model was expressed in terms of microstructural properties of polymer and physical properties of the foams.

Also, the effects of nanoclay and foaming conditions on the foam morphology and mechanical properties of HDPE/clay nanocomposite foams were investigated by experiment. Microcellular HDPE/clay nanocomposites were manufactured using a batch processing using CO_2. Nanoclay loadings of 0.5, 1.0, and 2.0 wt% were used in nanocomposites. Uniaxial tensile tests were performed with the nanocomposites and its foams. Then, the influence of clay loading and foaming conditions on the volume expansion ratio, elastic modulus, tensile strength, and elongation at break were investigated. The tensile experimental data of the foams were compared with the prediction by the theoretical model.

5.2 Constitutive Modeling

5.2.1 Elastic modulus of HDPE/clay nanocomposites

A model for the elastic modulus of HDPE/clay nanocomposite is proposed based on micromechanics. On the modeling the Young's modulus of nanocomposites, the effect of the clay particles on the polymer matrix needs to be investigated first. It was observed that the lamellar thickness and interlamellar spacing of HDPE increase when the crystallization

temperature increases [Schultz 2001]. The crystallization temperature of HDPE/clay nanocomposites was tested by Lee et al. [Lee YH et. al 2005], where the crystallization temperature increased from 117.4 to 118.8°C when clay content varied from 0 to 3 wt%. In this temperature range, changes of interlamellar spacing and lamellar thickness were small, keeping 12 nm and 26 nm, respectively [Schultz 2001]. Thereof, in this study, the thicknesses of crystalline and amorphous layers in the HDPE are assumed not to be changed even though clays are added. At low clay loadings, some clay particles are observed as well-dispersed structures throughout the HDPE matrix [Lee YH et. al 2005]. However, in this study, all clay particles are modeled as intercalated structures for simplicity's sake, and at the same time, variable clay spacing dependent on the clay contents is considered in the model.

The intercalated clay stacks are modeled as cuboids with dimensions a_1 and thickness a_3, with one of the lengths always keeping a right angle to the load direction (Fig. 5.1). When the angle between the clay plane and load direction ($\pi/2-\theta$) varies from 0° to 90°, the reinforcing effect of the clay on the elastic modulus goes from maximum to minimum. If each intercalated clay stack is deformed uniformly both in the length direction (a_1) and thickness direction (a_3), the displacement of the clay stack in the load direction can be expressed as:

$$u_p = \delta a_3 \cos\theta \ , \tag{5.1}$$

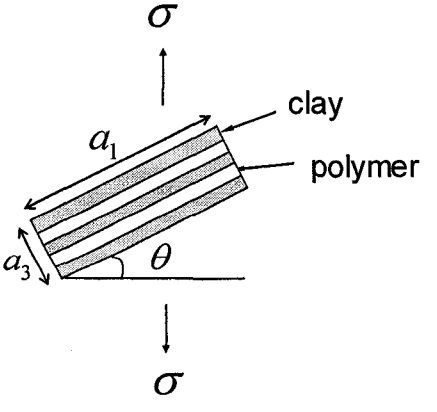

Figure 5.1 Model for intercalated clay stack.

where θ is the angle between the clay plane and the normal to the load. When an overall tensile stress (σ) is applied on a RVE, the force applied on a clay stack becomes $\sigma a_1^2 \cos\theta$. Since the force component in the direction of clay thickness is $\sigma a_1^2 \cos^2\theta$, the displacement δa_3 is calculated from the linear stress-strain relationship as:

$$\delta a_3 = \frac{\sigma a_3 \cos^2\theta}{E_R}, \tag{5.2}$$

where E_R is the elastic modulus for the laminated composite by the Reuss model ($\theta = 0$). Originally, the Reuss model was made for large-particle composites. However, since the intercalated clay stacks have a dimension greater than 100 nm, the Reuss model does apply in this model. Inserting Eq. (5.2) into Eq. (5.1) u_p is obtained as:

$$u_p = \frac{\sigma a_3 \cos^3\theta}{E_R}. \tag{5.3}$$

In the case of zero clay content, the corresponding displacement in the direction of load is

$$u_0 = \frac{\sigma a_3}{E_m \cos\theta}, \tag{5.4}$$

where E_m is the elastic modulus of polymer matrix. Thus, the decrease of the tensile displacement of an intercalated clay stack due to the presence of the clay is

$$u = u_0 - u_p = \frac{\sigma a_3}{\cos\theta}\left(\frac{1}{E_m} - \frac{\cos^4\theta}{E_R}\right). \tag{5.5}$$

The decreased overall strain due to a clay stack can be obtained by using the RVE concept as

$$\bar{\varepsilon}^{\alpha} = \frac{1}{V}\frac{2}{\pi}\int_0^{\frac{\pi}{2}} u \cdot a_1^2 \cos\theta \, d\theta = \frac{a_1^2 a_3}{V}\sigma\left(\frac{1}{E_m} - \frac{3}{8E_R}\right). \tag{5.6}$$

In Eq. (5.6), $a_1^2 a_3 V^{-1}$ is the volume fraction of the intercalated clay region and can be expressed using the volume fraction of clay particles (v_p) as [Jo et al. 2006]:

$$v_{pi} = v_p\left(1 + \frac{n_c - 1}{n_c}\frac{d_m}{d_p}\right), \tag{5.7}$$

where n_c is the number of clay layers in each intercalated clay stack, d_p and d_m are the clay layer thickness and clay layer spacing, respectively. Then, the overall strain decreased by all intercalated clay stacks are

$$\bar{\varepsilon}^p = N\bar{\varepsilon}^\alpha = v_{pi}\sigma\left(\frac{1}{E_m} - \frac{3}{8E_R}\right). \tag{5.8}$$

Thus, the effective strain becomes $\bar{\varepsilon} = \varepsilon^0 - \bar{\varepsilon}^p$ and by using $\varepsilon^0 = \sigma/E_m$ and $E_R = (E_m E_p)\left[E_m v_{pi} + E_p(1 - v_{pi})\right]^{-1}$, the effective elastic modulus of HDPE/clay nanocomposites is yielded as

$$\bar{E}_c = E_m'\left\{1 - v_{pi} + \frac{3v_{pi}}{8E_p}\left[E_p - v_{pi}\left(E_p - E_m'\right)\right]\right\}^{-1}, \tag{5.9}$$

in which E_m' is the elastic modulus of HDPE containing PE-g-MAn. When PE-g-MAn is added to the HDPE the elastic modulus increases by 4% compared to the pure HDPE [Gopakumar et. al 2002]. In Eq. (5.9), the modulus of the volume between the clay layers is assumed to have the same modulus as clay layers. The macromolecular chains intercalated in clay layers are confined in a very small space and their behavior is quite different from those in bulk matrix, which results in macromolecules becoming rigid [Yano et. al 1993, Usuki et. al 1995, Ji et. al 2002]. Also, the increase of the tensile modulus at the interfacial region between the polymer matrix and clay particles was proved by Ji et al. [Ji et. al 2002]. Therefore, the elastic modulus in the intercalated region can usually be regarded as the same as that of clay particles.

5.2.2 Elastic modulus of HDPE/clay nanocomposite foams

Since most HDPE/clay nanocomposite foams have relatively low volume expansion ratios [Lee YH et al. 2005, Rachtanapun et al. 2003, Rachtanapun et al. 2004], the following two conditions can be considered in the modeling of the elastic modulus: there is a dilute distribution of the voids in the polymer matrix and the voids are randomly distributed. In this study, the shape of voids in the foams is assumed as spherical cavities. Under the uniaxial tensile loading, the cavities in RVE cause an increase of the tensile strain. Thus, the overall

strain increment of the polymer nanocomposites containing voids can be estimated from the locally incremented strains. Within the volume V of RVE, the average strain ($\bar{\varepsilon}$) is expressed as

$$\bar{\varepsilon} = \bar{\varepsilon}^0 + \bar{\varepsilon}^c \ , \tag{5.10}$$

where $\bar{\varepsilon}^0$ is the average strain of the RVE without cavities, and $\bar{\varepsilon}^c$ is the additional strain increment due to the presence of the cavities. The magnitude of $\bar{\varepsilon}^c$ can be obtained by using the virtual stress-strain concept on the cavity surfaces and reciprocal theorem [Nemat-Nasser and Hori 2003] as

$$\bar{\varepsilon}^c = \frac{1}{V}\int_{\partial\Omega}\frac{1}{2}(n\otimes u + u\otimes n)dS \ , \tag{5.11}$$

where $\partial\Omega$ denotes cavity surface, n is the exterior unit normal vector on the cavity surface and u is the displacement vector resulting from actual loading. When the coordinate axes are formed at the center of a spherical cavity of radius R, the displacement field in the infinite elastic body under uniaxial remote tension (σ), as derived within the linear elastic theory [Li et al. 2006], is

$$\begin{aligned} u_r = {} & \frac{\sigma r}{4\mu}\left[\frac{2+\Lambda}{2+3\Lambda} + \frac{13+8\Lambda}{14+9\Lambda}\left(\frac{R}{r}\right)^3 - \frac{3(1+\Lambda)}{14+9\Lambda}\left(\frac{R}{r}\right)^5\right] \\ & + \frac{\sigma r}{4\mu}\left[1 + \frac{5(5+3\Lambda)}{14+9\Lambda}\left(\frac{R}{r}\right)^3 - \frac{9(1+\Lambda)}{14+9\Lambda}\left(\frac{R}{r}\right)^5\right]\cos 2\theta \end{aligned} \ , \tag{5.12}$$

where r is the radial distance in the spherical coordinate and θ is the angle from the tensile loading axis. The parameter Λ is expressed as $\Lambda = \lambda/\mu$, where λ is a Ramé constant and μ is the shear modulus. The radial displacement at the surface of the spherical cavity is obtained from Eq. (5.12), where $\Lambda = 2\nu/(1-2\nu)$ is used:

$$u_R = \frac{3\sigma R(1-\nu)}{\mu(7-5\nu)}\left(\frac{1}{1+\nu} + \frac{5}{4}\cos 2\theta\right) , \tag{5.13}$$

where ν is the Poisson's ratio. The additional overall volumetric strain resulting from a cavity is defined as

$$\bar{\varepsilon}^R \equiv \frac{1}{V}\int_{\partial\Omega_R}\frac{1}{2}(n\otimes u + u\otimes n)dS \ . \tag{5.14}$$

Thus, $\bar{\varepsilon}^R$ is obtained by substituting u_R into Eq. (5.14) and integration from $\theta = 0$ to $\theta = \pi$ as

$$\bar{\varepsilon}^R = \frac{1}{V}\int_{\partial\Omega_R} u_R dS$$
$$= \frac{1}{V}\frac{3\sigma R(1-\nu)}{\mu(7-5\nu)} 2\pi R^2 \left(2\int_0^{\pi/2} \frac{1}{1+\nu}\sin\theta d\theta + 2\int_0^{\pi/2} \frac{5}{4}\cos 2\theta \sin\theta d\theta \right). \quad (5.15)$$
$$= \frac{1}{V}\frac{\pi R^3(1-\nu)}{\mu(1+\nu)}\sigma$$

For simplicity's sake, when all cavities in RVE are assumed to be uniform and have dilute distribution, then $\bar{\varepsilon}^c = N\bar{\varepsilon}^R$, where N is the total number of cavities per unit volume.

The applicability of dilute distribution and uniform distribution of cavities in this model is verified quantitatively by comparing the stress over the surrounding of the cavity with overall stress. In the dilute distribution of micro-inclusions, the interactions among inclusions are not considered. Also, the inclusions are assumed to be distributed evenly throughout the volume. In this situation, elastic moduli do not depend on a distance between inclusions [Lubarda and Richmond 1999]. When the overall stresses are assumed to be prescribed, it underestimates the effect of the interaction between cracks [Yin and Ehrlacher 1996]. However, prescribed stress is not considered in this model. First, the distance between cells in the foams is calculated with the following model. If the voids in the foam are assumed as spherical cavities and densely packed in a cube, a packing model of the spheres in the cube can be proposed. When the diameter of spheres and the dimension of cube is d and d_1 (= n × d), respectively, n spheres are arrayed along one edge of cube. Then, another array is added at the next of the first array so that each of the spheres can be located between the spheres in first array, where the distance between the first array and the second array is calculated as $\left(\sqrt{3}/2\right)$d. So, $\left(2/\sqrt{3}\right)$ arrays are located on the other side of cube. Now, n × $\left(2/\sqrt{3}\right)$n spheres are packed on a plane. Next, the same plane arrays are placed on top of the first plane array so that each of the spheres in the second plane can be positioned at the center of the three spheres in the first plane. Then, the distance between planes is (3/4)d. Therefore, the total number of spheres packed in the cube becomes n × $\left(2/\sqrt{3}\right)$n × (4/3) n = $\left(8/3\sqrt{3}\right)$n^3. This packing model can be an example of the distribution of cells in the foams which have uniform distance among cells. In this case, the distance among cells is equal to d because all adjacent spheres are contacted at the surface of the sphere and the

center of cells is coinciding with the center of the spheres. In this model, the size of cells should be smaller than the spheres and is assumed to have diameter d′. Then, the volume of cells in the foam is expressed as $(4\pi)(d'/d)^3 d_1^3/(9\sqrt{3})$, where n = d_1/d was used. The volume ratio of air in the cube foam is $(4\pi)(d'/d)^3/(9\sqrt{3})$, and is equal to $(1-1/V_R)$, where V_R is the volume expansion ratio of foams. Therefore, the ratio of the distance between cells and cell diameter is represented as a function of volume expansion ratio as

$$\frac{d}{d'} = \left[\frac{9\sqrt{3}}{4\pi}\left(1-\frac{1}{V_R}\right)\right]^{-\frac{1}{3}}, \tag{5.16}$$

and plotted in Fig. 5.2.

In the range of the volume expansion ratio from 1.02 to 1.07, the ratios of the distance between cells and cell diameter were 2.5 – 3.5. Next, the influence of stresses due to a cavity over the surroundings of the cavity is investigated. When an external remote tension load is applied at infinity, the tangential component of the stress at cavity is expressed as [Krstic 1985]:

$$\sigma_\theta = \frac{\sigma_0}{2}(1-\cos 2\theta)+\sigma_0\left\{\begin{array}{l}\dfrac{13}{4(7-5\nu)}\left(\dfrac{R}{r}\right)^3-\dfrac{3}{4(7-5\nu)}\left(\dfrac{R}{r}\right)^5 \\ +\left[\dfrac{5(1-2\nu)}{4(7-5\nu)}\left(\dfrac{R}{r}\right)^3-\dfrac{21}{4(7-5\nu)}\left(\dfrac{R}{r}\right)^5\right]\cos 2\theta\end{array}\right\}, \tag{5.17}$$

where R is the radius of cavity, r is the radial distance from the center of cavity, and ν is Poisson's ratio. To investigate the effect of this stress on other cavities, the magnitude of this stress in the direction of applied load ($\theta = \pi/2$) is calculated between cavities. As shown in Fig. 5.3, this stress has maximum at the surface of the cavity and decrease as r increases. Since the influence of this stress is almost disappeared at the distances longer than 2.5 times of the cavity radius, the interactions between cells can be negligible in the r/R range between 2.5 and 3.5. Thus, the distribution of cells in HDPE/clay nanocomposite foams can be regarded as a dilute distribution because the interactions among cells may not be considered.

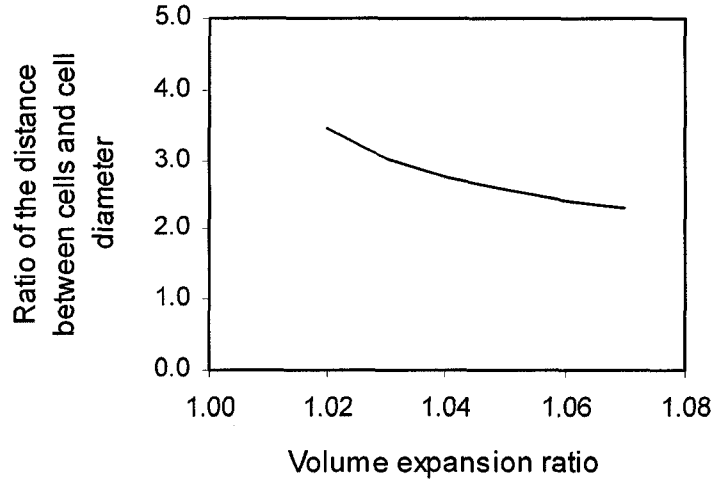

Figure 5.2 The ratio of the distance between cells and cell diameter represented as a function of volume expansion ratio.

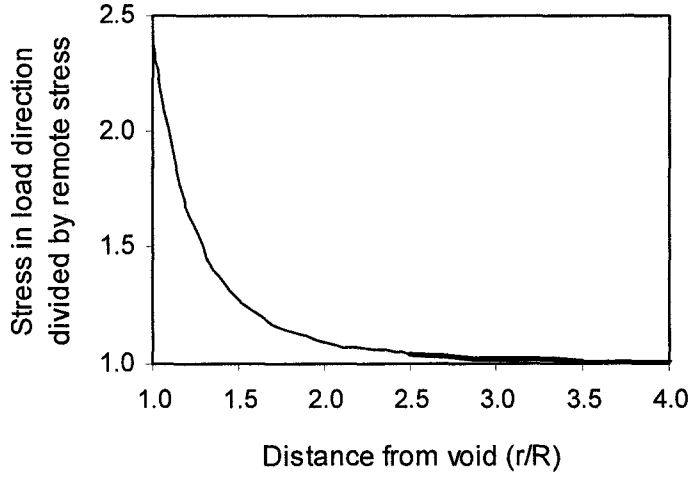

Figure 5.3 Stress concentration factor in load direction between cells.

Therefore, the additional volumetric strain due to the presence of the cavities can be expressed by

$$\bar{\varepsilon}^{c} = f\frac{3(1-\nu)}{4\mu(1+\nu)}\sigma \ , \tag{5.18}$$

where f is the volume fraction of the cavities in RVE. The additional volumetric strain in Eq. (5.18) is the sum of the component in the direction of uniaxial tensile stress and the component in the other two perpendicular directions. Then, within the isotropic linear elasticity, the component of additional volumetric strain in the direction of tensile stress (σ) is obtained as

$$\bar{\varepsilon}_{xx}^{\ c} = (1-2\nu)\bar{\varepsilon}^{c} \ . \tag{5.19}$$

Thus, the average strain defined in Eq. (5.10) is modified for the effective strain in the uniaxial stress direction as

$$\bar{\varepsilon} = \bar{\varepsilon}^{0} + \bar{\varepsilon}_{xx}^{\ c} \ . \tag{5.20}$$

By using $\bar{\varepsilon} = \sigma/\bar{E}$ and $\bar{\varepsilon}^{0} = \sigma/E$, Eq. (5.20) is changed to

$$\frac{\sigma}{\bar{E}} = \frac{\sigma}{E} + (1-2\nu)f\frac{3(1-\nu)}{4\mu(1+\nu)}\sigma \ . \tag{5.21}$$

Then, the overall elastic modulus is expressed as

$$\bar{E} = \left[\frac{1}{E} + (1-2\nu)f\frac{3(1-\nu)}{4\mu(1+\nu)}\right]^{-1} \ . \tag{5.22}$$

If the volume fraction of cavities is converted to the relative density of foams (ρ_r) and shear modulus is expressed by elastic modulus, the ratio of elastic modulus of foams ($\bar{E}^{*}$) and that of unfoamed polymer is yielded as

$$\frac{\bar{E}^{*}}{E} = \left[1-(1-\rho_r)\frac{3(1-\nu)}{2(1-2\nu)}\right] \ . \tag{5.23}$$

Eq. (5.23) is valid at the beginning of the tensile deformation because both unfoamed and foamed materials show linear elastic property at the starting of the deformation. Therefore, replacing E in Eq. (5.23) with the elastic modulus of HDPE/clay nanocomposites (Eq. (5.9)), the elastic modulus of foams ($\bar{E}^{*}$) is yielded as a function of the relative density of foams (ρ_r),

$$\bar{E}_c^* = E_m' \left\{ 1 - v_{pi} + \frac{3v_{pi}}{8E_p} \left[E_p - v_{pi} \left(E_p - E_m' \right) \right] \right\}^{-1} \left[1 - (1-\rho_r) \frac{3(1-\nu)}{2(1-2\nu)} \right] . \quad (5.24)$$

This expression is valid for the foams which have low void fractions.

5.2.3 Constitutive equation

The tensile behavior of HDPE/clay nanocomposite foams can be described by viscoelastic-plastic constitutive model. For overall behavior of polycrystal structure, a self-consistent approach using large deformation viscoplastic theory was developed by Molinari et al. [Molinari et al. 1987], where elasticity was neglected. Since the amorphous phase plays a predominant role in many aspects of the properties of semi-crystalline polymers [Lin and Argon 1994], elastic part of tensile deformation is considered first in the present thesis, and viscoplasticity model is left for future study. The mechanism of elastic deformation in response to tensile stress is due to the elongation of the chain molecules in the direction of the applied load. The semi-crystalline polymers can be modeled using lamellar crystal layers separated by amorphous layers. Among the deformation mechanisms of amorphous layers of HDPE, interlamellar shear parallel to the lamellae is dominant in the early phase of deformation [Bartczak et al. 1992a, Bartczak et al. 1992b]. To describe the overall elastic behavior by shear deformation of amorphous layers, a three-element viscoelastic model (Fig. 5.4) can be used, where the proposed elastic modulus of foams can be applied directly.

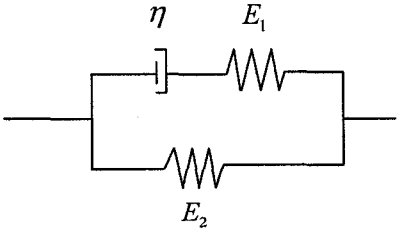

Figure 5.4 Three-element viscoelastic model.

The elastic modulus E_1 in Fig. 5.4 depends on the strain rate [Nikolov and Doghri 2000]. However, it is considered as a constant for simplicity sake because a constant strain rate is used in this study. The equation of motion of the three-element viscoelastic model is

$$\dot{\sigma}+\frac{E_1}{\eta}\sigma=\frac{E_1E_2}{\eta}\varepsilon+\left(E_1+E_2\right)\dot{\varepsilon}\ . \tag{5.25}$$

The corresponding constitutive relation is obtained from Eq. (5.25) as

$$\sigma=\bar{E}\varepsilon-\frac{\eta}{\tau}\varepsilon+\eta\dot{\varepsilon}\left[1-\exp\left(-\frac{\varepsilon}{\tau\dot{\varepsilon}}\right)\right], \tag{5.26}$$

where the equivalent elastic modulus ($\bar{E}$) and relaxation time constant (τ) [Jo 2005] are E_1+E_2 and ηE_1^{-1}, respectively. When Eq. (5.26) is used for HDPE/clay nanocomposite foams Eq. (5.24) is substituted for $\bar{E}$. The crystallinity was not used in Eq. (5.26). However, the influence of crystallinity is controlled indirectly by viscoelastic parameters.

5.3 Experimental

Microcellular HDPE/clay nanocomposite foams were manufactured in a batch processing method and their physical and mechanical properties were obtained by experiment.

5.3.1 Materials

High density polyethylene (SCLAIR 59A, Nova Chemicals) with a density of 0.962 g/cm^3 (ASTM D792) and a melt index of 0.72 g/10min (ASTM D1238) was used. Organically modified clay with dimethyl dehydrogenated tallow alkyl ammonium (Cloisite 20A, Southern Clay Products) was employed as the layered silicate. The maleic anhydride-grafted HDPE (PE-g-MAn, Fusabond MB100D, DuPont Canada) was used as the coupling agent. A commercial grade carbon dioxide provided by Praxair was utilized as the blowing agent.

5.3.2 Preparation of HDPE/clay nanocomposites

HDPE/clay nanocomposites were prepared using a parallel counter-rotating intermeshing twin-screw extruder (Model D6/2, C.W. Brabender, diameter = 42 mm, L/D = 10) having a barrel temperature profile ranging from 140 to 180°C from the feeding zone to the die zone. The residence time depends on screw rpm and the characteristics of materials like MFI or viscosity. In this case, the screw speed was set as 70 rpm. HDPE and Cloisite 20A were used as it is without special treatment. Prior to extrusion, organoclay powder, PE-g-MAn and HDPE were mixed thoroughly in a container and placed into the hopper of a screw feeder. The PE-g-MAn content was fixed at 15 wt.% and the clay contents were varied at 0.5, 1.0, and 2.0 wt.%. The extrudate was pelletized. The pelletized HDPE/clay nanocomposites were then compression molded with a hydraulic heated press machine (Caver Inc.) for 10 minutes using five tons of force (1.52 MPa). The temperature of the hot pressing plates was 160°C. The molded samples were quenched in cold water to room temperature. The size of compression-molded samples was 6 mm × 50 mm × 1.55 mm (width × length × thickness).

5.3.3 Microcellular foaming

A batch microcellular foaming process was used for foaming of HDPE and HDPE/clay nanocomposites.

In the first stage, the compression-molded samples were saturated in a pressurized CO_2 chamber at 5.8 MPa and room temperature for 85 hours. As an alternate saturation method, the compression-molded samples were saturated in a pressurized CO_2 chamber at 8.3 MPa and room temperature for 3 days. For a long time, CO_2 was completely saturated in the sample at this condition. Then, the pressure was released rapidly to supersaturate samples with CO_2, and the samples were immersed in a hot glycerin bath for foaming, where the foaming temperature was 130°C. In order to control the expansion ratio, variable foaming times were used. The foamed samples were immediately quenched in cold water to prevent cell deterioration.

The foam density (ρ_f) was measured by a buoyancy method using a density determination kit supplied by Denver Instrument. The Archimedean principle was applied for determining the specific gravity of the foams. The relative foam density (ρ_r) is defined

as the ratio of foam density to the unfoamed sample density, while the volume expansion ratio is the ratio of the unformed sample density to the foam density.

5.3.4 Sample characterization and mechanical testing

Foam density was measured by a buoyancy method using a density determination kit supplied by Denver Instruments. The Archimedean principle was applied for determining the specific gravity of the foams. The relative foam density is defined as the ratio of the foamed to unfoamed polymer density, whereas the expansion ratio is defined as its inverse.

The morphology of HDPE/clay nanocomposites was studied by transmission electron microscope (TEM) analysis. Ultra thin sections (70nm thickness) of the nanocomposite samples were cut by ultracryomicrotome equipped with a diamond knife. Images were recorded using a Hitachi HD-2000 STEM microscope operating at 200 kV.

The foam samples were examined using scanning electron microscope (SEM). The samples were coated using a cold coating process by applying a thin layer of gold with the aid of a sputter coater (SEM Coating Unit PS3). The gas pressure was set at 2 kPa (20 mbar) and the current was applied at 9–10 mA. The entire coating time lasted 70 seconds. The edges of the coated samples and the SEM mounts were then painted with a conductive carbon paste. A JSM scanning electron microscope (Model 6060) was then operated at 20 kV, and images were acquired from several locations on each sample.

Uniaxial tensile mechanical tests were performed with rectangular strip samples. The dimension of samples, gage length and test speed were determined according to the ASTM D638, and Instron 4482 machine with a 100 kN load cell was used. A crosshead speed of 50 mm/min at room temperature was used, and the strain was measured based on the change in the displacement of the crosshead. The elastic modulus was obtained from the maximum slope at the initial elastic portion of the stress-strain curves. The tensile strength and elongation at break were also reported. A minimum of five specimens were tested for each data point, and the averages were reported.

5.4 Results and Discussion

5.4.1 Effect of nanoclay and foaming conditions on the mechanical properties

The transmission electron micrographs of HDPE/clay nanocomposites are shown in Fig. 5.5. In all of three clay loading cases, intercalated clay clusters dispersed in the polymer matrix are detected. As shown in the figure the thickness of intercalated clay clusters is decreased as clay content increases, which means that interlayer spacing in clay clusters is decreased as clay content increases. Fig. 5.6 shows the scanning electron micrographs for foamed samples. HDPE/clay nanocomposites produced foams of smaller cell size ($\approx 1\,\mu$m) and also show low foaming grade. This phenomenon is due to low solubility and diffusivity of CO_2 by the crystalline structure in HDPE. In general, compared to the amorphous polymer, foaming of the semicrystalline polymer is difficult because of the crystalline structures in the semicrystalline polymer, which was demonstrated in references [Jo et al. 2006, Lee YH et al. 2005, Doroudiani et al. 1996, Doroudiani et al. 1998], where the expansion ratio was decreased with increasing crystallinity. Also, the foaming grade of HDPE is usually decreased with increasing molecular weight or with decreasing melt flow index [Zhang Y et al. 2003]. With increasing molecular weight, cell size is decreased and cell density is increased [Zhang Y et al. 2003].

The effects of clay contents and foaming times on the volume expansion ratio of HDPE/clay nanocomposite foams are shown in Fig. 5.7. The figure indicates that relatively low void fractions were achieved. This result is similar to the Rachtanapun's [Rachtanapun et al. 2003] experimental result, where the volume expansion ratios of HDPE foams could reach up to 1.067. From Fig. 5.7, it was demonstrated that clay particles provide favorable condition for foaming, in HDPE. Since the crystallinity decreases with increasing clay contents [Min et al. 2006], high clay loadings result in a drop in crystallinity and, consequently, can result in a favorable effect on foaming. Higher volume expansion can be achieved by increasing the foaming temperature [Rachtanapun et al. 2003, Rachtanapun et al. 2004], or by using low-molecular-weight HDPE, or lower viscosity material [Zhang Y et al. 2003]. However, high foaming temperature may cause the deformation of the samples and, as a result, decrease the mechanical strength.

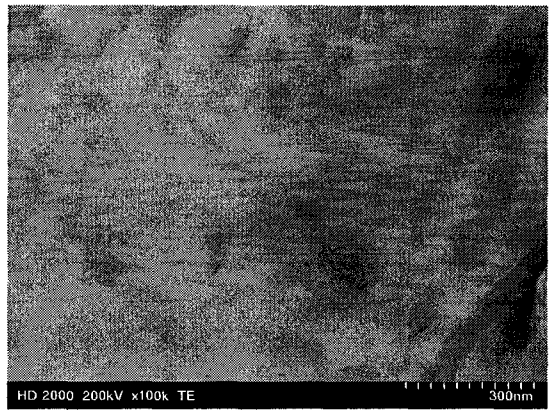

(a)

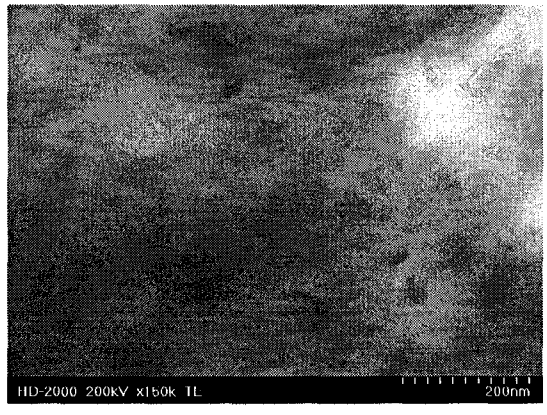

(b)

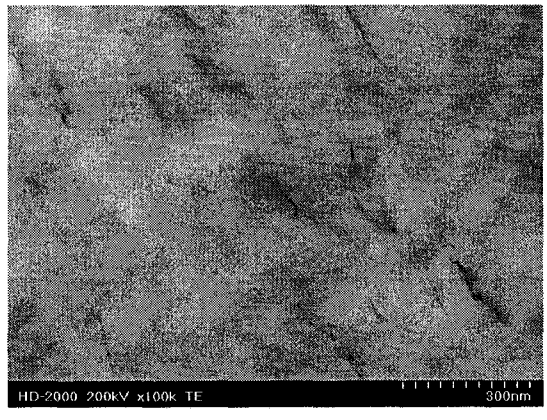

(c)

Figure 5.5 Transmission electron micrographs of HDPE/clay nanocomposites: (a) 0.5 wt% clay; (b) 1.0 wt% clay; (c) 2.0 wt% clay.

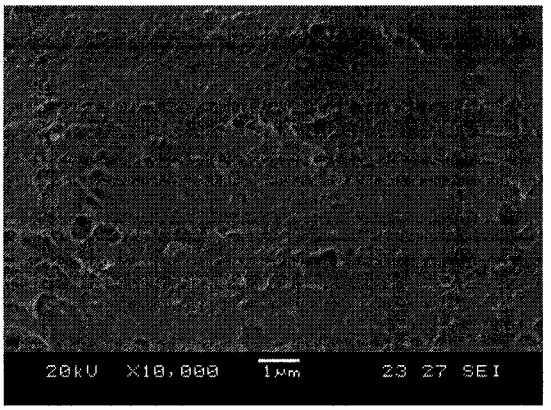

(a)

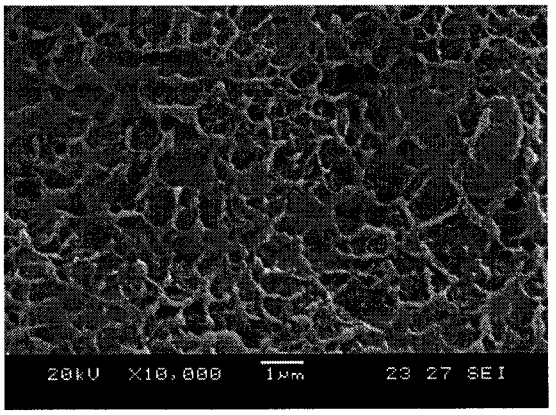

(b)

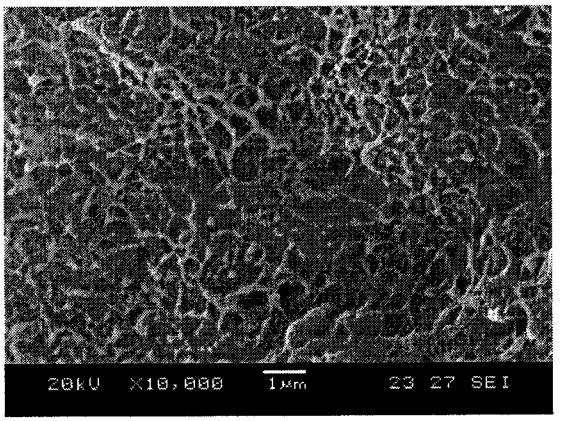

(c)

Figure 5.6 Scanning electron micrographs of HDPE/clay nanocomposite foams: (a) 0.5 wt% clay; (b) 1.0 wt% clay; (c) 2.0 wt% clay.

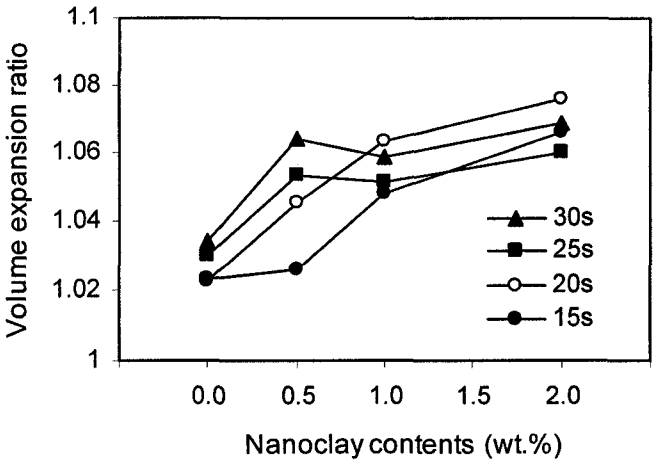

Figure 5.7 Effect of clay content and foaming time on the volume expansion ratio of HDPE/clay nanocomposite foams.

In the cases where high saturation pressure (8.3 MPa) was used, the effects of clay contents and foaming conditions on the volume expansion ratio of HDPE/clay nanocomposite foams are shown in Fig. 5.8. When foaming time longer than 30s was used, the void fraction increased at all three clay loadings, and also the maximum value of the volume expansions achieved at the three clay contents were almost the same. Except 1.0 wt.% clay loading, the foaming could be deteriorated by a long foaming time.

The elastic modulus of HDPE was improved by 9% when nanoclays were added (Fig. 5.9). However, the effect of the variation of the clay contents was small. This could be a result of the intercalated fraction of the clays in HDPE. Other researchers reported that the clay fraction in HDPE has little effect on the intercalation extent within 5 wt.% clay loading range [Doroudiani et al. 1996]. This phenomenon is different from the case of PMMA/clay nanocomposites [Fu and Naguib 1996], where the modulus was increased by 50% with 0.5 wt.% clay loadings and decreased gradually as clay contents increase after 0.5 wt.% clay loading. It can be deduced from this comparison that the amorphous polymer has reinforced more than the semicrystalline polymer.

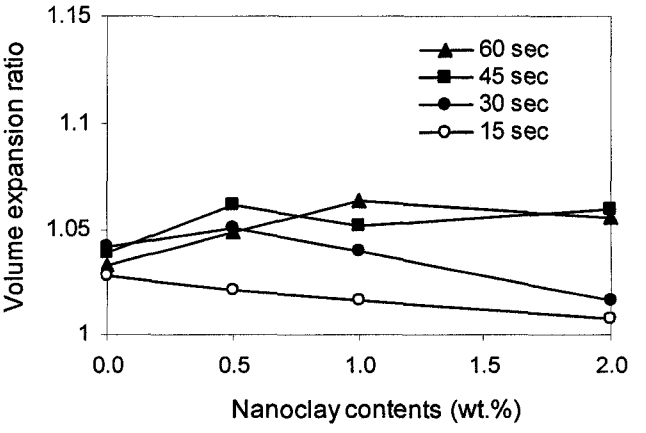

(a)

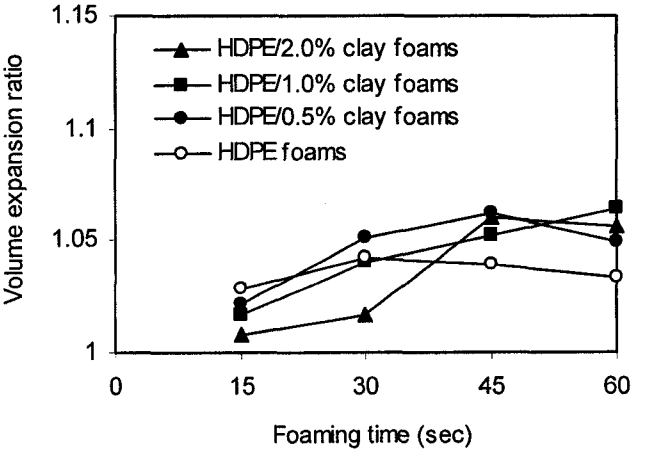

(b)

Figure 5.8 Volume expansion ratio of HDPE foams and HDPE/clay nanocomposite foams as a function of: (a) clay content and (b) foaming time.

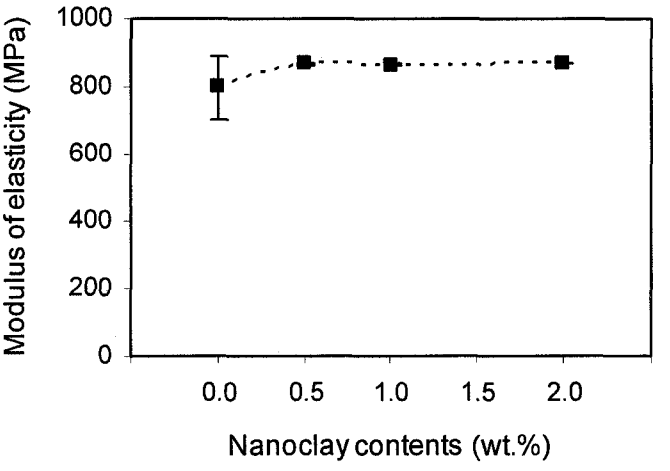

Figure 5.9 Effect of clay loadings on the elastic modulus of HDPE/clay nanocomposites.

The effects of clay loadings on the elastic modulus of HDPE/clay nanocomposite foams were compared with foam density in Fig. 5.10. As shown in the figure, the reinforcing effect of the clays on the elastic modulus of foams was maximized when clay loading was 0.5 wt.%, and then decreased as clay content increases. This decreasing phenomenon implies that some of the nanoclays acted as a deteriorating effect in the foams. Lee et al. [Lee JH et al. 2005] reported that some stacked clays were found above 3 wt.% clay loading when PE-g-MA was used as compatibilizer in synthesizing nanocomposites.

The tensile strength was also improved by 5-7% by adding nanoclays as shown in Fig. 5.11. When HDPE/clay nanocomposites contain partially intercalated/exfoliated clays, their tensile modulus and tensile strength could increase continuously up to 7 wt.% clay loadings [Lee JH et al. 2005]. In this study, however, the tensile strength creates no big difference to the change of the clay contents within 2.0 wt.% clay loadings and some decreasing phenomenon after 1.0 wt.% was found out as well. This implies that some of the clays in the samples remain stacked state and applied as a retrogressive effect on the reinforcing process. Murphy et al. [Murphy et al. 2003] also investigated that organoclay loading in polyethylene had an adverse effect on the tensile yield stress.

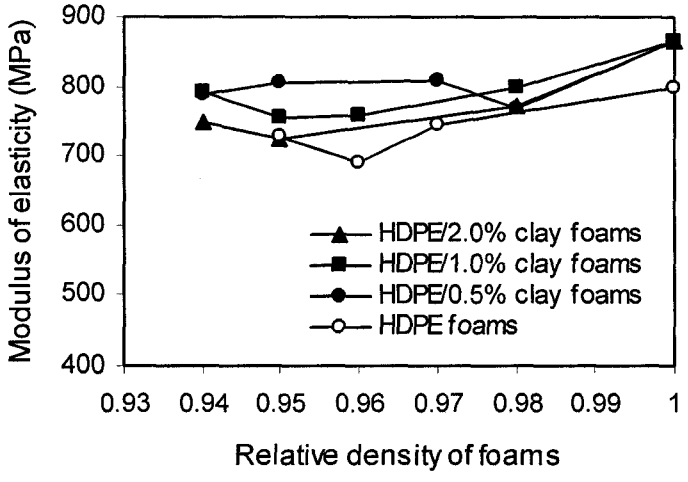

Figure 5.10 Elastic modulus of HDPE/clay nanocomposite foams.

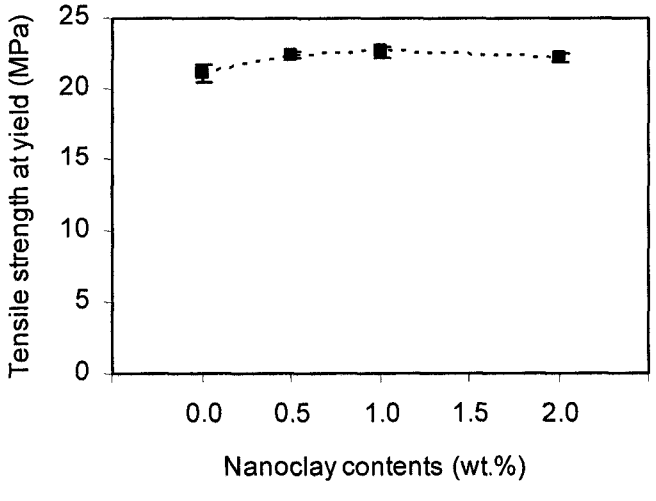

Figure 5.11 Effect of clay loadings on the tensile strength of HDPE/clay nanocomposites.

As shown in Fig. 5.12, the HDPE/clay foams containing 0.5 wt% nanoclay had higher tensile strength than other clay loadings.

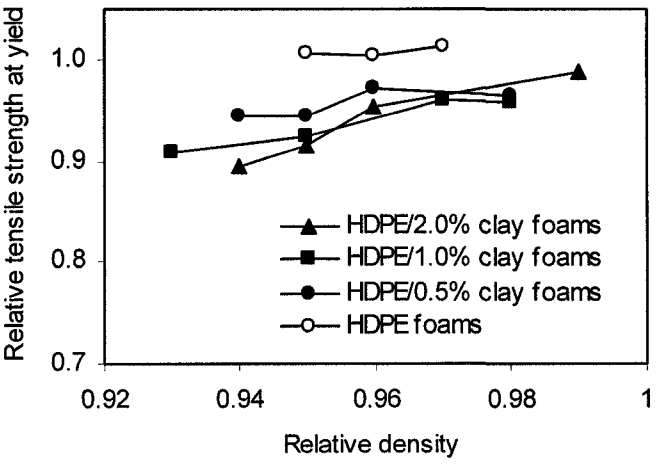

Figure 5.12 Effect of clay loadings on the relative tensile strength at yield of HDPE/clay nanocomposite foams.

The percent elongation at yield decreased by 20 % when nanoclays were added to the HDPE, but the variation of the percent elongation between 0.5 % and 2.0 % clay loadings was small as shown in Fig. 5.13. The decrease in yield strain is probably due to the confined movement of the polymer between the clay particles. The percent elongation at break of HDPE was considerably reduced with the addition of nanoclays (Fig. 5.14). As foaming increases, the percent elongation at break decreased in general (Fig. 5.15). Also, the percent elongation at break decreased as the clay content increased. Similarly to the tensile strength, the highest percent elongation of the foams was obtained at 0.5 wt% clay loading.

The uniaxial tensile test results of the HDPE/clay nanocomposites and nanocomposite foams were plotted in Fig. 5.16. The HDPE/clay nanocomposites show plastic deformation resulting from the separation of the crystalline block segments in HDPE. By adding clay particles, the elastic modulus and tensile strength of HDPE were improved somewhat. However, the percent elongation at break decreased greatly as the clay content increased. The percent elongation at yield of HDPE/clay nanocomposites changed a little with clay loading. It was demonstrated that nanoclays in HDPE, with proper clay contents, have a role to improve the mechanical properties, such as elastic modulus and tensile strength.

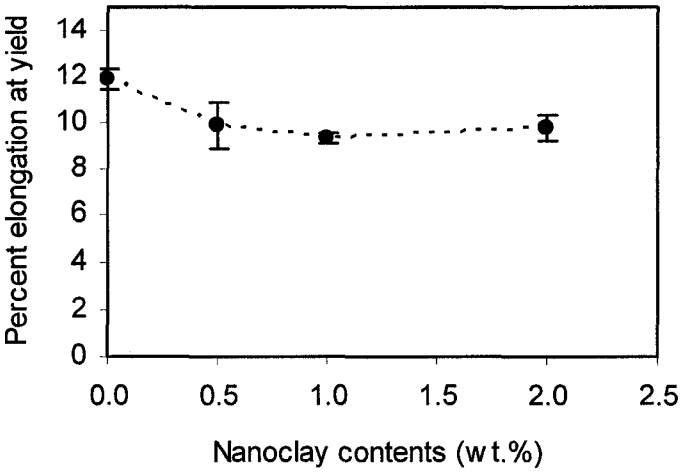

Figure 5.13 Percent elongation at yield of HDPE/clay nanocomposites.

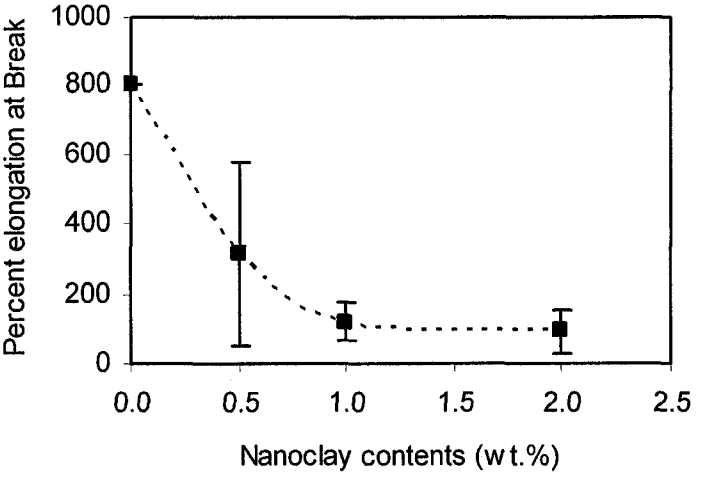

Figure 5.14 Percent elongation at break of HDPE/clay nanocomposites.

In addition, tensile properties of HDPE/clay foams are reinforced when compared to that of pure HDPE foams. In the case of both nanocomposites and nanocomposite foams, the mechanical properties are improved most at 0.5 wt% clay loadings.

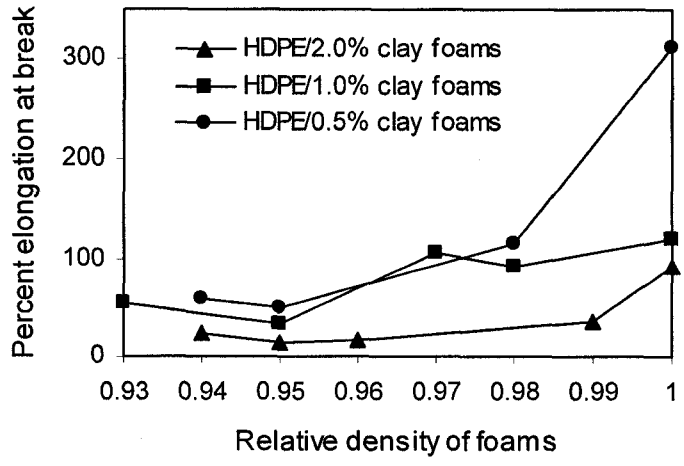

Figure 5.15 Percent elongation at break of HDPE/clay nanocomposite foams.

5.4.2 Comparison of the constitutive models with experiments

Dispersed clay platelets in HDPE led to increased elastic properties, and also resulted in a reduction of the degree of crystallinity [Gopakumar et al. 2002]. In this experiment, the elastic modulus of HDPE was improved by 9 % when nanoclays were added (Fig. 5.17). However, the variation of the elastic modulus by increasing clay contents was small. This could be a result of the degree of the intercalation. Other researchers reported that the clay fraction in HDPE has little effect on the intercalation extent within 5 wt% clay loadings [Zhong and Kee 2005]. In Fig. 5.20, theoretical prediction was compared with the test results. In the model, d_m/d_c = 5, 4, and 3 were used for 0.5, 1.0, and 2.0 wt% clay composites, respectively, which were determined on the basis of XRD studies of HDPE/clay nanocomposites [Osman et al. 2005, Swain and Isayev 2007, Tzavalas et al. 2006, Liang et al. 2004]: When 1.0 and 2.0 wt% clay (Cloisite 20A) concentration was used the d-spacing of the clay was measured as 35 Å [Tzavalas et al. 2006] and 30 Å [Zhong and Kee 2005], respectively, which indicates that macromolecular chains are intercalated into the interlayer of Cloisite 20A. In the case of these interlayer distances, the ratios of clay layer spacing and clay layer thickness (d_m/d_c) for 1.0 and 2.0 wt% clay concentration are calculated as 2.5

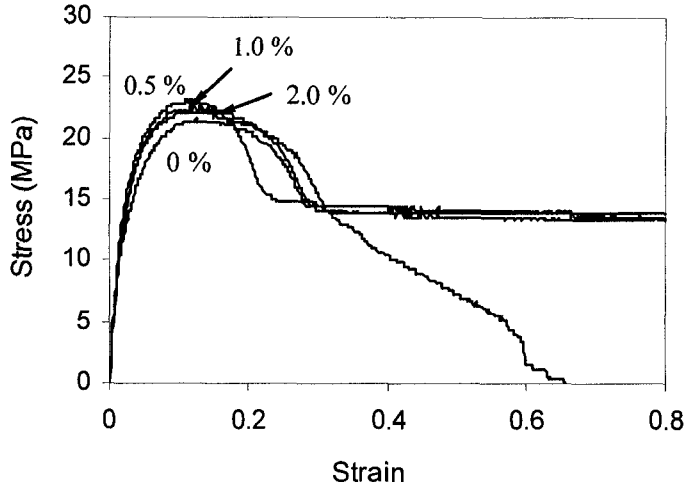

(a)

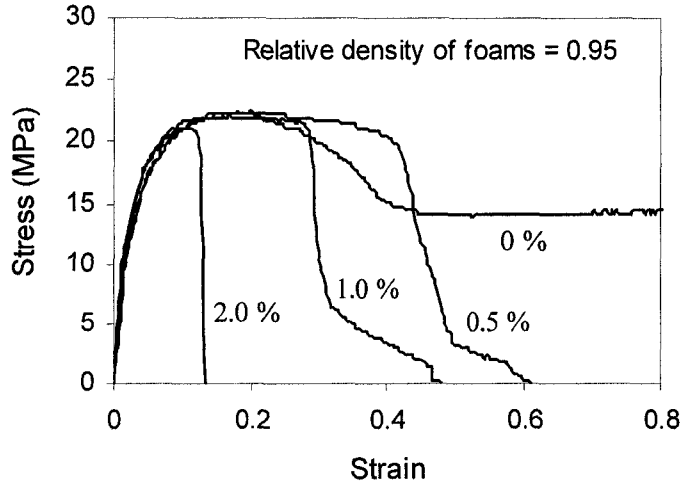

(b)

Figure 5.16 Effect of clay loadings on the tensile behavior of (a) HDPE/clay nanocomposites and (b) HDPE/clay nanocomposite foams.

and 2, respectively, in which 1 nm thickness of silicate layers was used [Giannelis et al. 1999]. Also, it was reported that the d-spacing of Cloisite 20A was enlarged from 24 Å to 35.6 Å at 2.5 wt% clay concentration [Swain and Isayev 2007], which corresponds to d_m/d_c = 2.6. No obvious change in clay layer spacing is found for HDPE/clay nanocomposite when the clay content increases from 2 to 5 wt%, however the d-spacing was proved to be decreased with increasing clay concentration [Zhong and Kee 2005, Swain and Isayev 2007]. The d-spacing of clays can also be increased by maleic anhydride grafted polyethylene (PE-*g*-MAn). When organic-montmorillonite (Org-MMT) is added in HDPE/clay nanocomposites the d-spacing of Org-MMT is increased as the content of PE-*g*-MAn increases [Liang et al. 2004]. Thus, in the present model, 1.5 times of d_m/d_c values were adopted as d_m/d_c = 4 and 3 for 1.0 and 2.0 wt% clay loadings, respectively, because 15 wt% of maleic anhydride grafted polyethylenes were used in the HDPE/clay nanocomposites. Also, for the case of 0.5 wt% clay loadings, more increased interlayer spacing of clays (d_m/d_c = 5) was used in the model. The number of clay layers (n_c) in each intercalated clay cluster was assumed as 5. As shown in Fig. 5.17, the developed model for the elastic modulus of HDPE/clay nanocomposites was found to have a trend similar to the experimental results.

The effect of the clay loadings on the elastic modulus of HDPE/clay nanocomposite foams are shown in Fig. 5.18. The reinforcing effect of the clays on the elastic modulus of foams was maximized when clay loading was 0.5 wt.%, and then decreased with increasing clay content. In other words, the rate of decrease of elastic modulus by foaming becomes the least at 0.5 wt.% clay loading. This decreasing phenomenon of the relative elastic modulus implies that some of the nanoclays acted to have a deteriorating effect on the foams after 0.5 wt.% clay loading. Lee et al. [Lee J-H et al. 2005] reported that some stacked clays were found above 3 wt.% clay loading when PE-g-MAn was used as a compatibilizer in synthesizing nanocomposites. In this case, montmorillonite was treated with a swelling agent (octadecylamine) before melt mixing to increase the interlayer distance of the clays. However, in this study, clays are used as received in the melt compounding. Accordingly, the deteriorating effect by stacked clays might be created before 3 wt.% clay loadings in this experiment. The theoretical models for tensile elastic modulus of HDPE/clay nanocomposite

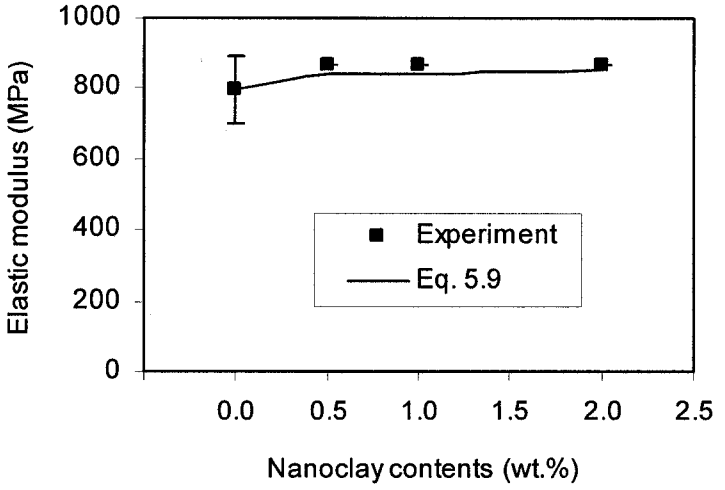

Figure 5.17 Effect of clay loading on the elastic modulus of HDPE/clay nanocomposites.

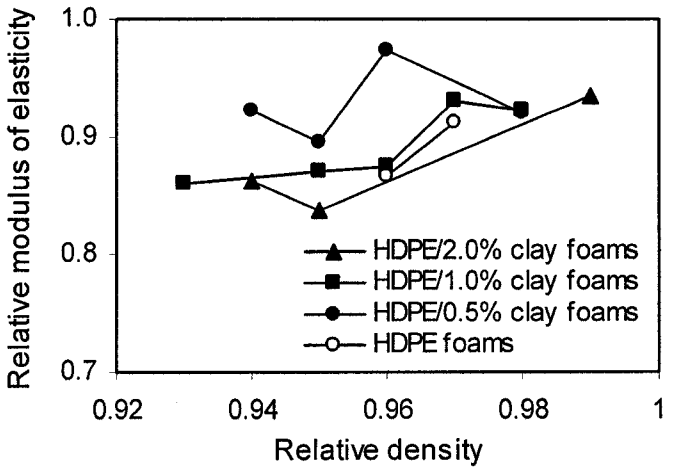

Figure 5.18 Effect of clay content on the relative elastic modulus of HDPE/clay nanocomposite foams.

foams were compared with the experimental results in Fig. 5.19, where the Poisson's ratio was fixed as 0.35. As shown in the figure, the elastic modulus decreased as the relative density decreases. As indicated in Fig. 5.19(a), Eq. (5.23) is representing the elastic modulus of foams at high relative density. Thus, the application of Eq. (5.23) in Eq. (5.24) is regarded as appropriate. The test results of the elastic modulus in Fig. 5.19(b) may look as consisted of three data groups, which is due to the limited recording system from the tensile test machine. Also the figure look as there is big deviation between experiment and prediction. However, the elastic modulus decreases with decreasing the relative density because the change of the experimental elastic moduli moves between data groups. Also, the theoretical curves in the figure are connecting the three data group. To compare the theoretical models with experimental results more accurately, 1% secant modulus was used in Fig. 5.19(c). The 1% secant modulus is smaller than the elastic modulus ($\approx$ 0% secant modulus) used in Fig. 7b by approximately 6.5 %. However, the 1% secant modulus can be representative of the tensile modulus in this experiment as it is quite close to the maximum modulus values. Also, the use of the modulus can be effective method for fully nonlinear elastic behavior as well as it can overcome the limit of the recording system of test machine. As shown in Fig. 5.19(c) the theoretical model (Eq. (5.24)) predicts the tensile elastic modulus well. Also, this model shows no big difference between clay contents as represented by experimental data.

The proposed constitutive model was compared with experimental results in Fig. 5.20. The effects of clay contents and relative density of foams on the tensile behavior were investigated with model prediction. The viscoelastic properties of HDPE/clay nanocomposite foams were well described by the model. The viscoplastic model which can be applied after yielding will be studied in the future work.

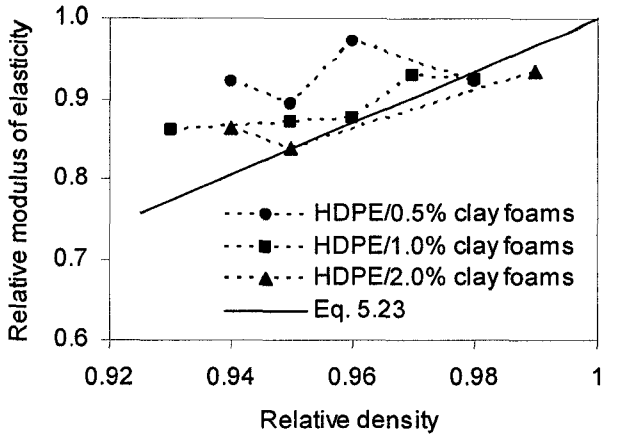

(a)

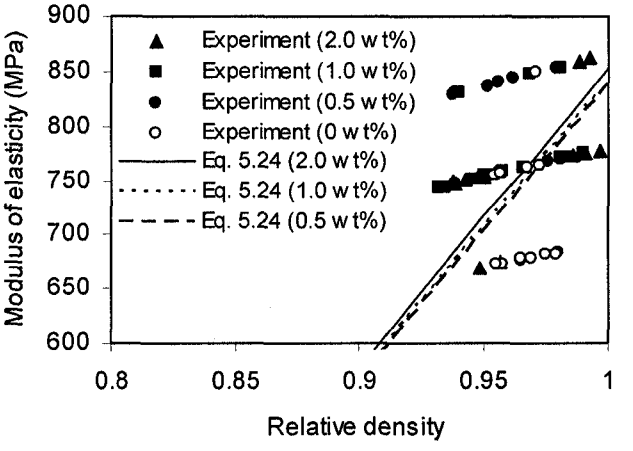

(b)

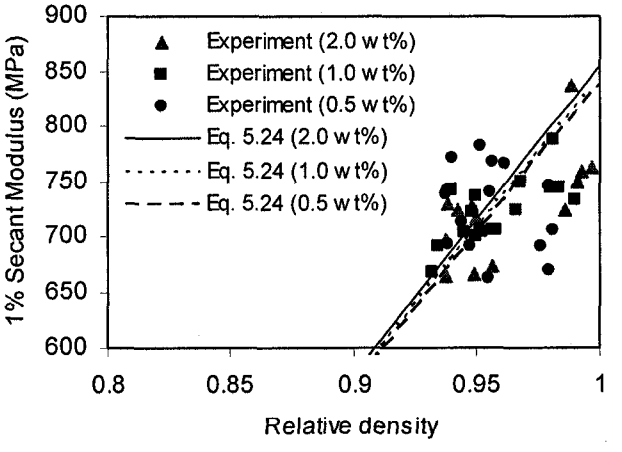

(c)

Figure 5.19 Comparison of the theoretical prediction for tensile elastic modulus of HDPE/clay nanocomposite foams with experimental results: (a) relative elastic modulus, (b) elastic modulus, (c) 1% secant modulus.

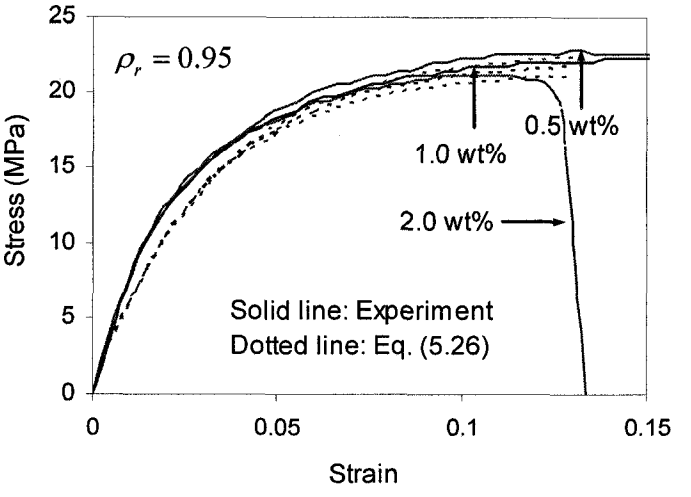

(a)

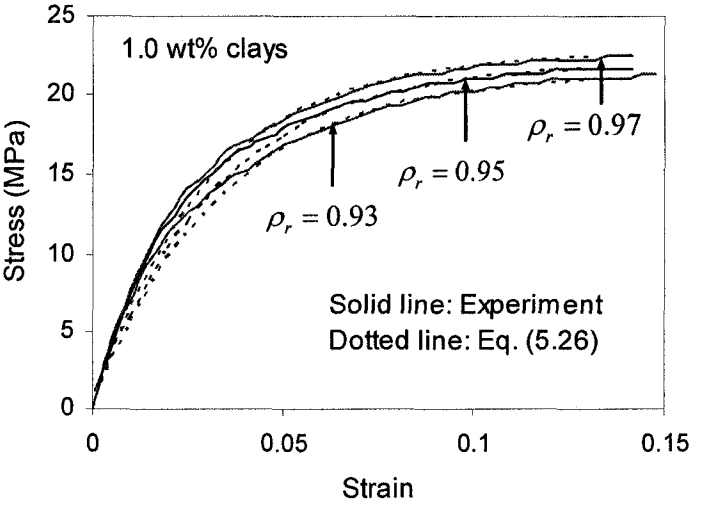

(b)

Figure 5.20 Tensile elastic behavior of HDPE/clay nanocomposite foams depending on: (a) the clay contents and (b) the relative densities.

5.5 Conclusion

The effects of the nanoclay and foaming conditions on the foam morphology and tensile mechanical properties of polymer/clay nanocomposite foams were studied. The microcellular HDPE/clay nanocomposite foams were prepared by batch foaming process with 0.5, 1.0, and 2.0 wt% nanoclay loadings. Also, uniaxial tensile tests were performed with the foams. The effect of clay contents, and foaming conditions on the cell morphologies such as cell size and volume expansion ratio, and on the mechanical properties such as elastic modulus, tensile strength, and elongation at break were investigated. The nanoclays in both nanocomposites and nanocomposite foams played a role in improving the mechanical properties such as elastic modulus and tensile strength at yield. Compared to the pure HDPE foams, HDPE/clay foams showed better tensile properties. At 0.5 wt% nanonclay loading, the mechanical properties of both nanocomposites and nanocomposite foams were improved most. A constitutive model for characterizing the tensile elastic behavior of HDPE/clay nanocomposite foams was developed using micromechanics theory and compared with the experimental results. Within high relative density region, the theoretical model could predict the uniaxial tensile elastic behavior of HDPE/clay nanocomposite foams.

Chapter 6

Effect of Crystallinity and Strain Rate on the Cell Morphology and Mechanical Properties of HDPE/Clay Nanocomposite Foams[1]

6.1 Introduction

Since the crystalline structures play a role as an obstacle on the foaming of semicrystalline polymers the expansion ratio of foams is decreased with increasing crystallinity in the semicrystalline polymer [Doroudiani et al, 1996, Rachtanapun et al. 2003, Doroudiani et al, 1998]. The influence of nanoclay on the crystallinity was studied [Min et al. 2006, Mehrabzadeh and Kamal 2004]: The crystallinity of HDPE/clay composites blown films was decreased as Cloisite 15A content increased from 0.5 to 2.0 wt%, however, when 5.0 wt% Cloisite 15A was used, the crystallinity was not affected [Mehrabzadeh and Kamal 2004]. Also, the crystallinity was decreased continuously up to 10 wt% loadings of graphite in HDPE [Zheng et al. 2004]. Some studies for the effect of crystallinity on the mechanical properties have been performed using HDPE foams or HDPE/clay nanocomposites [Doroudiani et al, 1996, Min et al. 2006, Doyle 2000].

The influence of strain rate on the viscoplastic response of isotactic polypropylene (iPP) was studied by Drozdov and Christiansen [Drozdov and Christiansen 2003]. It was demonstrated that the elastic modulus and viscoplastic flow were monotonically increased with Hencky strain rate. The tensile flow stress of polymer showed almost linear relation with log scale of strain rate [Sarva et al. 2007], and the ultimate stress of glass–epoxy composite increased monotonically with strain rate [Fereshteh-Saniee et al. 2005]. In the modeling for the effect of strain rate on the elastic modulus of polymer, log scale of the

[1]Reproduced from: C. Jo and H.E. Naguib, Modeling the Effect of Strain Rate on the Mechanical Properties of HDPE/Clay Nanocomposite Foams, *Polymers and Polymer Composites*, submitted 2008.

strain rate was used [Zhou and Mallick 2002, Drozdov and Christiansen 2004, Drozdov and Christiansen C. 2007], where the increase in the elastic modulus of semicrystalline polymer with strain rate is explained by using the effect of material viscosity [Drozdov and Christiansen 2004]. The nominal-stress increases with strain rate but reached a constant value as strain rate increased [Briatico-Vangosa and Funk 2000]. Also, It was reported that at high strain rates the semicrystalline polymer behave as elastic materials, representing little dependence on the strain rate.

In this chapter, HDPE/clay nanocomposite foam was used to investigate the effect of crystallinity and strain rate on the mechanical properties and cell morphologies of the foams. Also, the effects of processing conditions and nanoclay loadings on the foam morphology and mechanical properties of the foams were investigated. High density polyethylene (HDPE)/clay nanocomposites with various crystallinities were prepared by altering the cooling rate of the polymer melt, where the nanoclay loadings of 0.5, 1.0, and 2.0 wt% were used. Then, microcellular foams were manufactured by a batch foaming process. The nanocomposites were characterized by means of transmission electron microscope (TEM) to examine the clay structures in the polymer and also, crystallinity was measured by differential scanning calorimeter (DSC) experiment. Foam morphologies were studied by using scanning electron microscope (SEM). Tensile mechanical properties were studied by carrying out the uniaxial tensile test of nanocomposites and its foams. The influence of crystallinity and strain rate on the Young's modulus, tensile strength, and toughness were investigated. Also, the effect of crystallinity and strain rate on the mechanical properties was considered in the constitutive model, and the models were verified by experiments.

6.2 Experimental

6.2.1 Materials

The same materials as used in section 5.3.1 are used in this experiment.

6.2.2 Preparation of HDPE/clay nanocomposites

The same procedures described in section 5.3.2 are used for HDPE/clay nanocomposites. However, three different cooling rates of the compression-molded samples were used to induce differing crystallinities in the samples. For a fast cooling rate, samples were quenched in cold water, and for a medium cooling rate, they were cooled in air to room temperature. Finally, the samples were cooled slowly on a hot pressing plate to induce a higher crystallinity. The observed cooling rates on a hot plate are 2.0°C/min up to 7 min and 1.1°C/min up to 16 min, and then cooled at the rate of 0.83°C/min until the melting temperature of the sample is reached.

6.2.3 Microcellular foaming

A batch microcellular foaming process was utilized for foaming the HDPE/clay nanocomposite samples. First, the compression-molded samples were saturated in a pressurized CO_2 chamber at 5.9 MPa, at room temperature, for 8 days. Then, the pressure was released rapidly to supersaturate samples with CO_2. Next, the samples were immersed in a hot glycerin bath for foaming, where the foaming temperature was 130°C. In order to control the expansion ratio, variable foaming times (20, 30, 40, and 50s) were used. The foamed samples were immediately quenched in cold water to prevent cell deterioration.

6.2.4 Sample characterization and mechanical testing

The measurement of foam density and TEM experiments are the same in section 5.3.4. The crystallinity of the HDPE/clay nanocomposites is investigated by utilizing a differential scanning calorimeter (DSC, 2910 TA Instruments Co.) at a heating rate of 10°C/min from 20°C to 200°C under a nitrogen environment. Sample weights of 4 to 6 mg are used. The crystallinity is calculated from the specific heat required for the melting of the sample by integrating the corresponding peak and dividing this value by the heat of fusion (293 J/g) for the pure crystalline phase of HDPE [Min et al. 2006].

The foam morphology of HDPE/clay nanocomposite foams was characterized by utilizing a scanning electron microscope (SEM). The samples were cooled in liquid nitrogen and fractured to produce a clean and intact surface with minimum plastic deformation. They

were then platinum-coated by using a sputter coater (SEM Coating Unit PS3) for enhanced conductivity. A JOEL scanning electron microscope (JSM-6060) was then operated at 20 kV, and images were acquired from several locations on each sample.

The uniaxial tensile mechanical tests are performed as in section 5.3.4. However, three different crosshead speeds (50, 5, and 1 mm/min) were used in this experiment to obtain different strain rates.

6.3 Results and Discussion

6.3.1 Crystallinity

The influence of cooling rate and clay contents on the density of HDPE/clay nanocomposites is shown in Table 6.1.

Table 6.1 Effect of cooling rate on the density of HDPE/clay nanocomposites (unit: g/cm^3).

Clay content / Cooling type	0 wt%	0.5 wt%	1.0 wt%	2.0 wt%
Water cooling	0.942	0.945	0.945	0.947
Air cooling	0.962	0.962	0.964	0.965
Hot plate cooling	0.968	0.969	0.970	0.974

The increase of density with decreasing the cooling rate is due to the higher crystallinity in HDPE. As the cooling rate is decreased more crystal structures are formed in HDPE, which results in an increase in density because crystals are heavier than amorphous portions. The density also increases gradually in proportion to the nanoclay content because the density of clay is larger than that of HDPE. Since the polymer density is related to the volume fraction of crystals (V_c), it is given by

$$\rho_0 = V_c\rho_c + (1 - V_c)\rho_a \ , \tag{6.1}$$

where ρ_c and ρ_a are the density of crystal structure and amorphous structure, respectively. For polyethylene, ρ_c and ρ_a are 1.0 g/cm^3 and 0.854 g/cm^3, respectively [Mills 2005]. When clay particles are included in the polymer, the density of the polymer/clay nanocomposites is transformed into the following equation:

$$\rho = V_p\rho_p + (1-V_p)\rho_a + (1-V_{pi})V_c(\rho_c - \rho_a) \ , \tag{6.2}$$

where V_p is the volume fraction of clay particles and is calculated from the weight fraction of the clay particles (w_p) by

$$V_p = \left[1 + \frac{\rho_p}{\rho_m}\left(\frac{1}{w_p} - 1\right)\right]^{-1} \ . \tag{6.3}$$

In Eq. (6.3), ρ_p is the density of clay particles and ρ_m is the density of polymer matrix. The density of Cloisite 20A is 1.77 g/cm^3. When all of the clay particles are intercalated, the volume fraction of the intercalated clay clusters in the nanocomposites is obtained by an intercalated model [Jo et al. 2006]

$$V_{pi} = V_p\left(1 + \frac{n_p - 1}{n_p}\frac{d_m}{d_p}\right), \tag{6.4}$$

where n_p is the number of clay layers in each intercalated clay cluster, and d_p and d_m denote the clay layer thickness and the spacing between clays, respectively. The intercalated clay clusters in HDPE/clay nanocomposites are shown in Fig. 6.1. The thickness of the intercalated clay clusters decrease as clay content increases, which is attributed to the decrease of interlayer spacing in the clay clusters. In Eq. (6.4), n_p is assumed as five and d_m/d_p = 5, 4, and 3 were used for 0.5, 1.0 and 2.0 wt% clay loadings, respectively. The magnitude of d_m/d_p is determined from experiments, and the background for the determination of these values for HDPE/clay nanocomposites was explained in the previous study [Jo and Naguib 2007].

From the data in Table 6.1, the percentage crystallinity of HDPE/clay nanocomposites can be estimated as a function of clay content and density of nanocomposites, in which the crystallinity is considered to be linearly proportional to the volume fraction of crystals. The

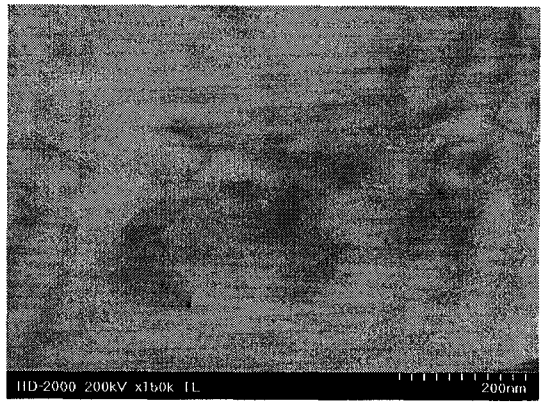

(a)

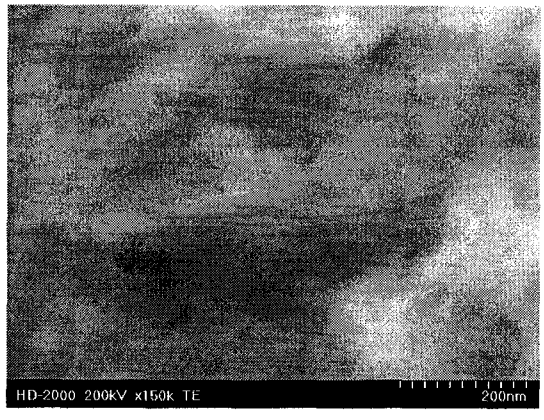

(b)

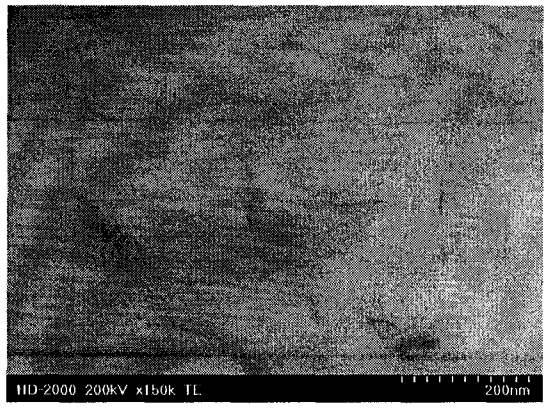

(c)

Figure 6.1 Transmission electron micrographs of HDPE/clay nanocomposites: (a) 0.5 wt% clay; (b) 1.0 wt% clay; (c) 2.0 wt% clay.

Table 6.2 Percent crystallinity of HDPE/clay nanocomposites.

Clay content / Cooling type	0 wt%	0.5 wt%	1.0 wt%	2.0 wt%
Water cooling	60.27	65.02	65.49	65.74
Air cooling	70.04	71.28	72.50	72.28
Hot plate cooling	74.72	76.04	77.33	77.56

effect of the cooling rate and clay contents on the crystallinity of HDPE/clay nanocomposites is shown in Table 6.2. By decreasing the cooling rate, the crystallinity increased. However, there was no significant change in the crystallinity between 0.5 and 2.0 wt% clay loadings. It looks dissimilar from other studies [Min et al. 2006, Zheng et al. 2004, Lee YH et al. 2005] where the crystallinity was decreased overall as the clay content increased. This difference is due to the fact that the clay contents are not high enough, and also, the clays were not exfoliated in the present experiment. In the case of the fast cooling rate (water cooling) the crystallinity shows a distinct increase by adding clay. This increase could be the result of the effect of clay or the coupling agent (PE-g-MAn). In this study, the effect of the coupling agent on the crystallinity was not measured. However, Lee et al's result [Lee YH et al. 2005] showed that the crystallinity of HDPE increased by adding only PE-g-MAn and actually began to decrease by incorporating clays. The rate of decrease depends upon the type of compatibilizer or type of clay used. Thus, it can be accounted that the increase of crystallinity in Table 6.2 is caused by the coupling agent. If the influence of interference by clays on the crystalline process is not significant, the crystallinity of polymer/clay nanocomposites can be defined as the volume fraction of crystals in the nanocomposites as $\chi_c = C(1-V_{pi})V_c$. The expression for $(1-V_{pi})$ is derived from Eq. (6.2). Then, the crystallinity is expressed as function of the volume fraction of clay particles and the density of nanocomposites as

$$\chi_c = C\frac{(\rho-\rho_a)-V_p(\rho_p-\rho_a)}{(\rho_c-\rho_a)}, \tag{6.5}$$

The factor C in Eq. (6.5) is for the effect of the coupling agent on the crystallinity, and the value of ρ can be obtained by Eq. (6.2). The crystallinity predicted by Eq. (6.5) shows

gradual decrease by increasing the clay content. The factor C for the fast cooling case (water cooling) was proved as 1.1, while C has 1.0 for the other two cooling rates. The effect of the coupling agent on the crystallinity with various cooling rates will be studied in the future.

6.3.2 Foam morphologies

The effect of crystallinity on the foaming degree is shown in Fig. 6.2. In this study, the samples obtained by using 20 s foaming time were selected on plotting figures as the highest volume expansion ratios were produced at 20 s foaming time. It was demonstrated in the figure that the highest volume expansion ratio was obtained with the air cooled samples, which means that proper crystallinity is one of the parameters for high foaming degree. Also the foaming was improved by incorporating the clays, where lower relative density was obtained at high clay contents. The clay particles contributed more to the foaming of HDPEs at lower crystallinity. This is inferred from the fact that more crystalline structures in high crystalline materials acted as an obstacle to the solubility and diffusivity of the blowing agent [Doroudiani et al, 1996], and consequently diminishes the favorable effect of clay particles on the foaming.

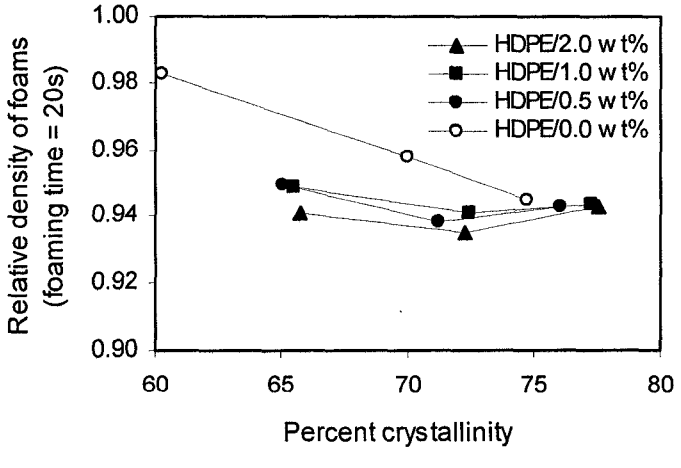

Figure 6.2 Relative density of HDPE/clay nanocomposite foams.

When pure HDPE was foamed the foaming degree was increased as crystallinity increased. This is different from the anticipated results from the references [Doroudiani et al, 1996, Rachtanapun et al. 2003, Doroudiani et al, 1998] that the degree of foaming is decreased as crystallinity increases.

The microstructure of HDPE/clay nanocomposite foams are shown in Fig. 6.3. The foam samples used for scanning electron micrographs were made at 20s of foaming time and have similar volume expansion ratios ($\approx$ 1.06). As shown in the figure, the cell sizes range from less than 1 μm to a few μm in diameters. However, there is a big difference in cell distribution between pure HDPE foams and HDPE/clay nanocomposite foams. Without clays, cells are distributed locally forming band shapes, while cells in nanocomposite foams are created through the whole polymer matrix. This phenomenon demonstrates that clay particles play a role as a nucleation agent during the foaming process. The effect of crystallinity on the cell size is clear in HDPE foams: as the crystallinity increases the cell size decreases (Figs. 6.3(a), 6.3(b), 6.3(c)). On the other hand, in the case of HDPE/clay nanocomposite foams, the variation of cell size is not significant as crystallinity increased. However, as crystallinity decreases, cell size becomes more uniform and cells are distributed more evenly.

The approximate sizes of cell diameter are obtained from SEM micrographs as plotted in Fig. 6.4(a). It is shown from the figure that the cell size decreased very slightly as clay content and crystallinity increase. However, the effect of crystallinity diminishes in high clay content samples. Cell population density of the foams can be measured by using SEM images. However, it was estimated by the following equation as the cell size and the cell distribution are not uniform in the figure:

$$N = \left(\frac{1}{\rho_r} - 1\right)\frac{6\times10^{12}}{\pi D^3} \quad (\text{cells/cm}^3). \tag{6.6}$$

In Eq. (6.6), D is the cell diameter (μm) and ρ_r is the relative density of foams. Also, cells are assumed to have spherical shape and to have uniform size at each sample. As shown in Fig. 6.4(b), cell density is proportional to the crystallinity and clay content. However, the influence of crystallinity on the cell density was decreased by increasing the clay contents. The increase of cell density means that the cell nucleation density increased with an increase

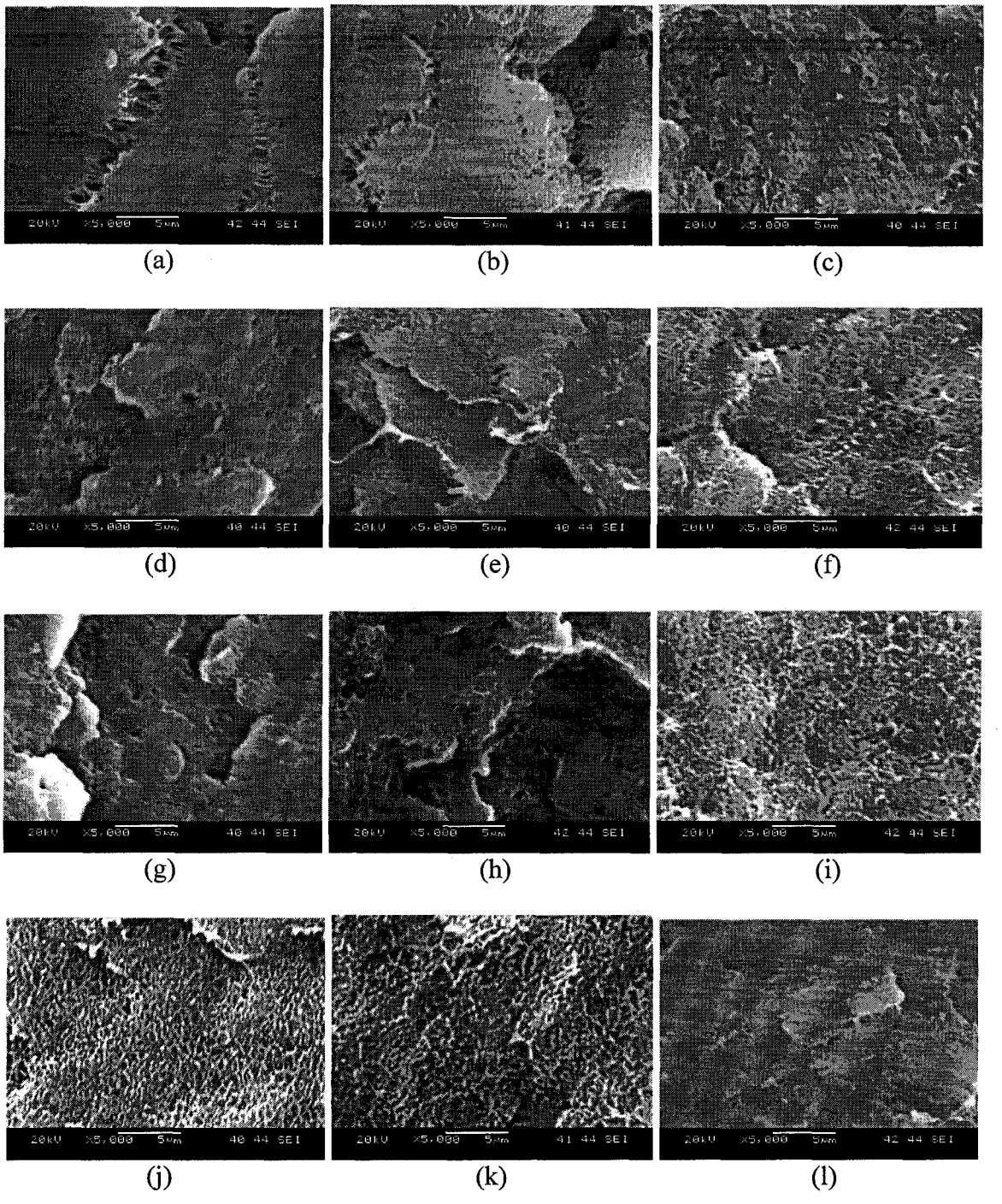

Figure 6.3 Scanning electron micrographs of HDPE/clay nanocomposite foams (×5000): (a) HDPE/0.0 wt% (water); (b) HDPE/0.0 wt% (air); (c) HDPE/0.0 wt% (hot plate); (d) HDPE/0.5 wt% (water); (e) HDPE/0.5 wt% (air); (f) HDPE/0.5 wt% (hot plate); (g) HDPE/1.0 wt% (water); (h) HDPE/1.0 wt% (air); (i) HDPE/1.0 wt% (hot plate); (j) HDPE/2.0 wt% (water); (k) HDPE/2.0 wt% (air); (l) HDPE/2.0 wt% (hot plate).

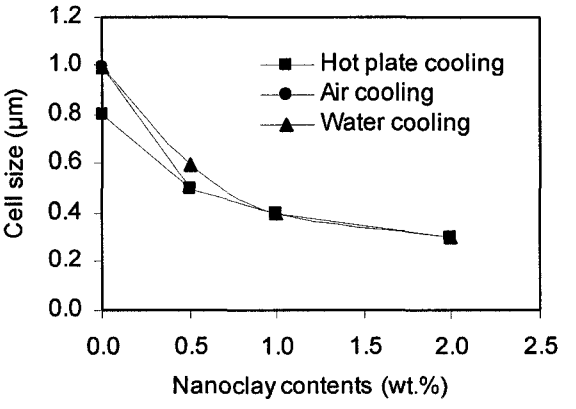

(a)

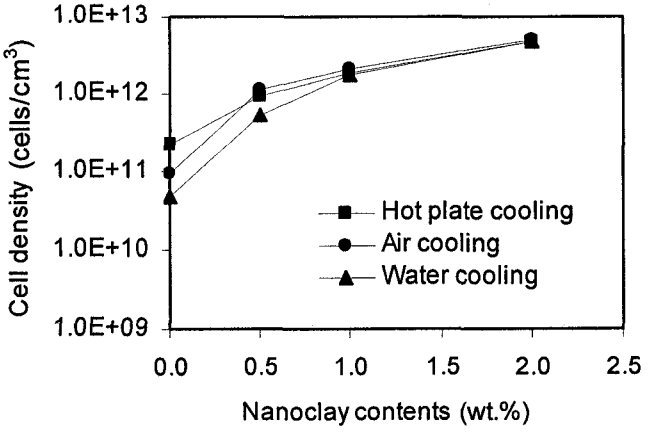

(b)

Figure 6.4 Cell sizes and cell densities as function of clay content and crystallinity (foaming time = 20s): (a) cell sizes from SEM images (b) estimated cell densities by Eq. (6.6).

in the clay content. From these results, it can be concluded that the morphology of HDPE/clay nanocomposite foams can be easily controlled at low crystalline state.

6.3.3 Mechanical properties and constitutive modeling

The effect of crystallinity on the tensile behavior of HDPE/clay nanocomposite foams is plotted in Fig. 6.5. The Young's modulus and tensile strength of the foams were increased by increasing the crystallinity. Crystallinity is measured with solid nanocomposite samples prior to foaming. So, the effect of crystallinity on the Young's modulus was modeled for HDPE/clay nanocomposites. The change of Young's modulus of HDPE/clay nanocomposites is plotted as a function of crystallinity in Fig. 6.6. For all cases of clay loadings, the Young's moduli increase as crystallinity increases. However, the rate of increase is reduced at high crystallinity region. In the previous study [Jo et al. 2006, Jo and Naguib 2007], some deteriorating effect of clays on the modulus was detected after 1.0 wt% clay loadings at low crystalline state. However, when crystallinity is over 70%, the maximum Young's moduli were obtained at high clay loadings (2.0 wt%). It can be deduced from this phenomenon that the effect of clay loadings on the Young's modulus of HDPE/clay nanocomposites is maximized at a high crystalline state of the nanocomposites, and vice versa. This is regarded as a result of that the augmenting effect by crystalline structures surpasses the decreasing effect by agglomeration of clay particles.

As represented in Fig. 6.6(a) the Young's moduli of HDPE/clay nanocomposites at each clay loading show similar trends. This trend was compared with that of pure HDPE in Fig. 6.6(b), and it was proved that they are similar. This provides a basis that the trend line of HDPE can be used for the modeling of the trend of HDPE/clay nanocomposites. If the increase of the Young's modulus of HDPE is represented as a power form of crystallinity, it can be expressed as

$$E_m = A\chi_c^{\ B} \tag{6.7}$$

In Eq. (6.7), the parameters A and B for HDPE are determined by experiments. From the curve in Fig. 6.6(b), the values of A and B are obtained as 4.585 and 1.236, respectively. Since the trend of the modulus of HDPE/clay nanocomposites has similar form as that of HDPE, the Young's modulus of the nanocomposites can be obtained from that of HDPE.

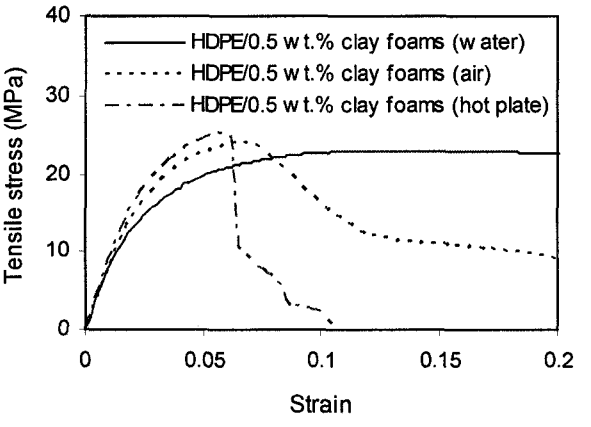

(a)

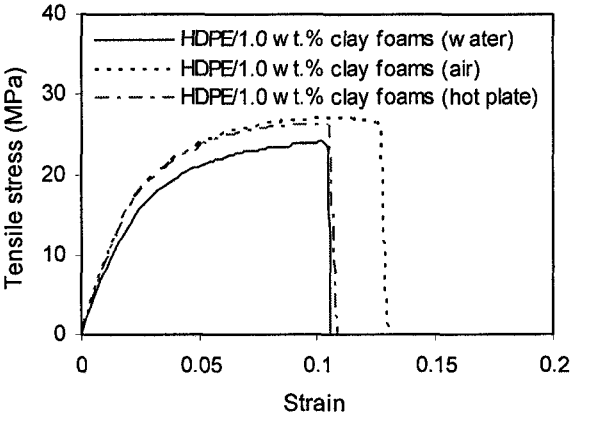

(b)

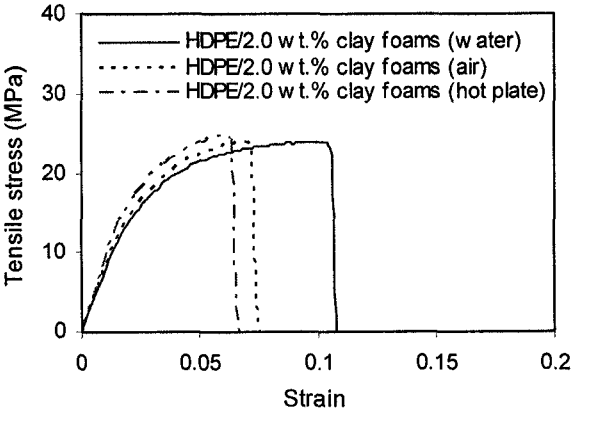

(c)

Figure 6.5 Tensile behavior of HDPE/clay nanocomposite foams (relative density = 0.95) with the clay contents of (a) 0.5 wt%, (b) 1.0 wt%, and (c) 2.0 wt%.

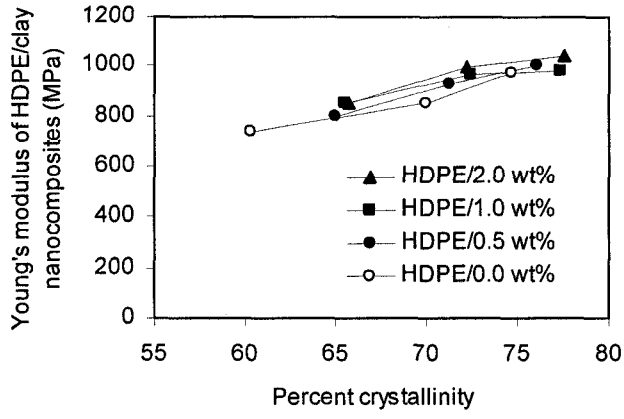

(a)

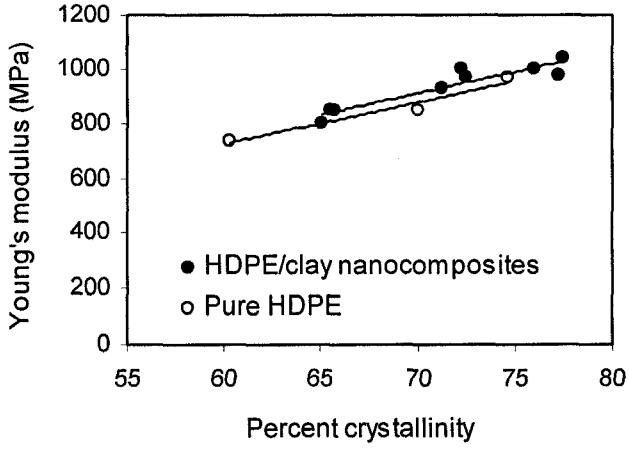

(b)

Figure 6.6 Young's modulus of HDPE/clay nanocomposites: (a) variations depending on the crystallinity; (b) comparison of the trends.

In the previous study [Jo and Naguib 2007], the Young's modulus of HDPE/clay nanocomposites was proposed as $\bar{E} = E_m' \left\{1 - v_{pi} + 3v_{pi}\left[E_p - v_{pi}\left(E_p - E_m'\right)\right]\right/ 8E_p\}^{-1}$ without considering the crystallinity. This equation can be modified as the following form by incorporating the altering crystallinity:

$$\bar{E} = C_2 A \chi_c^{\ B} \left\{1 - v_{pi} + \frac{3v_{pi}}{8E_p}\left[E_p - v_{pi}\left(E_p - C_2 A \chi_c^{\ B}\right)\right]\right\}^{-1}, \tag{6.8}$$

where the parameter C_2 is the effect of coupling agent on the Young's modulus. When PE-g-MAn was added in HDPE as a coupling agent the Young's modulus increased by 4% compared to the pure HDPE [Gopakumar et al. 2002]. Thus, in this study, C_2 = 1.04 was used for HDPE/clay nanocomposites.

The Young's modulus of HDPE/clay nanocomposites by Eq. (6.8) was compared with experiments in Fig. 6.7. As shown in the figure the points by Eq. (6.8) form a nearly straight line to all clay contents, which means that the effect of clay variation on the modulus is small.

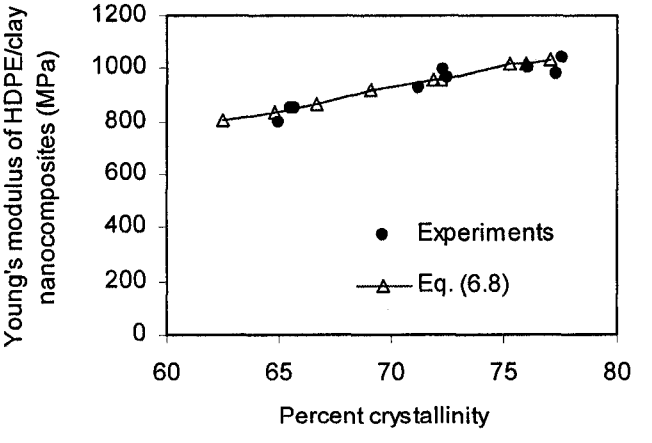

Figure 6.7 Comparison of the Young's modulus of HDPE/clay nanocomposites with theoretical model.

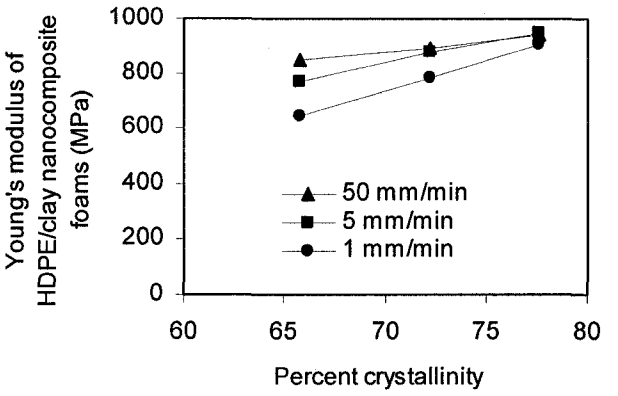

(a)

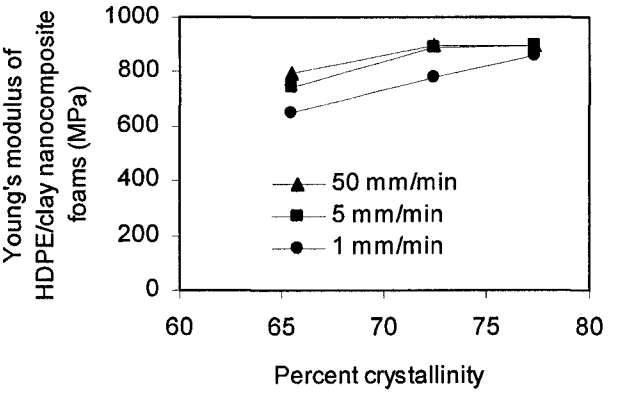

(b)

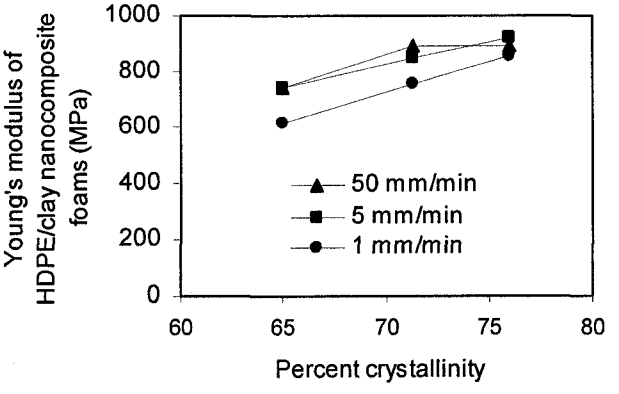

(c)

Figure 6.8 Effect of crystallinity on the Young's modulus of HDPE/clay nanocomposite foams (relative density = 0.95): (a) clay content = 2.0 wt%; (b) clay content = 1.0 wt%; (c) clay content = 0.5 wt%.

Fig. 6.8 shows the Young's modulus of HDPE/clay nanocomposite foams depicting the effect of crystiallinity and strain rate. For the plot of Fig. 6.8, the same relative density (= 0.95) of foam samples was used. Similarly to the unfoamed samples, the Young's modulus of the nanocomposite foams increased with crystallinity. However, at high strain rate, the rate of increase of the modulus was blunted as crystallinity increases.

The degree of nonlinearity in the tensile behaviour of polymer is also affected by strain rate and temperature as well as material nonlinearity. In this study, the effect of strain rate on the Young's modulus of HDPE/clay nanocomposite foams was studied. However, the effect of temperature is not considered in the model, i.e. only room temperature was used. The inelastic strain was expressed with compliance function, stress, and strain [Zhou and Mallick 2002]. If the compliance is substituted by a stiffness function (K) the strain has the following form:

$$\varepsilon_i = \frac{\sigma}{K(\dot{\varepsilon})\varepsilon^{-m}} \tag{6.9}$$

where the stiffness is a function of the strain rate. The strain exponent m represents strain-hardening or strain-softening. The state, m =1 means that polymer has a strain neutral behavior [Zhou and Mallick 2002]. This says the elastic modulus is not varies with strain. The viscoelastic model explained in the following paragraph has the strain neutral characteristic as strain increases. To incorporate the effect of strain rate into Eq. (6.8), Young's modulus is induced from Eq. (6.9). Since the Young's modulus depends on the strain rate the parameter ε in Eq. (6.9) is replaced by strain rate for Young's modulus. Then, the Young's modulus is expressed as

$$E = K(\dot{\varepsilon})\dot{\varepsilon}^{-m} \tag{6.10}$$

The Young's modulus of HDPE/clay nanocomposite foams versus the strain rate of a logarithmic scale is plotted in Fig. 6.9. The modulus increased with increasing the strain rate, but the rate of increase is blunted as the strain rate increases. Similar tendency in the variation of the initial elastic modulus was reported in Drozdov and Christiansen's work [Drozdov and Christiansen 2004]. Also, the influence of strain rate diminishes as crystallinity increases (from Fig. 6.9(a) to 6.9(c)). This phenomenon can be materialized by adding a parameter χ_c in the function of K:

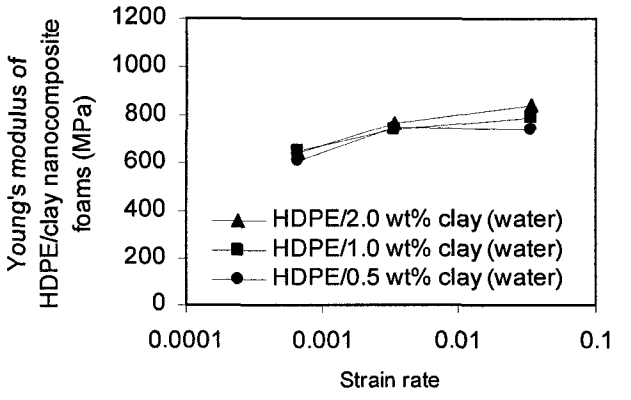

(a)

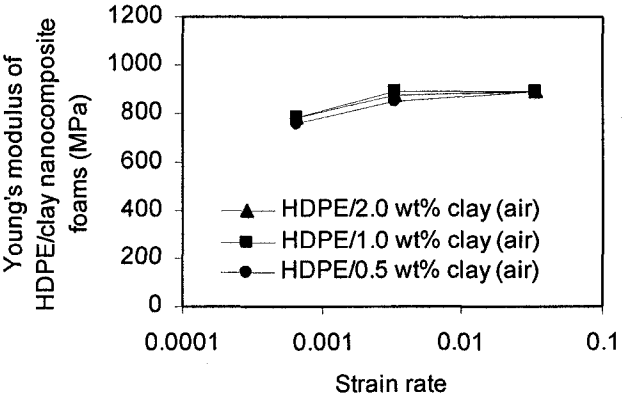

(b)

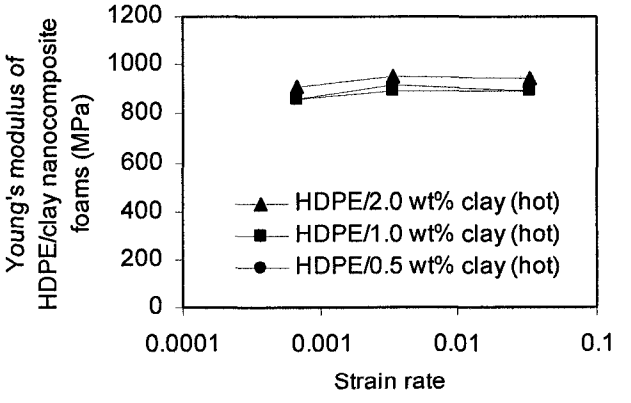

(c)

Figure 6.9 Effect of strain rate on the Young's modulus of HDPE/clay nanocomposite foams (relative density = 0.95): (a) water cooling; (b) air cooling; (c) hot plate cooling.

$$E = \frac{K(\dot{\varepsilon}, \chi_c)}{\dot{\varepsilon}^m} \tag{6.11}$$

From Fig.6.9, it was found that the variation of the Young's modulus can be represented by a logarithmic function of the strain rate. Also, since the crystallinity gives a detrimental influence on the favorable effect of the strain rate, an inverse relation to the crystallinity can be used for the modeling of the Young's modulus, which is expressed as $1/\dot{\varepsilon}^m$ in Eq. (6.11). Thus, the following formula is proposed for the compounding effect of the strain rate and crystallinity on the Young's modulus:

$$E = \frac{\log \dot{\varepsilon}}{\chi_c{}^{\alpha} \dot{\varepsilon}} + 1 \tag{6.12}$$

where $m = 1$ was used. Parameter α represents the degree of the influence of crystallinity on the strain rate effect, which will be determined by experiments. In Eq. (6.12), the constant one was introduced so that it can be applied to the previous step (Eq. (6.8)) directly. In Eq. (6.8), the effect of nanoclays and crystallinity on the Young's modulus was modeled on the basis of standard strain rate (50 mm/min test speed). To compare the Eq. (6.12) with experiments, the Young's modulus of the foams was normalized based on the strain rate comes from 50 mm/min test speed. Fig. 6.10 shows the normalized Young's modulus of the foams. The Young's modulus plotted by Eq. (12) is compared with the experiemental data in Fig. 6.10. If the effect of nanoclays on the Young's modulus is assumed not to be significant, α is determined as 2.45 from the experiemental curves. In general, they show good agreement except the low strain rate case at high crystalline state. Therefore, by incorporating the effect of the strain rate, the Young's modulus of HDPE/clay nanocomposite foams is yielded as

$$\begin{aligned} \bar{E} = 1.04 A \chi_c{}^{B} & \left\{ 1 - v_{pi} + \frac{3 v_{pi}}{8 E_p} \left[E_p - v_{pi} \left(E_p - 1.04 A \chi_c{}^{B} \right) \right] \right\}^{-1} \\ & \times \left(\frac{\log \dot{\varepsilon}}{\chi_c{}^{\alpha} \dot{\varepsilon}} + 1 \right) \left[1 - (1 - \rho_r) \frac{3(1-\nu)}{2(1-2\nu)} \right] \end{aligned} \tag{6.13}$$

In Eq. (6.13) the influence of relative density after foaming was also incorporated by previous work [Jo and Naguib 2007]. Fig. 6.11 shows the comparison of Eq. (6.13) with experimental data in the case of 0.5 wt% clay content. The relative density of foams was

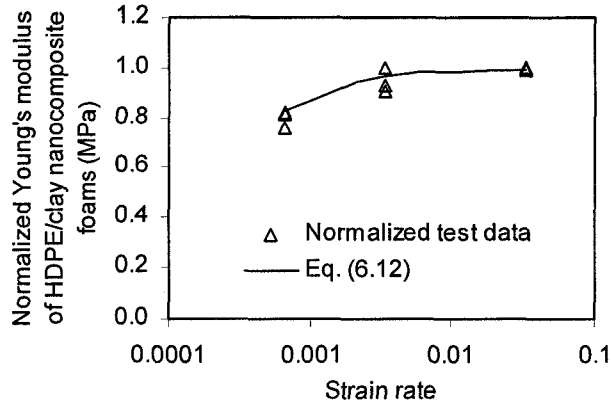

(a)

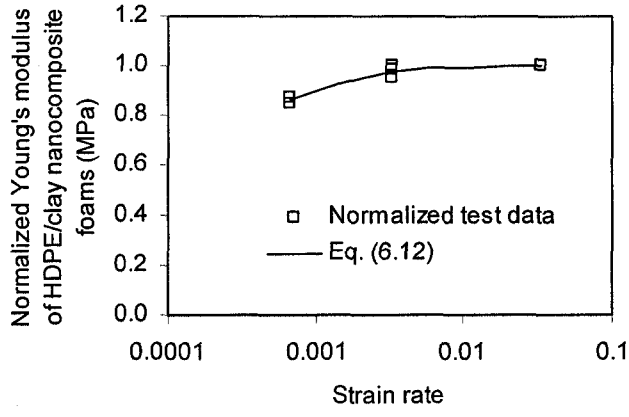

(b)

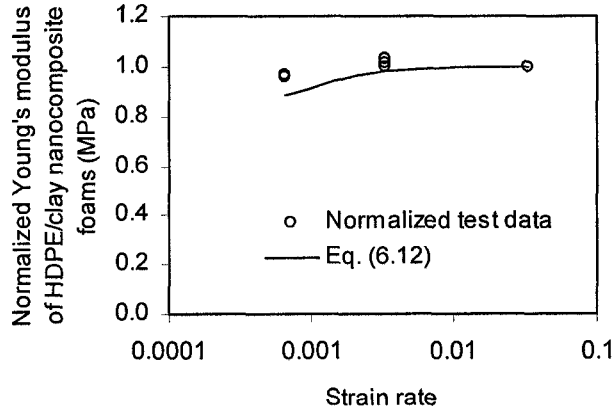

(c)

Figure 6.10 Comparison of normalized Young's modulus of foams with model: (a) water cooling; (b) air cooling; (c) hot plate cooling.

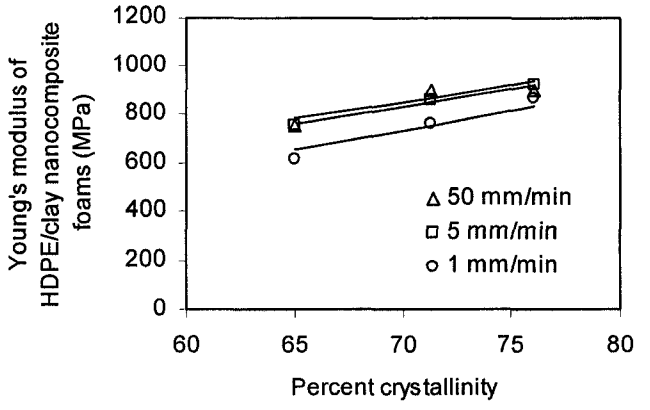

(a)

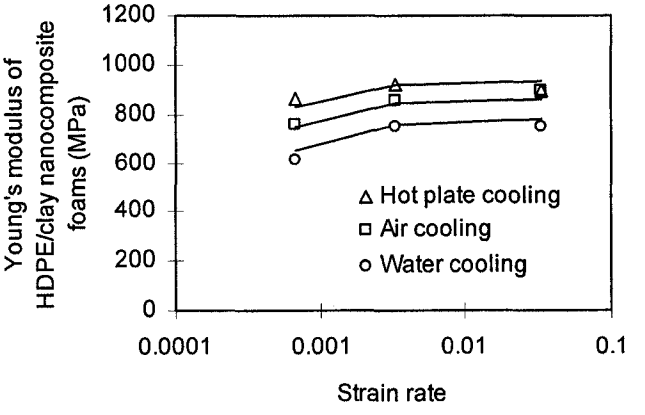

(b)

Figure 6.11 Comparison of Young's modulus by model (Eq. (6.13), solid line) with experiments (points): (a) depending on the percent crystallinity; (b) depending on the strain rate.

0.95 for all samples. The model in Eq. (6.13) shows similar tendency with experimental results. The Young's modulus by Eq. (6.13) increases with increasing the crystallinity and strain rate. However, the increase rate of Young's modulus was slow down at high strain rate greater than 0.003.

The viscoelastic stress-strain behavior of polymer/clay nanocomposite foam could be described by using a Maxwell model [Jo et al. 2005]. From the constitutive equation by Maxwell model, the equivalent elastic modulus E_{eq} was obtained as

$$E_{eq} = \left.\frac{d\sigma}{d\varepsilon}\right|_{\varepsilon \to 0} = E_0, \tag{6.14}$$

which can be counted as the Young's modulus of foams. Thus, the Young's modulus expressed by Eq. (6.13) is used as E_0 in the constitutive model. By using the relation $E = d\sigma/d\varepsilon$, the elastic modulus is obtained in the Maxwell model as

$$E = E_0 \exp\left(-\frac{\varepsilon}{\tau\dot{\varepsilon}}\right) \tag{6.15}$$

For a basis of numerical analysis, the stress is expressed as a function of strain increase in this study. The relationship between stress and strain can be defined as Fig. 6.12, where the stress-strain points are selected at the middle of the each strain interval to take off the size effect of $\Delta\varepsilon$.

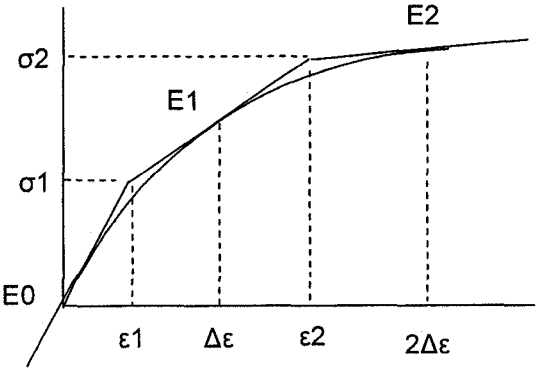

Figure 6.12 Stress-strain relation in the constitutive equation.

Then the modulus in Eq. (6.15) is expanded as

$$E_1 = E_0 \exp\left(-\frac{\Delta\varepsilon}{\tau\dot{\varepsilon}}\right),\ E_2 = E_0 \exp\left(-\frac{2\Delta\varepsilon}{\tau\dot{\varepsilon}}\right),\ E_n = E_0 \exp\left(-\frac{n\Delta\varepsilon}{\tau\dot{\varepsilon}}\right) \quad (n \geq 1) \tag{6.16}$$

and the stresses are

$$\sigma_0 = 0, \quad \sigma_1 = E_0 \frac{\Delta\varepsilon}{2}, \quad \sigma_n = \sigma_{n-1} + E_{n-1}\Delta\varepsilon \quad (n \geq 2) \tag{6.17}$$

Thus, the stress equation is

$$\sigma_n = E_0\Delta\varepsilon\left[\frac{1}{2} + \exp\left(-\frac{\Delta\varepsilon}{\tau\dot{\varepsilon}}\right) + \exp\left(-\frac{2\Delta\varepsilon}{\tau\dot{\varepsilon}}\right) + ... + \exp\left(-\frac{(n-1)\Delta\varepsilon}{\tau\dot{\varepsilon}}\right)\right] \qquad (\sigma_0 = 0,\ n \geq 1)$$

$$\varepsilon_n = \frac{2n-1}{2}\Delta\varepsilon \qquad (\varepsilon_0 = 0,\ n \geq 1) \tag{6.18}$$

where, the size of $\Delta\varepsilon$ does not affect the stress-strain curve by Eq. (6.18). Simplifying the stress equation, the following expression is yielded:

$$\sigma_n = E_0\Delta\varepsilon\left[-\frac{1}{2} + \left\{1-\exp\left(-\frac{n\Delta\varepsilon}{\tau\dot{\varepsilon}}\right)\right\}\left\{1-\exp\left(-\frac{\Delta\varepsilon}{\tau\dot{\varepsilon}}\right)\right\}^{-1}\right], \tag{6.19}$$

where the effects of crystallinity, strain rate, and clay content are considered in the modulus equation E_0. The tensile stress-strain data were compared with the prediction by Eq. (6.19) in Fig. 6.13, where the relative density is 0.95 in model and experiment. As shown in the figure the proposed constitutive model describes the viscoelastic tensile behavior of HDPE/clay nanocomposite foams. In Fig. 6.13, the discrepancy between the experiments and the predictions by model are arising from the difference of the Young's modulus between the experiments and the model predictions. In the proposed constitutive model, the initial elastic part is dependent upon the magnitude of Young's modulus, and the remaining part is determined by the parameter τ . Since the relaxation time constant τ in the constitutive equation depends on the strain rate [Jo et al. 2005], it needs to be expressed as a function of the strain rate. The relaxation time constants used in Fig. 6.13 are listed in Table 6.3, and plotted in Fig. 6.14. From the figure, it was proved that the log scale of relaxation time constant is inversely proportional to the log scale of strain rate. Therefore, τ is expressed as a function of the strain rate as

$$\log\tau = p\log\dot{\varepsilon} + q \tag{6.20}$$

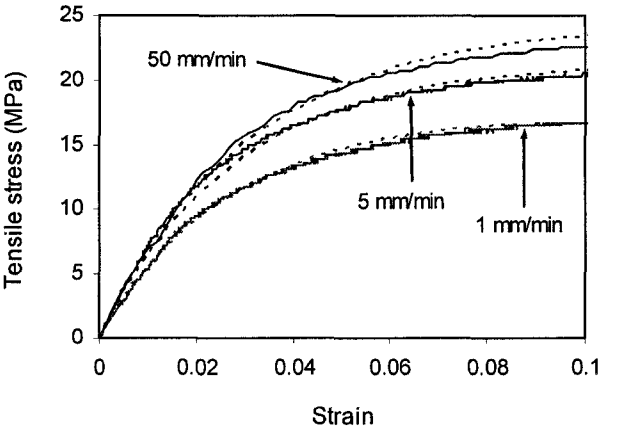

(a)

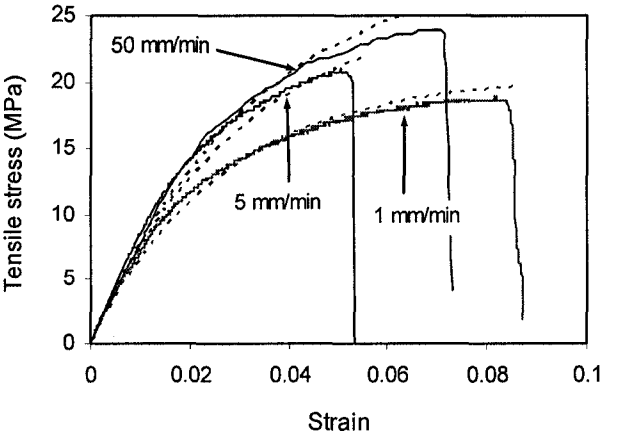

(b)

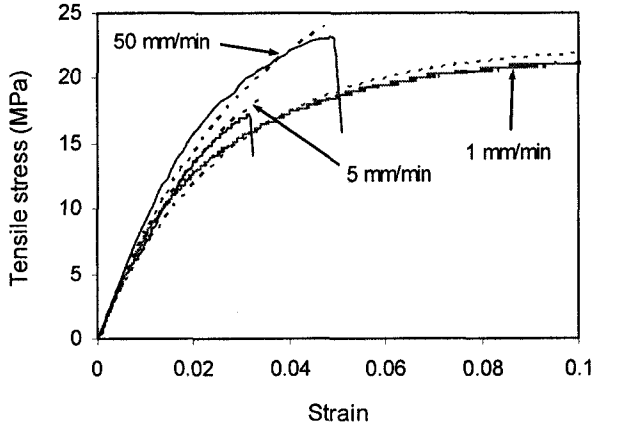

(c)

Figure 6.13 Tensile stress-strain behavior of HDPE/clay nanocomposite foams (solid line: experimental data, dotted line: Eq. (6.19)): (a) 0.5% clay content, water cooling, (b) 2.0% clay content, air cooling, (c) 1.0% clay content, hot plate cooling.

Table 6.3 Relaxation time constant τ used in Figure 6.13.

Crosshead speed (mm/min)	0.5 wt% clay content Water cooling	2.0 wt% clay content Air cooling	1.0 wt% clay content Hot plate cooling
50	0.95	1	1
5	8.5	9	8.5
1	40	40	40

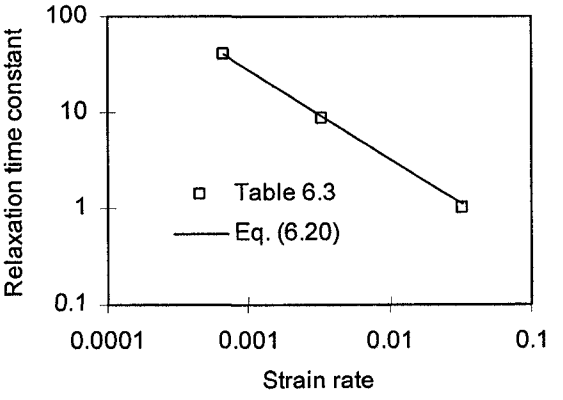

Figure 6.14 Relaxation time constant depending on the strain rate.

The parameters p and q are determined from the experimental data as -0.92 and -1.32, respectively. In Fig. 6.14, the curve by Eq. (6.20) was compared with the relaxation time constants plotted with the data in Table 6.3. Using the expression for τ the constitutive equation for HDPE/clay nanocomposite foams can be modified as

$$\sigma_n = E_0 \Delta\varepsilon \left[-\frac{1}{2} + \left\{ 1 - \exp\left(-\frac{n\Delta\varepsilon}{0.04786\dot{\varepsilon}^{0.08}} \right) \right\} \left\{ 1 - \exp\left(-\frac{\Delta\varepsilon}{0.04786\dot{\varepsilon}^{0.08}} \right) \right\}^{-1} \right] \tag{6.21}$$

The tensile strength of HDPE/clay nanocomposites increases gradually as crystallinity increases. However, a different aspect was found when the samples were foamed. As shown in Fig. 6.15(a), both nanoclay and crystallinity do not give significant influence on the tensile strength of HDPE/clay nanocomposite foams. Also, as indicated in the figure, the tensile strength of pure HDPE foams could have higher value than those of the foams, which implies that the tensile strength is deteriorated easily by adding clays when crystallinity is relatively high. It can also be said that high crystallinity gives an adverse effect on the tensile strength when HDPE/clay nanocomposite samples are foamed. The tensile strength of the foams increased with increasing the strain rate as shown in Fig. 6.15(b), where the tensile strength shows linearly proportional to the log scale of the strain rate.

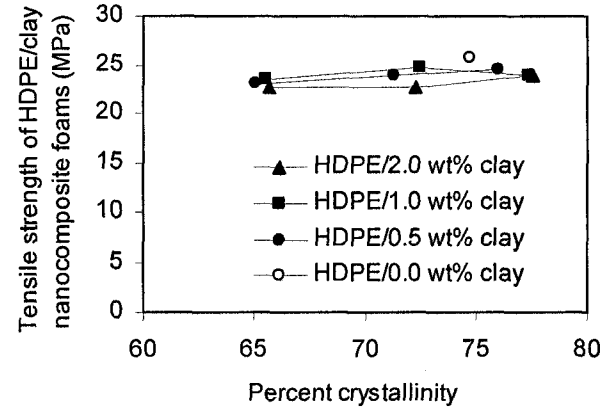

(a)

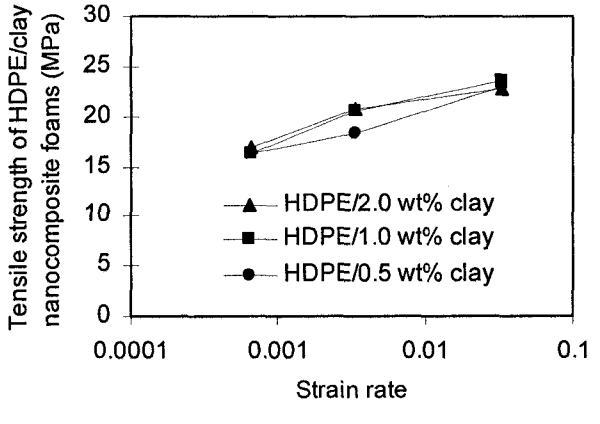

(b)

Figure 6.15 Tensile strength of HDPE/clay nanocomposite foams (relative density = 0.95) depending on: (a) the crystallinity and (b) the strain rate.

Percent elongation at yield of HDPE/clay nanocomposite foams decreased as clay content and crystallinity increased (Fig. 6.16). Also, the toughness dropped as crystallinity increases. This reduction of toughness is inferred as a result of the brittle failure in crystalline structures.

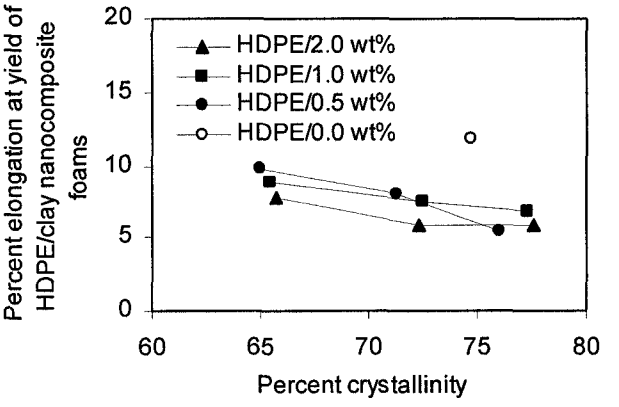

Figure 6.16 Percent elongation at yield of HDPE/clay nanocomposite foams (relative density = 0.95) as a function of crystallinity.

6.4 Conclusion

The effect of strain rate and crystallinity on the mechanical properties of HDPE/clay nanocomposite foams was investigated. HDPE/clay nanocomposites with various crystallinities were prepared with clay loadings of 0.5, 1.0, and 2.0 wt%. A batch foaming process was used to make microcellular foams. The samples were characterized by using TEM, DSC, and SEM experiments, and uniaxial tensile tests were carried out. The favorable effect of clay particles on the foaming was increased as crystallinity decrease. As crystallinity increases, the volume expansion ratio of HDPE/clay nanocomposite foams increased up to certain point of crystallinity, but began to decrease as crystallinity increases more. Cell size became more uniform and cells were distributed more evenly as crystallinity decreases. Cell density was proportional to the crystallinity. However, the influence of

crystallinity on the cell density was decreased by increasing the clay contents. The Young's modulus of HDPE/clay nanocomposite foams increased with crystallinity. However, at high strain rate, the rate of increase of the modulus was blunted as crystallinity increases. Also, the Young's modulus of the foams increased gradually with increasing the strain rate, but the rate of increase diminished as crystallinity increases. Crystallinity did not give significant influence on the tensile strength of HDPE/clay nanocomposite foams. However, the tensile strength showed linear increase to the strain rate on log scale. Percent elongation and toughness of the foams decreased as clay content and crystallinity increased. Also, a constitutive model considering the effect of strain rate and crystallinity on the mechanical behavior of the foams was proposed. The effect of strain rate and crystallinity was incorporated in the Young's modulus in the modeling. A viscoelastic model was proposed to describe the stress-strain behavior of the foams. Good agreement was demonstrated between the proposed constitutive model and the experimental results.

Chapter 7

Conclusions and Recommendations

Constitutive models for characterizing the mechanical behavior of amorphous and semi-crystalline polymer/clay nanocomposite foams were developed. For viscoelastic nonlinear stress-strain behavior of foams, constitutive equations were derived from several viscoelastic models. It was verified that the constitutive equation based on Maxwell model could be a representative among several constitutive equations obtained from other types of viscoelastic model providing that the relaxation time constant is determined properly. The proposed constitutive equation is expressed as a function of strain, strain rate, relaxation time constant, equivalent elastic modulus, volume fraction of solid contained in the cell edges, and relative density of foams.

A constitutive model for tensile behavior of PMMA/clay nanocomposite foams was developed elucidating the effect of intercalated and agglomerated nanoclays. In determining the elastic modulus of the nanocomposite foams, the reinforcing effect by intercalated clay particles and the detrimental effect by agglomerated clay particles were taken into account. The proposed model is expressed in terms of clay morphologies such as aspect ratio and clay layer spacing, foam morphologies, and material properties. The tensile stress-strain curves predicted by the constitutive model were validated by experimental results.

As a semi-crystalline polymer, HDPE/clay nanocomposite foams was manufactured by a batch foaming process and the effect of clay contents, crystallinity, and foaming conditions on the cell morphologies and mechanical properties of the foams were studied. Cell size, cell population density, volume expansion ratio, elastic modulus, tensile strength, and toughness were investigated. Intercalated clay structures were detected in the nanocomposites, and the influence of intercalated clay structures was considered in the constitutive modeling. Nanoclay loadings provided favorable condition for foaming, and contributed more to the foaming at lower crystalline state. Cell size decreased as clay content or crystallinity increased. However, as clay content increased, the influence of crystallinity on the variation of cell size was diminished. According to the tensile mechanical tests, the Young's modulus

of HDPE/clay nanocomposite foams increases with crystallinity. However, at high strain rate, the rate of increase in the modulus was blunted as crystallinity increases. Also, the Young's modulus of the foams increased gradually with increasing the strain rate, but the rate of increase diminished as crystallinity increases. The percent elongations at yield and break decreased as crystallinity increase. A constitutive model characterizing the tensile elastic behavior of HDPE/clay nanocomposite foams was developed, where the elastic modulus of the foams was developed using micromechanics and representative volume element (RVE) concept. In the model, the effect of clay contents, crystallinity and loading rate were considered. The developed constitutive models were validated by tensile experiments using HDPE/clay nanocomposite foams. Theoretical predictions by the model showed good agreement with the experimental results.

As a future study, the effect of coupling agent on the crystallinity and mechanical properties will be determined. Also, the decrease of foaming degree at long foaming time needs to be examined. Furthermore, viscoplastic characteristics can be incorporated in the constitutive model, where the yield model is defined and plastic deformations are described. Also, the influence of temperature on the mechanical properties can be considered.

References

Alexandre M, Dubois P. *Mater. Sci. Eng.* **28** 1-63 (2000)

Alexandre M, Dubois P, Sun T, Garces IM, Jerome R. *Polymer* **43**(8) 2123-32 (2002)

Arruda EM, Boyce MC, Jayachandran R. *Mech. Mater.* **19** 193-212 (1995)

Arzoumanidis GA, Liechti KM. *Mech. of Time-Dependent Materials* **7** 209–50 (2003)

Baldwin DF, Park CB, Suh NP. *Polym. Eng. Sci.* **36** 1425–35 (1996)

Baldwin DF, Suh NP. *ANTEC '92, SPE Tech. Paper* **38** 1503–7 (1992)

Bartczak Z, Argon AS, Cohen RE. *Macromol.* **25**(19) 5036-53 (1992a)

Bartczak Z, Cohen RE, Argon AS. *Macromol.* **25**(18) 4692-704 (1992b)

Bekkour K, Scrivener O. *Mechanics of Time-Dependent Materials* **2** 171–93 (1998)

Benveniste Y. *Mech. Mater.* **6**(2) 147 (1987)

Bergman JS, Chen H, Giannelis EP, Thomas MG, Coates TG. *Chem. Commun.* 2179-80 (1999)

Berthoud P, G'Sell C, Hiver J-M. *J. Phy.s D: App.l Phys.* **32** 2923-32 (1999)

Bharadwaj RK. *Macromolecules* **34** 9189-92 (2001)

Briatico-Vangosa F, Funk M. *Polym. Eng. Sci.* **40** 1553-63 (2000)

Biswas M, Ray S. *Adv. Polym. Sci.* **155** 167 (2001)

Broek D. *Elementary Engineering Fracture Mechanics* Martinus Nijhoff, Dordrecht (1986)

Brune DA, Bicerano J. *Polymer* **43** 369 (2002)

Collias DI, Baird DG, Borggreve RJM. *Polymer* **35** 3978–83 (1994)

Chen W, Lu F, Cheng M. *Polymer Testing* **21** 113–121 (2002)

Cho JW, Paul DR. *Polymer* **42**(3) 1083-94 (2001)

Cho KS, Kim SY. *Macromol. Theory Simul.* **9** 328–35 (2000)

Christensen RM. *Theory of viscoelasticity: an introduction* 2nd ed. New York, Academic Press (1982)

Deshpande VS, Fleck NA. *J. Mech. Phys. of Solids* **48** 1253-83 (2000)

Dommelen JAW, Schrauwen BAG, Breemen LCA, Govaert LE. *J. Polym. Sci. Part B: Polym. Phy.s* **42** 2983–94 (2004)

Dommelen JAW, Brekelmans WAM, Baaijens FPT. *J. Mat. Sci.* **38** 4393–405 (2003)

Dommelen JAW, Parks DM, Boyce MC, Brekelmans WAM, Baaijens FPT. *Polymer* **44** 6089–101 (2003)

Dommelen JAW, Parks DM, Boyce MC, Brekelmans WAM, Baaijens FPT. *J. Mech. Phys. Solids* **51** 519–41 (2003)

Doroudiani S, Park CB, Kortschot MT. *Polym. Eng. Sci.* **36**(21) 2645-62 (1996)

Doroudiani S, Park CB, Kortschot MT. *Polym. Eng. Sci.* **38**(7) 1205-15 (1998)

Doyle MJ. *Polym. Eng. Sci.* **40** 330 (2000)

Drozdov AD, Christiansen J. *Mech. Res. Commun.* **30** 431–42 (2003)

Drozdov AD, Christiansen C. *Polymer* **44** 1211-28 (2003)

Drozdov AD, Christiansen C. *Polym. Eng. Sci.* **44** 548-56 (2004)

Drozdov AD, Christiansen C. *Polymer* **48** 3003-12 (2007)

Drozdov AD, Christiansen J. *Eur. Polym. J* **43**(1) 10-25 (2007)

Drozdov AD, Christiansen J. *J. Appl. Polym. Sci.* **88** 1438–50 (2003)

Drozdov AD, Gupta RK. *Int. J. Solids. Struct.* **40** 6217–43 (2003)

Drozdov AD. *Int. J. Solids Sturuct.* **38** 8285-304 (2001)

Drozdov AD. *Polym. Eng. Sci.* **40**(3) 818-25 (2000)

Drozdov AD. *Archive of Appl. Mech.* **68** 308-22 (1998)

Drugan WJ, Willis JR. *J. Mech. Phys. Solids*, **44** 497 (1996)

Du J, Zhu J, Wilkie CA, Wang J. *Polym. Deg. Stab.* **77** 377-81 (2002)

Duan Y, Saigal A, Greif R. *Polym. Eng. Sci.* **41**(8) 1322-8 (2001)

Eshelby JD. *Proc R. Soc. Lond. A*, **241** 376 (1957)

Fereshteh-Saniee F, Majzoobi GH, Bahrami M. *J. Materials Processing Technol.* **162–163** 39–45 (2005)

Ferry JD. *Viscoelastic Properties of Polymers* 3rd ed. New York: John Wiley & Sons Inc. (1980)

Fertig III RS, Garnich MR. *Compos. Sci. Technol.* **64** 2577 (2004)

Fu J, Jo C, Naguib HE. *Cell. Polym.* **24** 177-96 (2005)

Fu J, Naguib HE. *J. Cell. Plast.* **42**(4) 325-342 (2006)

Gibson LJ, Ashby MF. *Cellular Solid: Structure and Properties*, 2nd ed. Cambridge (1999)

Gilman JW, Jackson CL, Morgan AB, Harris Jr R, Manias E, Giannelis EP. *Chem. Mater.* **12**(7) 1866-73 (2000)

Gong L, Kyriakides S, Jang W-Y. *Int. J. Solids and Struct.* **42** 1355-79 (2005)

Gong L, Kyriakides S. *Int. J. Solids and Struct.* **42** 1381-99 (2005)

Gopakumar TJ, Lee JA, Kontopoulou M, Parent JS. *Polymer* **43** 5483–91 (2002).

Giannelis EP. *Adv. Mater.* **8** 29 (1996)

Giannelis EP, Krishnamoorti R, Manias E. *Adv. Polym. Sci.* **138** 107 (1999)

Handa YP, Zhang Z, Wong B. *Cell. Polym.* **20** 1–16 (2001)

Halpin JC, Kardos JL. *Polym. Eng. Sci.*, **16**(5) 344 (1976)

Hasan OA, Boyce MC. *Polym. Eng. Sci.* **35**(4) 331-44 (1995)

Hernandez-Jimenez A, Hernandez-Santiago J, Macias-Garcia A, Sanchez-Gonzalez J. *Polymer Testing* **21** 325–31 (2002)

Huang X, Brittain WJ. *Macromolecules* **34** 3255 (2001)

Iannace F, Iannace S, Caprino G, Nicolais L. *Polymer Testing* **20** 643–7 (2001)

Imad A, Ouâkka A, Dang Van K, Mesmacque G. *Strength of Materials* **33** 140-9 (2001)

Jeon HG, Jung HT, Lee SW, Hudson SD. *Polym. Bull.* **41**(1) 107-13 (1998)

Ji XL, Jing JK, Jiang W, Jiang BZ. *Polym. Eng. Sci.* **42**(5) 983-93 (2002)

Jo C, Fu J, Naguib HE. *Polymer* **46** 11896–903 (2005)

Jo C, Fu J, Naguib HE. *Polym. Eng. Sci.* **46** 1787-96 (2006)

Jo C, Naguib HE. *Polymer* **48** 3349 (2007)

Kanny K, Mahfuz H, Carlsson LA, Thomas T, Jeelani S. *Compos. Struc.* **58** 175–83 (2002)

Khan F, Krempl E. *Trans. of the ASME* **128** 64-72 (2006)

Klempner D, Frisch KC. *Handbook of Polymeric Foams and Foam Technology*. Munich: Hanser Publishers, (2004)

Klompen ETJ, Govaert LE. *Mechanics of Time-Dependent Materials* **3** 49–69 (1999)

Kojima Y, Usuki A, Kawasumi M, Okada A, Fukushima Y, Kurauchi T, Kamigaito O. *J. Mater. Res.* **8** 1185 (1993)

Krstic VD. *Arta mctd.* **33** 521-6. (1985)

Kumar S, Jog JP, Natarajan U. *J. Appl. Polym. Sci.* **89** 1186-94 (2003)

Kumar V, VanderWel M, Weller J Seeler KA. *J. Eng. Mater. Technol.* **116** 439–45 (1994)

Kuo MC, Tsai CM, Huang JC, Chen M. *Mater. Chem. Phys.* **90**(1) 185–95 (2005)

Lai D, Yakimets I, Guigon M. *Mat. Sc.i Eng.* **A405** 266–71 (2005)

Lai J, Bakker A. *Polym. Eng. Sci.* **35**(17) 1339-47 (1995)

Laroussi M, Sab K, Alaoui A. *Int. J. Solids and Struct.* **39** 3599-623 (2002)

LeBaron PC, Wang Z, Pinnavaia TJ. *Appl. Clay. Sci.* **15** 11 (1999)

Lee J-H, Jung D, Hong C-E, Rhee KY, Advani SG. *Compos. Sci. Technol.* **65**(13) 1996–2002 (2005)

Lee K, Ghosh S. *Mater. Sci. Eng.* **A272** 120–33 (1999)

Lee BJ, Parks DM, Ahzi S. *J. Mech. Phys. Solids.* **41**(10) 1651-87 (1993)

Lee KY, Goettler LA. *Polym. Eng. Sci.* **44**(6) 1103-11 (2004)

Lee KY, Paul DR. *Polymer* **46** 9064–80 (2005)

Lee YH, Park, CB, Wang KH, Lee MH. *J. Cell. Plast.* **41**(5) 487-502 (2005)

Lee LJ, Zeng C, Cao X, Han X, Shen J, Xu G. *Compos. Sci. Technol.* **65**(15-16) 2344–63 (2005)

Li K, Gao X-L, Roy AK. *Compos. Sci. Technol.* **63** 1769-81 (2003)

Li Y, Zhao B, Xie S, Zhang S. *Polym. Int.* **52** 892 (2003)

Li ZR, Lim CW, He LH Eur. *J. Mech. A/Solids* **25** 260–70 (2006)

Liang G. Xu J, Bao S, Xu W. *J. Appl. Polym. Sci.* **91**(6) 3974 – 80 (2004)

Liao B, Song M, Liang H, Pang Y. *Polymer* **42**(25) 10007-11 (2001)

Lin H-R. *Polym. Test.* **16** 429-43 (1997)

Lin L, Argon AS. *J. Mater. Sci.* **29** 294-323 (1994)

Liu Q, Subhash G. *Polym. Eng. Sci.* **44** 463-73 (2004)

Lopez-Manchado MA, Herrero B, Arroyo M. *Polym. Int.* **53** 1766 (2004)

Lu Z, Zhang H. *J. Beijing University of Aeronautics and Astronautics* **30** 202-5 (2004)

Lubarda VA, Richmond O. *Mechanics of Materials* 31 1-8 (1999)

Luo J-J, Daniel IM. *Compos. Sci. Technol.* **63**(11) 1607–16 (2003)

Manninen A, Naguib HE, Nawaby AV, Day M. *Polym. Eng. Sci.* **45**(7) 904-14 (2005)

Manninen A, Naguib HE, Nawaby AV, Xia L, Day M. *Cell. Polym.* **24**(2) 49-70 (2005)

Matuana LM, Park CB, Balatinecz JJ. *Cell. Polymers* **17** 1–16 (1998)

McNally T, Murphy WR, Lew CT, Turner RJ, Brennan GP. *Polymer* **44** 2761 (2003)

Mehrabzadeh M, Kamal MR. *Polym. Eng. Sci.* **44**(6) 1152–61 (2004)

Mills NJ. *Plastics: microstructure and applications*, Amsterdam, Boston, MA, Elsevier Butterworth Heinemann (2005)

Min KD, Kim MY, Choi K-Y, Lee JH, Lee S-G. *Polym. Bull.* **57**(1) 101–8 (2006)

Miyagawa H, Foo KH, Daniel IM, Drzal LT. *J. Appl. Polym. Sci.*, **96** 281 (2005)

Molinari A, Canova GR, Ahzi S. *Acta metall.* **35**(12) 2983-94 (1987)

Mori T, Tanaka K. *Acta Metall. Mater.* **21**(5) 571 (1973)

Murphy MJ, Truss R, Halley P, Martin D, Ang CL. *ANTEC* 2003 Plastics: Annual Technical Conference, Vol. 1: Processing 1189-93 (2003)

Nemat-Nasser S, Hori M. *Micromechanics: Overall Properties of Heterogeneous Materials*, North-Holland, Amsterdam (1993)

Nieh TG, Higashi K, Wadsworth J. *Mater. Sci. Eng.: A* **283** 105-10 (2000)

Nikolov S, Doghri I. *Polymer* **41** 1883–91 (2000).

Nikolov S, Doghri I, Pierard O, Zealouk L, Goldberg A. *J. Mech. Phys. Solids* **50** 2275–302 (2002)

Nitta K-H, Yamaguchi M. *J. Mat. Sci.* **33** 1015–21 (1998)

Okamoto M, Morita S, Kim YH, Kotaka T, Tateyama H. *Polymer* **42** 1201 (2001)

Osman MA, Rupp JEP, Suter UW. *Polymer* **46**(5) 1653–60 (2005)

Pappas J, Patel K, Nauman EB. *J. Appl. Polym. Sci.*, **95** 1169 (2005)

Park CB, Baldwin DF, Suh NP. *Polym. Eng. Sci.* **35** 432–40 (1995)

Park JH, Jana SC. *Polymer* **44** 2091 (2003)

Pinnavaia JJ, Beall GW. *Polymer Clay Nanocomposites*, John Wiley, New York (1989)

Priya L, Jog JP. *J. Polym. Sci. Part B: Polym. Phys.* **41** 31 (2003)

Qin H, Zhang Z, Feng M, Gong F, Zhang S, Yang M. *J. Polym. Sci. Part B Polym. Phys.* **42**(16) 3006-12 (2004)

Qin H, Zhang S, Zhao C, Feng M, Yang M, Shu Z. *Polym. Degrad. Stab.* **85**(2) 807-13 (2004)

Rachtanapun P, Selke, SEM, Matuana LM. *J. Appl. Polym. Sci.* **88**(12) 2842–50 (2003)

Rachtanapun P, Selke SEM, Matuana LM. *J. Appl. Polym. Sci.* **93**(1) 364–71 (2004)

Ray SS, Bousmina M, Okamoto K. *Macromol. Mater. Eng.* **290** 759 (2005)

Riande E. *Polymer Viscoelasticity: Stress and Strain in Practice*. New York: Marcel Dekker (2000)

Riesz F, Sz.-Nagy B. *Functional Analysis* New York: Frederick Ungar Publishing Co. (1955)

Rodriguez-Perez MA, Velasco JI, Arencon D, Almanza O, De Saja JA. *J. Appl. Polym. Sci.* **75** 156–66 (2000)

Sahraoui S, Mariez E, Etchessahar M. *Polym. Test.* **20** 93–6 (2001)

San Marchi C, Mortensen A. *Acta Mater.* **49** 3959-69 (2001)

Sarva SS, Deschanel S, Boyce MC, Chen W. *Polymer* **48** 2208-13 (2007)

Schiessel H, Metzler R, Blumen A, Nonnenmacher TF. *J. Phys. A: Math. Gen.* **28** 6567–84 (1995)

Schmidt A, Gaul L. *Nonlinear Dynamics* **29** 37–55 (2002)

Schultz JM. *Polymer Crystallization: The Development of Crystalline Order in Thermoplastic Polymers*, Whahington, D.C.: Oxford University Press, 2001 (Ch. 4).

Seeler KA, Kumar V. *J. Reinf. Plast. Compos.* **12** 359–76 (1993)

Sheng N, Boyce MC, Parks DM, Rutledge GC, Abes JI, Cohen RE. *Polymer* **45** 487–506 (2004)

Shia D, Hui CY, Burnside SD, Giannelis EP. *Polym. Compos.* **19** 608 (1998)

Singh R, Davies P, Bajaj AK. *Nonlinear Dynamic* 34 319–46 (2003)

Sneddon IN. *Proc. R. Soc. Lond. Ser. A* **187:1009** 229 (1946)

Spathis G. and E. Kontou. *Polymer* **39**(1) 135-142 (1998)

Swain SK, Isayev AI. *Polymer* **48** 281-9 (2007)

Tabtiang A, Lumlong S, Venables RA. *Eur. Polym. J.* **36** 2559 (2000)

Taylor DM, Fernandez O. *IEEE Trans. on Dielectrics and Electrical Insulation* **12**(4) 768–78 (2005)

Tandon GP, Weng GJ. *Compos. Sci. Technol.* **27** 111 (1986)

Tseng C, Wu JY, Lee HY, Chang FC. *J. Appl. Polym. Sci.* **85** 1370 (2002)

Tsukrov I. *Int. J. Fracture* **101** L29 (2000)

Tzavalas S, Macchiarlla K, Gregoriou VG. *J. Polym. Sci. B: Polym. Phys.* **44** 914–24 (2006)

Unal H, Mimaroglu A, Alkan M. *Polym. Int.* **53** 56 (2004)

Usuki A, Koiwai A, Kojima Y, Kawasumi M, Okada A, Kurauchi T, Kamigaito O. *J. Appl. Polym. Sci.* **55** 119-23 (1995)

Vaia RA, Price G, Ruth PN, Nguyen HT, Lichtenhan J. *Appl. Clay. Sci.* **15** 67 (1999)

Vu YT, Rajan GS, Mark JE, Myers CL. *Polym. Int.* **53**(8) 1071–7 (2004)

Wan C, Qiao X, Zhang Y. *Polymer Test.* **22** 453 (2003)

Wang H, Zeng C, Elkovitch M, Lee LJ, and Koelling KW. *Polym. Eng. Sci.* **41** 2036 (2001)

Wang KH, Choi MH, Koo CM, Choi YS, Chung IJ. *Polymer* **42**(24) 9819-26 (2001)

Wang KH, Chung IJ, Jang CM, Keum JK, and Song HH. *Macromol.* **35**(14) 5529-35 (2002)

Wang KH, Choi MH, Koo CM, Xu M, Chung IJ, Jang CM, Choi SW, Song HH. *J. Polym. Sci. Part B: Polym. Phys.* **40**(14) 1454-63 (2002)

Wang S, Hu Y, Zhongkai Q, Wang Z, Chen Z, Fan W. *Mater. Lett.* **57**(18) 2675-8 (2003)

Wang S, Zhang Yong, Ren W, Zhang Yinxi, Lin H. *Polymer Test.* **24** 766 (2005)

Wang W, Fu M, Qu B. *Polym. Adv. Tech.* **15** 467 (2004)

Wang Z, Pinnavaia TJ. *Chem. Mater.* **10** 3769 (1998)

Wang Z-P, Huang F-L. *Theor. Appl. Fract. Mech.* **23** 209 (1995)

Wei L, Tang T, Huang B. *J. Polym. Sci. A: Polym. Chem.* **42**(4) 941–9 (2004)

Weimer MW, Chen H, Giannelis EP, Sogah DY. *J. Am. Chem. Soc.* **121**(7) 1615-6 (1999)

White SW, Kim SK, Bajaj AK, Davies P, Showers DK, Liedtke PE. *Nonlinear Dynamics* **22** 281–313 (2000)

Winberg P, Eldrup M, Pedersen NJ, van Es MA, Maurer FHJ. *Polymer* **46** 8239 (2005)

Wunderlich B, Czornyj G. *Macromol.* **10**(5) 906 (1977)

Xiang B, Guan R, Fang Q, Xiao Z, Jiang Y. *J. Appl. Polym. Sci.* **99**(4) 1760–1766 (2006)

Xie X-L, Li R, Liu Q-X, Mai Y-W. *Polymer* **45** 2793 (2004)

Xu Y, Fang Z, Tong L. *J. Appl. Polym. Sci.* **96**(6) 2429–34 (2005)

Yang F, Nelson GL. *J. Appl. Polym. Sci.* **91** 3844 (2004)

Yano K. Usuki A, Okada A, Kurauchi T, Kamigaito O. *J. Polyrn. Sci Part A: Polym. Chem.* **31** 2493-98 (1993)

Yin HP, Ehrlacher A. *Mechanics of Materials* **23** 287-94 (1996)

Zerda AS, Lesser AJ. *J. Polym. Sci. Part B: Polym. Phys.* **39** 1137 (2001)

Zhang C. and I.D. Moore. *Polym. Eng. Sci.* **37**(2) 414-20 (1997)

Zhang J, Wilkie CA. *Polym. Degrad. Stab.* **80**(1) 163-9 (2003)

Zhang J, Kikuchi N, Li V, Yee A, Nusholtz G. *Int. J. Impact Eng.* **21** 369-386 (1998)

Zhang Y, Rodrigue D, Ait-Kadi A. *J. Appl. Polym. Sci.* **90**(8) 2111–9 (2003)

Zhao C, Qin H, Gong F, Feng M, Zhang S, Yang M. *Polym. Degrad. Stab.* **87** 183-9 (2005)

Zheng W, Lu X, Wong S-C. *J. Appl. Polym. Sci.*, **91**, 2781 (2004)

Zhong Y, Kee DD. *Polym. Eng. Sci.* **45**(4) 469–77 (2005)

Zhou Y, Mallick PK. *Polym. Eng. Sci.* **42**(2) 2461-70 (2002)

Zhu HX, Knott JF, Mills NJ. *J. Mech. Phys. Solids* **45** 319-43 (1997)

Zhu HX, Mills NJ, Knott JF. *J. Mech. Phys. Solids* **45** 1875-904 (1997)

Zhu HX, Hobdell JR, Windle AH. *Acta Mater.* **48** 4893-900 (2000)

Zhu HX, Windle AH. *Acta Mater.* **50** 1041-52 (2002)